SMALL SCALE AEOLIAN PROCESSES AND

LANDFORM RESPONSE

by

PEI ZHANG

DOUGLAS J. SHERMAN, COMMITTEE CHAIR
HONGXING LIU
ERIC J. PARTELI
JEAN T. ELLIS
SAGY COHEN

A DISSERTATION

Submitted in partial fulfillment of the requirements
for the degree of Doctor of Philosophy
in the Department of Geography
in the Graduate School of
The University of Alabama

TUSCALOOSA, ALABAMA

2022

ABSTRACT

When the wind blows across a surface with erodible grains, it exerts a shear stress on the surface. When the strength of the wind increases, those grains on the surface can be moved. The transported grains exchange momentum with fluid flow, interact with the surface, and then finally settle down when the wind strength becomes too weak to maintain their motion. The deposited grains produce various landforms from centimeter-scale sand ripples to meter- or kilometer-scale dunes and dune fields on terrestrial and extraterrestrial surfaces. In this dissertation, I investigated three subjects concerning small-scale aeolian processes and landforms: 1) the mechanisms of the low-energy creep mode of sand motion, especially the proportion of creep relative to the total transport within the aeolian system; 2) a method to efficiently delineate grainflow boundaries from a dune slipface; and 3) grainflow morphology characteristics on dunes of different sizes. To address these understudied topics, I integrated field data, signal and image processing techniques, and remote sensing and GIS techniques, to elucidate questions and arguments relevant to the study of aeolian processes and landforms.

This dissertation focuses on aeolian landforms that respond quickly to forcing processes by studying creep motion and grainflow morphology. We reviewed the literature on aeolian creep and found a fundamental deficit in the understanding of the sand transport system. We argued for an agreement on creep definition and accompanying measurement methods. We developed an algorithm to objectively and efficiently delineate grainflow boundaries. It is an essential tool to study aeolian processes on slipfaces and is also applicable to the broader family of geophysical flows. we addressed grainflow morphology on two relatively large dunes. The quantification and classification of grainflow morphology showed that grainflow shapes were dune-size dependent. The findings of this dissertation are relevant to the formation and evolution of aeolian landforms with associated processes.

DEDICATION

This dissertation is dedicated to everyone who helped me and guided me to get my doctoral degree. In particular, my supervisor and close friends continuously support me.

LIST OF ABBREVIATIONS AND SYMBOLS

u_*	Shear velocity
u_{*t}	Threshold shear velocity
u	Wind speed
u_t	Threshold wind speed
u_r	Ripple migration rate
q_s	Saltation transport rate
q_c	Creep transport rate
q	Total sand transport rate ($q = q_c + q_s$)
PTV	Particle-tracking velocimetry
ρ_s	Sand density
ρ	Fluid (air) porosity
H	Ripple height
g	Gravity constant
d	Sand grain diameter
DEM	Digital Elevation Model
DoD	Difference of DEM_s

ACKNOWLEDGEMENTS

I would like to thank my supervisor Professor Douglas J. Sherman for his continuous support of my doctoral research throughout these years. As my advisor, he provided me with generous help and was the academic model in my research. I learned a lot to write proposals, publish papers, prepare and conduct fieldwork, to communicate with people from diverse backgrounds. He is always patient with me and helps me improve my writing. As an expert in the aeolian academic circle, he respects all my opinions and discusses different ideas in an equal manner. He showed me a high standard to do research, teach courses, and mentor students in my future career.

I am also very thankful to the other committee members: Dr. Eric Parteli, Dr. Hongxing Liu, Dr. Jean Ellis, and Dr. Sagy Cohen, for their patience and constructive suggestions on my dissertation especially the new topics designed due to the influence of COVID.

My colleagues, Drs. Jean Ellis, Hong Cheng, Bailiang Li, Christy Swann, and Jordan Cissell, and friends, Diane Sherman, Qiaomin Pei, Huiru Li, Emily Durham, and Bonner Lee, were especially important in helping me succeed in getting my degree. Without their help in my research and life, I doubt that I can come here today. Most importantly, I would like to thank my parents and younger brother.

I would like to thank the Department of Geography and Graduate School for the continued support of graduate students. I would also like to thank National Science Foundation and Dissertation fund from Graduate School and Geography department for providing funds to conduct a field experiment in August 2021. This dissertation is funded by Graduate School Fellowship.

CONTENTS

LIST OF TABLES

LIST OF FIGURES

CHAPTER 1 INTRODUCTION

Motivation

Aeolian processes are a significant driving force of landscape change in windy deserts, many coastal environments, and on the surfaces of extraterrestrial bodies. Potential environments on Earth exposed to aeolian processes include the arid and semi-arid areas that cover more than 30% of the earth's land surface (Okin et al., 2006) and the coastal dunes that occur around three-quarters of the world's shorelines (Bascom, 1980). On Mars, it has been suggested that aeolian processes have been a dominant agency for a geologically significant period (Fenton, 2003). Because of the important influence of aeolian processes on landscape changes on Earth, Mars, and other extraterrestrial surfaces, understanding the mechanisms of aeolian processes and their interactions with landforms is important for several reasons. First, there is an increased appreciation of the environmental hazards caused by aeolian-driven processes, including the abrasion of infrastructure by drifting sand, degradation and erosion of agricultural lands, and the onset of human health issues induced by the increase in inhalable dust which is often generated by saltating sand grains (Mohammed et al., 1995; Gillette et al., 1997; Prospero and Lamb, 2003; Okin, 2005; Gillies, 2013; Flagg et al., 2014; Tsiouri et al., 2015; Huo et al., 2017; Wang et al., 2017; Duniway et al., 2019). Second, the processes of wind-driven transport on Earth can be analogs for aqueous and Martian environments (Bagnold, 1951; Claudin and Andreotti, 2006; Cohn et al., 2019). The differences lie in the fluid properties and gravity forces. Third, blowing sand contributes to the formation of dunes. Coastal dunes support important ecosystems and protect onshore developments from beach erosion and inundations by storm surges (Morton and Paine, 1985; Feagin et al., 2005; Houser and Hamilton, 2009; Bochev-Van der Burgh et al., 2011; Hanley et al., 2014). The migration of dunes may also threaten the burial of resources, infrastructure, and residential communities (Mohammed et al., 1995; Han et al., 2003; Hamdan et al., 2016; Bruno et al., 2018; Sigren et al., 2018; Seif and El-Khashab, 2019).

In this dissertation, I focus on wind-blown sand transport mechanisms by studying aeolian processes in relatively ideal conditions at temporal scales from minutes to tens of minutes and at spatial scales of centimeters to tens of meters.

This dissertation addresses two particular themes in aeolian research: 1) the physical mechanisms of sand transport, specially creep motion and 2) the morphodynamics of the leeside of dunes, specially grainflows. By integrating the collected field data, signal and image processing techniques, remote sensing and GIS techniques, I focused on the nature of sand transport and gravity-driven grainflow morphology characteristics. As is indicated by Fenton (2003), each data set adds its unique piece of the puzzle to the interpretation of overall system behavior. This dissertation presents several pieces of the overall aeolian system puzzle.

Figure 1.1 is a schematic of the framework of this dissertation which comprises three papers that have been published in peer-review journals. These papers are presented in Chapters 2-4. Chapter 2 (Figure 1.1 (a)), "Zhang, P., Sherman, D.J. and Li, B., 2021. Aeolian creep transport: A review. *Aeolian Research*, 51, https://doi.org/10.1016/j.aeolia.2021.100711", is focused on a review of aeolian creep transport. Two types of creep motion are defined: fluid creep and impact creep. Chapter 2 shows that the creep proportion of total transport is a wide range (1 – 50%) which is in contrast with the constant proportion (25%) suggested by Bagnold (1936; 1937; 1938). The review of creep transport indicates a fundamental deficit in our understanding of the sand transport system. Chapter 3 (Figure 1.1 (b)), "Zhang, P., 2021. An algorithm for objective analysis of grainflow morphology. *Aeolian Research*, 50, https://doi.org/10.1016/j.aeolia.2021.100686", presents an algorithm to objectively and efficiently extract grainflow boundaries by processing Digital Elevation Models (DEMs) in Matlab and ArcGIS. This method is also applicable to other forms of slope failure and geophysical flows, e.g., avalanches, snowslides, landslides, and debris flows. Chapter 4 (Figure 1.1 (c)), "Zhang, P., Sherman, D., Pelletier, J., Ellis, J., Farrell, E. and Li, B., 2022. Quantification and classification of grainflow morphology on natural dunes. *Earth Surface Processes and Landforms*, https://doi.org/10.1002/esp.5348", is the quantification and classification of grainflow morphology, which is scarce in the literature. The results show that

grainflow shape characteristics are dependent on dune height, which emphasizes the limitations of previous studies on small dunes (less than 10 m high). In the last chapter, a summary of the key findings of this dissertation and critiques on each chapter are provided. The purpose of my dissertation is not to create a unified model of aeolian sand transport, but to address the neglected or underappreciated parts of wind-blown sand transport and dune leeside morphodynamics.

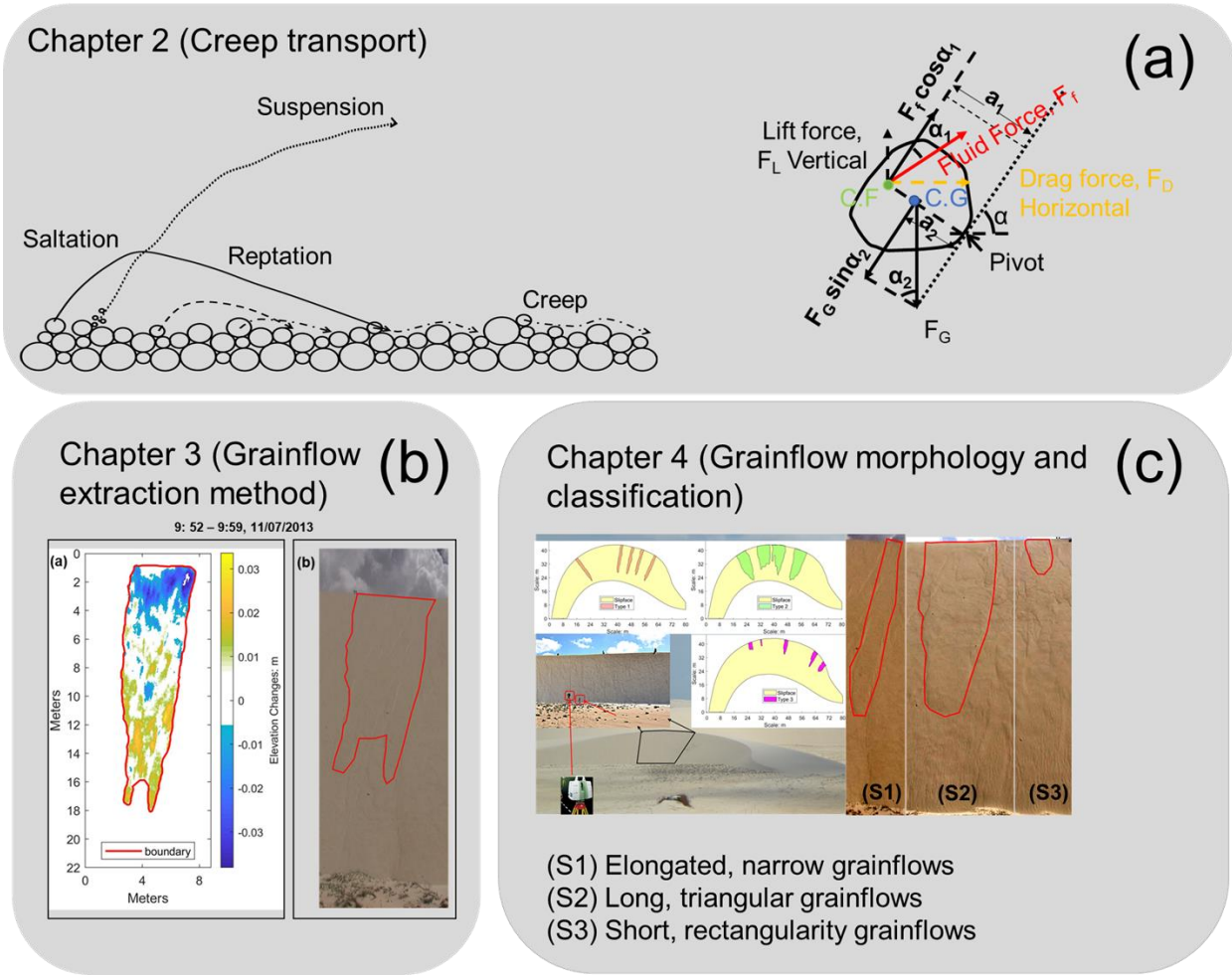

Figure 1. 1. The schematic layout of this dissertation and typical representations from chapter 2 to chapter 4. (a) Chapter 2 is a review on aeolian creep transport. The left panel shows the different modes of wind-blown sand transport. The right panel illustrates the forces on a grain (modified from Middleton and Southard (1984). (b) Chapter 3 is concerned with an algorithm for objective analysis of grainflow morphology. The figure shows an example of boundaries comparison by using my designed algorithm and manual drawing. (c) Chapter 4 is concerned with grainflow morphology quantification and classification. The figure shows examples of three typical grainflows.

Conceptually, the physics of aeolian sand transport mechanisms are easy to understand. Figure 1.2 shows the conceptual model of fluid-particle interactions and feedback on an erodible sand surface.

When the airborne shear stress exerted on a sand surface is sufficient to overcome the gravity and cohesion-induced resistance to motion, a grain starts to move either by rolling along the surface (e.g., particles creeping along the surface), or saltating into the air (Figure 1.2 (a) fluid-transport interaction). Once a saltating grain returns to an erodible surface, it can rebound into the air and force other grains into motion. The continuous interaction between saltating particles and the surface can contribute to the formation of different landforms, e.g., sand ripples and dunes (Figure 1.2 (b) transport-bedform interaction). The variations of the bedform, e.g., dunes, can alter fluid flow characteristics (Figure 1,2 (c) bedform-fluid interaction). The conceptual model becomes intractable, however, when we want to quantitatively express the physics of fluid-grain motion. For example, there are many complicated models (Anderson and Hallet, 1986; Mcewan et al., 1992; Kok, 2010; Ren and Huang, 2010; Duran et al., 2012; Dupont et al., 2013; Li et al., 2014b; Zhu et al., 2019; Jin et al., 2021; Pahtz et al., 2021) to explain the 1) interaction between moving grains and fluid forces, 2) momentum exchange within the fluid and grains in motion, grain rebound, impact, and 3) collision with bed surface to involve one or more grains into motion. The sophistication of many models, however, has substantially exceeded the empiricism necessary to support them, often including variables about which our knowledge is scant or naïve. Understanding the physical mechanisms involved becomes even more complicated when including grain size characteristics, moisture content, plants, and topographic variations.

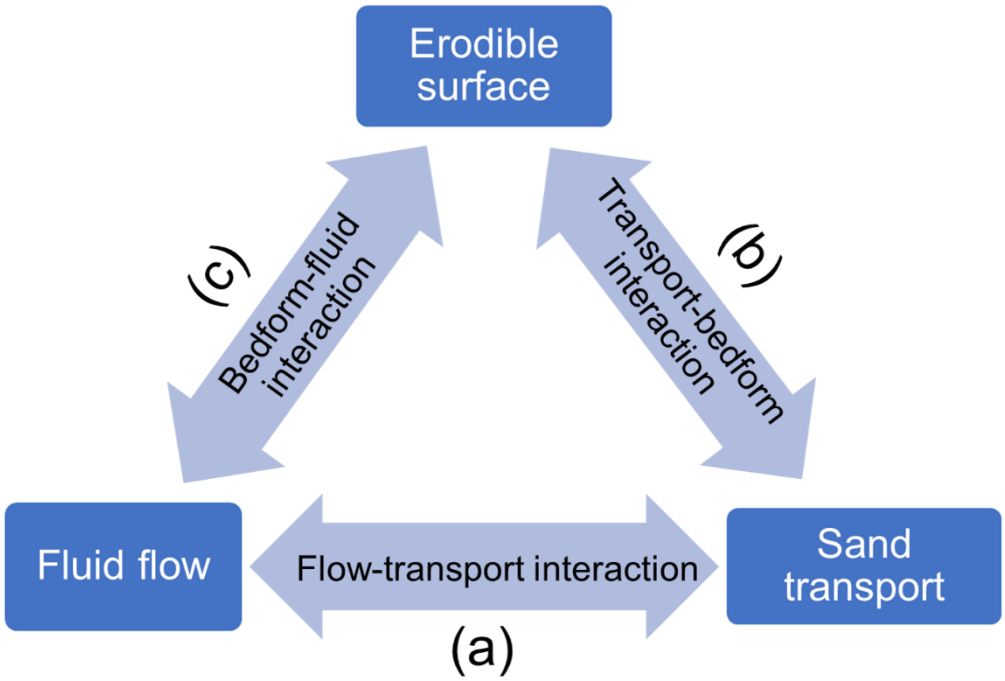

Figure 1. 2. A conceptual model of fluid-particle interactions and feedback on an erodible surface. It is modified from Livingstone (2007, Fig. 3).

Aeolian dunes have been of interest to scientists in the disciplines of geography, geology, geomorphology, ecology, sedimentology, and climatology, among others (Kocurek, 1991; Sherman and Bauer, 1993; Mcfadgen, 1994; Walker and Nickling, 2002; Crouvi et al., 2008; Thompson et al., 2021). The recognition of the similarity between flow dynamics over dunes and hills has facilitated the application of aerodynamic concepts from other disciplines (e.g., engineering, physics, and applied mathematics) to dune studies (Wiggs, 2001). For example, previous field and modeling studies have attempted to estimate sand transport rates based on the distributions of shear stress exerted on the windward and leeward sides of dunes (Howard et al., 1978; Mulligan, 1988; Frank and Kocurek, 1996; Lancaster et al., 1996; Parsons et al., 2004; Smith et al., 2017). Great advances have been made to enhance our understanding of the interactions between airflow and erodible sand grains in time and space due to flow acceleration on the windward slopes (Lancaster et al., 1996; Momiji and Bishop, 2002; Lancaster, 2009; Weaver and Wiggs, 2011; Dong et al., 2017). On the leeside of a dune, however, sediment transport processes have received relatively little attention. Grainflow, or avalanching, is a

primary sediment transport process driven by gravity that occurs on a dune slipface. After the deposition of windblown sand near the brink of a slipface, a grainflow is initiated by the over-steeping of the slope. Grainflows are significant and well-organized signatures on the leeside, and studying the morphodynamics of grainflows is important to understanding dune migration characteristics (Mcdonald and Anderson, 1995; Nickling et al., 2002; Sutton et al., 2013a; Cornwall et al., 2018b). McDonald and Anderson (1996) suggested that an important step toward generating a complete model of dune evolution, stratigraphy, and migration was to develop rules to describe the redistribution of sand in a manner consistent with grainflow processes. More than two decades have passed since the advocation of McDonald and Anderson (1996), and we are still at the exploratory stage of understanding grainflows on slipfaces (Nickling et al., 2002; Sutton et al., 2013a, b; Cornwall et al., 2018b). For example, there are insufficient studies or objective comparisons on grainflow morphodynamics; these include: 1) different grainflow formation and initiation mechanisms are raised but without quantitative connection with the morphodynamics of a grainflow itself; 2) the morphology of grainflows is a manual measurement based on different visual definitions (Ewing et al., 2017; Cornwall et al., 2018a; Cornwall et al., 2018b), which makes it hard to have objective evaluations and comparisons; 3) the sample sizes of previous case studies are small ($N < 80$) and from dunes less than 10 m high, and since the lengths of grainflows are highly dependent on the slipfaces of dunes, the results of previous studies cannot be extended to relatively large dunes.

In this dissertation, I reviewed the basic mechanisms in creep transport motion and methods to measure near-surface creep transport rates and presented a detailed analysis of grainflow morphology from two large barchans (21.3 m and 54.5 m high). We firstly raised two types of creep motion and compared available studies on creep. We found a fundamental deficit in the understanding of the sand transport system. We used an algorithm to delineate the boundaries of a large number of grainflows (of the order of 10^3) from the two aforementioned dunes. We then discussed and classified the morphometric attributes of grainflows on natural dunes.

In aeolian geomorphology study, our ability to understand the existence of different scales of aeolian landforms is dependent on the interpretation of the interactions of the wind-sand system. This dissertation focuses on the highly responsive aeolian landforms to corresponding aeolian processes, which provides an opportunity to closely examine the morphodynamic interactions. We believe we can understand the steps from a sandy surface to wind-driven sand transport to the formation and evolution of different aeolian landforms by studying the interactions of the wind-sand system.

Reference List for Introduction

Anderson, R.S., Hallet, B., 1986. Sediment Transport by Wind - toward a General-Model. Geological Society of America Bulletin 97, 523-535.

Bagnold, R.A., 1936. The movement of desert sand. Proceedings of the Royal Society of London. Series A-Mathematical and Physical Sciences 157, 594-620.

Bagnold, R.A., 1937. The transport of sand by wind. The Geographical Journal 89, 409-438.

Bagnold, R.A., 1938. The measurement of sand storms. Proceedings of the Royal Society of London. Series A. Mathematical and Physical Sciences 167, 282-291.

Bagnold, R.A., 1951. The movement of a cohesionless granular bed by fluid flow over it. British Journal of Applied Physics 2, 29.

Bascom, W., 1980. Waves and beaches Doubleday, NY: Anchor Press, 366.

Bochev-Van der Burgh, L., Wijnberg, K.M., Hulscher, S.J., 2011. Decadal-scale morphologic variability of managed coastal dunes. Coastal engineering 58, 927-936.

Bruno, L., Horvat, M., Raffaele, L., 2018. Windblown sand along railway infrastructures: A review of challenges and mitigation measures. Journal of Wind Engineering and Industrial Aerodynamics 177, 340-365.

Claudin, P., Andreotti, B., 2006. A scaling law for aeolian dunes on Mars, Venus, Earth, and for subaqueous ripples. Earth Planet Sc Lett 252, 30-44.

Cohn, N., Hoonhout, B.M., Goldstein, E.B., de Vries, S., Moore, L.J., Vinent, O.D., Ruggiero, P., 2019. Exploring Marine and Aeolian Controls on Coastal Foredune Growth Using a Coupled Numerical Model. J Mar Sci Eng 7.

Cornwall, C., Bourke, M.C., Jackson, D.W.T., Cooper, J.A.G., 2018a. Aeolian slipface dynamics and grainflow morphologies on Earth and Mars. Icarus 314, 311-326.

Cornwall, C., Jackson, D.W.T., Bourke, M.C., Cooper, J.A.G., 2018b. Morphometric analysis of slipface processes of an aeolian dune: Implications for grain-flow dynamics. Sedimentology 65, 2034-2054.

Crouvi, O., Amit, R., Enzel, Y., Porat, N., Sandler, A., 2008. Sand dunes as a major proximal dust source for late Pleistocene loess in the Negev Desert, Israel. Quaternary Res 70, 275-282.

Dong, Y.X., Hesp, P.A., Huang, D.Q., Namikas, S.L., 2017. Flow dynamics and sediment transport over a reversing barchan, Changli, China. Geomorphology 278, 121-127.

Duniway, M.C., Pfennigwerth, A.A., Fick, S.E., Nauman, T.W., Belnap, J., Barger, N.N., 2019. Wind erosion and dust from US drylands: a review of causes, consequences, and solutions in a changing world. Ecosphere 10, e02650.

Dupont, S., Bergametti, G., Marticorena, B., Simoens, S., 2013. Modeling saltation intermittency. J Geophys Res-Atmos 118, 7109-7128.

Duran, O., Andreotti, B., Claudin, P., 2012. Numerical simulation of turbulent sediment transport, from bed load to saltation. Phys Fluids 24.

Ewing, R.C., Lapotre, M.G.A., Lewis, K.W., Day, M., Stein, N., Rubin, D.M., Sullivan, R., Banham, S., Lamb, M.P., Bridges, N.T., Gupta, S., Fischer, W.W., 2017. Sedimentary processes of the Bagnold Dunes: Implications for the eolian rock record of Mars. J Geophys Res-Planet 122, 2544-2573

Feagin, R.A., Sherman, D.J., Grant, W.E., 2005. Coastal erosion, global sea-level rise, and the loss of sand dune plant habitats. Frontiers in Ecology and the Environment 3, 359-364.

Fenton, L.K., 2003. Aeolian processes on Mars: atmospheric modeling and GIS analysis. California Institute of Technology.

Flagg, C.B., Neff, J.C., Reynolds, R.L., Belnap, J., 2014. Spatial and temporal patterns of dust emissions (2004–2012) in semi-arid landscapes, southeastern Utah, USA. Aeolian Research 15, 31-43.

Frank, A., Kocurek, G., 1996. Toward a model for airflow on the lee side of aeolian dunes. Sedimentology 43, 451-458.

Gillette, D.A., Fryrear, D., Gill, T.E., Ley, T., Cahill, T.A., Gearhart, E.A., 1997. Relation of vertical flux of particles smaller than 10 μm to total aeolian horizontal mass flux at Owens Lake. Journal of Geophysical Research: Atmospheres 102, 26009-26015.

Gillies, J., 2013. Fundamentals of aeolian sediment transport: dust emissions and transport—near surface. Treatise on Geomorphology. 11. Elsevier Ltd. http://dx. doi. org/10.1016/B978-0-12-374739-6.00297-9.

Hamdan, M., Refaat, A., Wahed, M.A., 2016. Morphologic characteristics and migration rate assessment of barchan dunes in the Southeastern Western Desert of Egypt. Geomorphology 257, 57-74.

Han, Z., Wang, T., Sun, Q., Dong, Z., Wang, X., 2003. Sand harm in Taklimakan Desert highway and sand control. Journal of geographical sciences 13, 45-53.

Hanley, M., Hoggart, S., Simmonds, D., Bichot, A., Colangelo, M., Bozzeda, F., Heurtefeux, H., Ondiviela, B., Ostrowski, R., Recio, M., 2014. Shifting sands? Coastal protection by sand banks, beaches and dunes. Coastal Engineering 87, 136-146.

Houser, C., Hamilton, S., 2009. Sensitivity of post-hurricane beach and dune recovery to event frequency. Earth Surface Processes and Landforms 34, 613-628.

Howard, A., Morton, J., GAD-EL-HAK, M., Pierce, D.B., 1978. Sand transport model of barchan dune equilibrium. Sedimentology 25, 307-338.

Huo, W., He, Q., Yang, F., Yang, X., Yang, Q., Zhang, F., Mamtimin, A., Liu, X., Wang, M., Zhao, Y., 2017. Observed particle sizes and fluxes of Aeolian sediment in the near surface layer during sand-dust storms in the Taklamakan Desert. Theoretical and Applied Climatology 130, 735-746.

Jin, T., Wang, P., Zheng, X.J., 2021. Characterization of Wind-Blown Sand With Near-Wall Motions and Turbulence: From Grain-Scale Distributions to Sediment Transport. J Geophys Res-Earth 126.

Kocurek, G., 1991. Interpretation of Ancient Eolian Sand Dunes. Annu Rev Earth Pl Sc 19, 43-75.

Kok, J.F., 2010. An improved parameterization of wind-blown sand flux on Mars that includes the effect of hysteresis. Geophysical Research Letters 37.

Lancaster, N., 2009. Aeolian features and processes. The Geological Society of America, 1-25.

Lancaster, N., Nickling, W., Neuman, C.M., Wyatt, V., 1996. Sediment flux and airflow on the stoss slope of a barchan dune. Geomorphology 17, 55-62.

Li, Z.Q., Wang, Y., Zhang, Y., 2014b. A numerical study of particle motion and two-phase interaction in aeolian sand transport using a coupled large eddy simulation - discrete element method. Sedimentology 61, 319-332.

Livingstone, I., Wiggs, G.F., Weaver, C.M., 2007. Geomorphology of desert sand dunes: A review of recent progress. Earth-science reviews 80, 239-257.

Mcdonald, R.R., Anderson, R.S., 1995. Experimental-Verification of Aeolian Saltation and Lee Side Deposition Models. Sedimentology 42, 39-56.

McDonald, R.R., Anderson, R.S., 1996. Constraints on eolian grain flow dynamics through laboratory experiments on sand slopes. Journal of Sedimentary Research 66, 642-653.

Mcewan, I.K., Willetts, B.B., Rice, M.A., 1992. The Grain Bed Collision in Sand Transport by Wind. Sedimentology 39, 971-981.

Mcfadgen, B.G., 1994. Archaeology and Holocene Sand Dune Stratigraphy on Chatham-Island. J Roy Soc New Zeal 24, 17-44.

Middleton, G., Southard, J., 1984. Mechanics of Sediment Movement. Soc. of Econ. Paleontol. and Mineral., Tulsa, Okla.

Mohammed, A., Stigter, C., Adam, H., 1995. Moving sand and its consequences on and near a severely desertified environment and a protective shelterbelt. Arid Land Research and Management 9, 423-435.

Momiji, H., Bishop, S.R., 2002. Estimating the windward slope profile of a barchan dune. Sedimentology 49, 467-481.

Morton, R.A., Paine, J.G., 1985. Beach and vegetation-line changes at Galveston Island, Texas: erosion, deposition, and recovery from Hurricane Alicia.

Mulligan, K.R., 1988. Velocity profiles measured on the windward slope of a transverse dune. Earth surface processes and Landforms 13, 573-582.

Nickling, W.G., Neuman, C.M., Lancaster, N., 2002. Grainfall processes in the lee of transverse dunes, Silver Peak, Nevada. Sedimentology 49, 191-209.

Okin, G., Gillette, D., Herrick, J., 2006. Multi-scale controls on and consequences of aeolian processes in landscape change in arid and semi-arid environments. Journal of arid environments 65, 253-275.

Okin, G.S., 2005. Dependence of wind erosion and dust emission on surface heterogeneity: Stochastic modeling. Journal of Geophysical Research: Atmospheres 110.

Pahtz, T., Liu, Y.H., Xia, Y.Z., Hu, P., He, Z.G., Tholen, K., 2021. Unified Model of Sediment Transport Threshold and Rate Across Weak and Intense Subaqueous Bedload, Windblown Sand, and Windblown Snow. J Geophys Res-Earth 126.

Parsons, D.R., Walker, I.J., Wiggs, G.F.S., 2004. Numerical modelling of flow structures over idealized transverse aeolian dunes of varying geometry. Geomorphology 59, 149-164.

Prospero, J.M., Lamb, P.J., 2003. African droughts and dust transport to the Caribbean: Climate change implications. Science 302, 1024-1027.

Ren, S., Huang, N., 2010. A numerical model of the evolution of sand saltation with consideration of two feedback mechanisms. Eur Phys J E 33, 351-358.

Seif, E.-S.S.A., El-Khashab, M.H., 2019. Desertification risk assessment of sand dunes in middle Egypt: a geotechnical environmental study. Arabian Journal for Science and Engineering 44, 357-375.

Sherman, D.J., Bauer, B.O., 1993. Dynamics of Beach-Dune Systems. Prog Phys Geog 17, 413-447.

Sigren, J.M., Figlus, J., Highfield, W., Feagin, R.A., Armitage, A.R., 2018. The effects of coastal dune volume and vegetation on storm-induced property damage: analysis from Hurricane Ike. Journal of Coastal Research 34, 164-173.

Smith, A.B., Jackson, D.W.T., Cooper, J.A.G., 2017. Three-dimensional airflow and sediment transport patterns over barchan dunes. Geomorphology 278, 28-42.

Sutton, S.L.F., Neuman, C.M., Nickling, W., 2013a. Avalanche grainflow on a simulated aeolian dune. J Geophys Res-Earth 118, 1767-1776.

Sutton, S.L.F., Neuman, C.M., Nickling, W., 2013b. Lee slope sediment processes leading to avalanche initiation on an aeolian dune. J Geophys Res-Earth 118, 1754-1766.

Thompson, T.A., Argyilan, E.P., Johnson, M.R., Monaghan, G.W., 2021. Stratigraphic and sedimentologic investigation of collapse features in the Mount Baldy Dune in the Indiana Dunes National Park. J Great Lakes Res 47, 1485-1494.

Tsiouri, V., Kakosimos, K.E., Kumar, P., 2015. Concentrations, sources and exposure risks associated with particulate matter in the Middle East Area—a review. Air Quality, Atmosphere & Health 8, 67-80.

Walker, I.J., Nickling, W.G., 2002. Dynamics of secondary airflow and sediment transport over and in the lee of transverse dunes. Progress in Physical Geography-Earth and Environment 26, 47-75.

Wang, X., Cheng, H., Che, H., Sun, J., Lu, H., Qiang, M., Hua, T., Zhu, B., Li, H., Ma, W., 2017. Modern dust aerosol availability in northwestern China. Scientific reports 7, 1-8.

Weaver, C.M., Wiggs, G.F.S., 2011. Field measurements of mean and turbulent airflow over a barchan sand dune. Geomorphology 128, 32-41.

Wiggs, G.F., 2001. Desert dune processes and dynamics. Progress in physical geography 25, 53-79.

Zhu, W., Huo, X.H., Zhang, J., Wang, P., Pahtz, T., Huang, N., He, Z.G., 2019. Large Effects of Particle Size Heterogeneity on Dynamic Saltation Threshold. J Geophys Res-Earth 124, 2311-2321.

CHAPTER 2 AEOLIAN CREEP TRANSPORT: A REVIEW

Abstract

This paper reviews the literature on the nature of aeolian creep, the field and wind tunnel methods used to measure creep transport, the relative contribution of creep transport to total transport, and creep models. We discuss the dynamics of fluid- and impact-driven creep, potential sources of error in creep measurement or estimation, and the variability of the relative contribution of creep to total transport. We compare and discuss creep transport studies conducted in wind tunnels and in the field and demonstrate the disparity of results between different studies. Regression analysis of creep data indicates no significant relationship between the proportion of sand flux moved as creep and the magnitude of wind forcing. Individual studies are shown to produce contradictory results for the relationship between the proportion of total transport moved as creep and wind forcing. These findings point to the importance of better empiricism, especially, to elucidate the role of creep in wind-blown sand systems.

Highlights:

- Wind tunnel and field studies on aeolian creep are reviewed.
- Aeolian creep is defined as fluid creep and impact creep.
- Literature review reveals contradictions for relative contributions of creep to total transport.
- No consensus on how to define and measure creep transport.
- At the initiation of motion fluid creep is critical for the development of saltation.

Keywords: Initiation of motion, Saltation, Sand traps, Sand transport modes, Ripple migration

Introduction

Wind-blown sand is a fundamental agent for landscape change in many terrestrial and extra-terrestrial environments. Beyond its many geomorphological impacts, drifting sand can encroach upon

human settlements and infrastructure (Zhang et al., 2005; Samarkandi et al., 2017; Duniway et al., 2019), inundate adjacent ecosystems (Prospero and Lamb, 2003; Mahowald et al., 2010; Tsoar, 2013; Halfen et al., 2016), and generate atmospheric dust (Okin, 2005; Flagg et al., 2014; Tsiouri et al., 2015; Bolles et al., 2017; Huo et al., 2017). The modes by which wind-blown sand is moved are creep, reptation, saltation, and suspension (Figure 2.1).

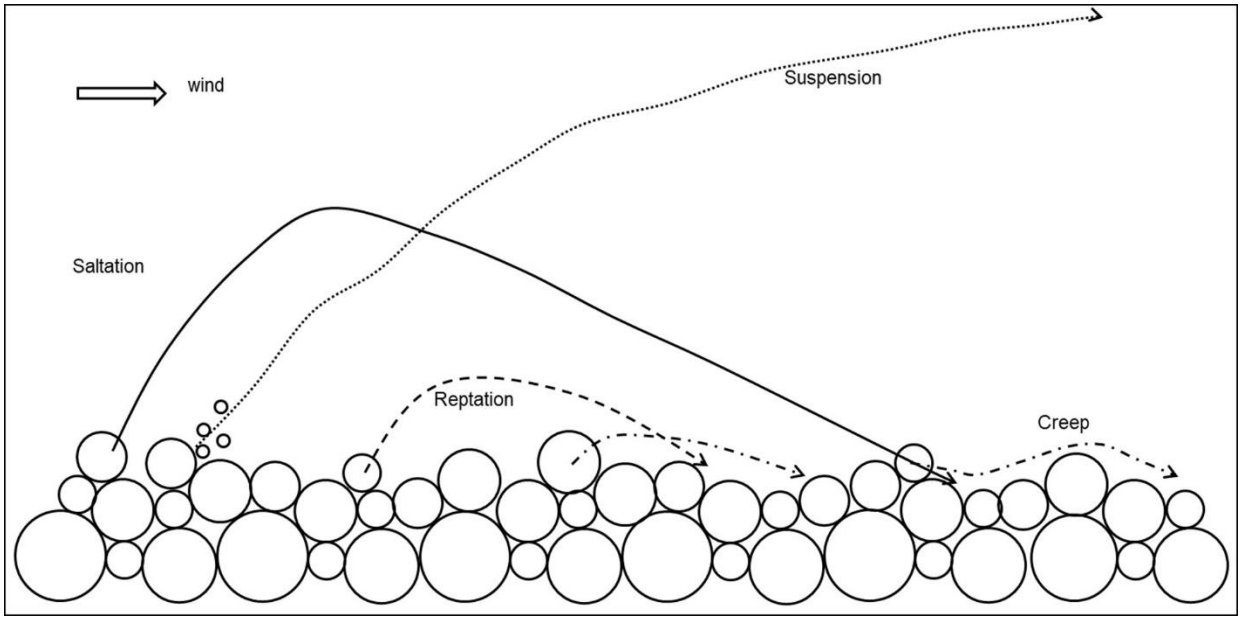

Figure 2. 1. A schematic of the different modes of wind-blown sand transport. The distinction between the creep and reptation modes is, *sensu stricto*, qualitatively and quantitatively vague, and because of that we treat both modes as creep.

The first three modes comprise the aeolian bedload and represent the conditions that account for the majority of wind-blown sand transport. Creep (sometimes referred to as traction or bed load) describes the movement of grains over a surface by rolling and sliding while maintaining continuous or near-continuous contact with the surface (Bagnold, 1937; Sharp, 1963; Owen, 1964; Williams, 1964; Howard, 1977; Walker, 1981; Greeley and Marshall, 1985; Anderson, 1987; Greeley and Iversen, 1987; Zhao and Li, 2008; Wang et al., 2009; Kok et al., 2012; Baas, 2019). Bagnold (1937) defined creep as "…grains rolled or impelled along the surface by the forward impact of grains descending from the saltation…" (p.253), a slow surface flow driven by impact of descending saltating particles. He thought that creep involved grains that are too large to be moved by the direct action of the wind and instead moving in slow

jerks caused by the impacts of saltating particles returning to the surface. One consequence of this understanding was the hypothesis that creep was responsible for changes in the size-grading of sand deposits. Bagnold also argued that creep driven by saltation impacts was unaffected by fluid drag, thus offering no resistance to the wind. Reptation involves the movement of grains in discrete hops above the surface, but with small enough momentum that their return to the surface does not usually eject other grains. Reptating grains have been termed reptons (e.g., Andreotti, 2004). Some include reptation in their definitions of the creep load (Greeley and Iversen, 1987; Werner and Haff, 1988; Anderson et al., 1991; Namikas, 2003; Lammel et al., 2012; Cheng et al., 2015a; Sherman et al., 2019), but others consider it to be a distinct, fourth mode of sand movement (Andreotti, 2004; Wang and Zheng, 2004; Duran et al., 2011; Kok et al., 2012; Baas, 2019).

Saltation involves the flight of grains above the bed over trajectories that are long and high enough to be significantly modified by momentum extracted from the near-surface wind (Williams, 1964; Anderson and Haff, 1991; Namikas, 2003; Shao, 2005; Nickling and Neuman, 2009; Li and Neuman, 2012; Ho et al., 2014; Martin and Kok, 2017). Saltating grains have been termed saltons (e.g., Andreotti, 2004). Suspension occurs in turbulent flows when mean, vertical wind speeds exceed or are equal to the fall velocity of grains, and they are, thereby, suspended or held up in the air (Bagnold, 1937; Kawamura, 1951; Anderson and Hallet, 1986; Greeley and Iversen, 1987; Daliang et al., 1990; Scott et al., 1995; Kjelgaard et al., 2004; Zheng, 2009; Rasmussen et al., 2011; Kok et al., 2012; Merrison, 2012; Ashrafi et al., 2015; Wang et al., 2015; Zhan et al., 2017). It is commonly assumed that suspension of sand-size particles is unusual and that most sand transport occurs as saltation (Bagnold, 1936; Belly, 1962; Owen, 1964; Sarre, 1987; Ungar and Haff, 1987; Anderson and Haff, 1991; Shao et al., 1996; Nishimura and Hunt, 2000; Baas, 2004; Kok and Renno, 2009; Cheng et al., 2013; Pahtz et al., 2014; Martin and Kok, 2017; Gillies et al., 2018; Pahtz et al., 2018; Liu and Bo, 2019; O'Brien and Neuman, 2019).

There remains considerable debate concerning the actual contributions of the different modes of motion to total sand transport. Of these modes, substantially the least is known of the contributions and dynamics of creep. Estimates of the creep proportion of total transport, for example, range from about 1%

(Nickling, 1978; Jerolmack et al., 2006; Gillies et al., 2012; Sherman et al., 2019; Wang et al., 2020) to 50% or more (Hijma and Lodder, 2001; Cheng et al., 2013). Part of the uncertainty arises from the ambiguous definitions for creep and part from the experimental challenges involved in measuring the phenomenon.

For the purposes of this review we adopt a definition of creep transport that includes reptation and consider the terms creep and reptation to be interchangeable unless otherwise noted in the text. In adopting this definition, we refer to the original Latin word *reptilis*, which means creeping and is the basis of reptile. The definitions of modes of motion are posed as if there are distinct transitions from one mode to another. In actuality there is a continuum that transitions through the stages from creep to saltation and to suspension as the strength of the wind increases: each mode in the sequence generally requiring greater shear stress than its predecessor. However, as a more energetic transport mode is achieved, there may still be significant sand transport via the less-energetic modes. Aeolian transport as suspension (involving mainly dust) and saltation load have received substantial attention in the literature, and these modes have been reviewed thoroughly (Shao and Raupach, 1993; Zobeck et al., 2003; Kjelgaard et al., 2004; Roney and White, 2004; Li and Guo, 2008; Goossens and Buck, 2011; Kok et al., 2012; Li and Neuman, 2012; Barchyn et al., 2014; Ashrafi et al., 2015; Mayaud et al., 2017; Martin and Kok, 2018; Sherman et al., 2018; Baas, 2019; Sherman, 2020). Much less attention has been devoted to understanding creep, an oversight we aim to redress through this review.

The goals of this review are to describe the fundamentals of creep transport under different wind and sediment conditions, the methods used to measure or estimate creep flux, and the major findings of the relevant studies. Reviewing the state of creep research is important for: 1) general understanding of wind-blown sand processes; 2) specific understanding of the creep process and its relative contribution to total sand flux (ignoring suspension); 3) describing the development and movement of wind ripples; and 4) developing terrestrial analogs applicable to extraterrestrial surfaces (e.g., Mars or Titan). We address the physics and different mechanisms of creep and summarize the key results from laboratory, field, and model studies, especially with regard to the contribution of creep flux to total sand transport, i.e. q_c/q (q_c

is creep transport rate, q is total sand transport rate. We report q_c/q as %, and assume that $q = q_c + q_s$ (q_s is saltation transport rate)). The relationships between q_c/q and controlling variables such as wind speed, grain size, and fetch length, as detailed below, remain ambiguous and the results reported in the literature are often contradictory. If the contribution of creep to total sand flux is small, then the issue is of little practical importance. If, however, $q_c/q \geq 25\%$, as has often been reported, then our sand transport models, if they are based solely on saltation, remain naïve. Models to distinguish creep contributions are then important for applications in geo-archeology, paleo-environmental reconstruction, stratigraphy, climate change, and, most immediately, sand transport prediction and consequent land surface changes. Our focus on creep in the sand transport system stems from the belief that understanding the process is a key element toward understanding landforms (Brunsden and Thornes, 1979) and this allows us to bound the review. Creep plays an important role in producing and modifying common ripples on Earth (decimeter-scale wavelength), large ripples on Mars (meter-scale wavelength), megaripples, transverse ridges, or other local small-scale geomorphological signatures in many aeolian environments on Earth and Mars (Seppala and Linde, 1978; Manukyan and Prigozhin, 2009; Zimbelman, 2010; Kerber and Head, 2012; Foroutan and Zimbelman, 2016; Lapotre et al., 2016; Cheng et al., 2018; Lammel et al., 2018; Yizhaq et al., 2019). In some cases the direct role of creep may be uncertain (Lapotre et al., 2016), but in others the concepts and models of creep transport rates are invoked to describe, especially, the evolution and migration of large bedforms (Lammel et al., 2018; Yizhaq et al., 2019; Silvestro et al., 2020; Sullivan et al., 2020). There is a large, vibrant, and fast-expanding literature concerning these creep-related bedforms, but their treatment is beyond the scope of this review.

The Nature of Creep

Traditionally-defined modes of sediment transport are bed load (or traction load) and suspended load (e.g., Gilbert and Murphy, 1914; Einstein, 1950; Van Rijn, 1993). In suspended load, particles are supported in the transporting fluid when the vertical turbulent velocities are equal to or faster than the particle settling velocity. In aeolian systems, suspension is mainly limited to particles in the silt and clay size classes. In bed load, moving grains are supported mainly by interactions with the bed, including close

contact by sliding and rolling; movement in short hops (often termed reptation); or by saltation, where grains bounce along trajectories of lengths that are several orders of magnitude longer than grain diameters. Saltation is largely, but not entirely, constrained to grains within the range of sand sizes: 0.0625 – 2.00 mm. In aqueous environments the distinctions between the different types of bed load are muted because the density ratio between sand and water is about 2.6 and saltation trajectories usually remain within a few tens of grain diameters of the surface (Bagnold, 1973). This makes distinction of creep and saltation motion difficult. In aeolian transport, saltation trajectories are much higher and longer than they are in water, and this makes the distinction between creep and saltation modes easier. Most creep occurs within a layer a few millimeters above the surface and most saltation trajectories rise above that height. Changes from creep to saltation in a transport system, however, occur along a gradient of motions, defined mainly by trajectory heights, obviating absolute physical distinctions of one from the other.

For the purpose of this review we distinguish two forms of aeolian creep: fluid and impact creep. Fluid creep is the form of motion which is driven solely or mainly by fluid forces exerted on grains. Impact creep is that which is driven solely by the impacts of saltating grains at the ends of their trajectories. These are polar definitions for the organization of our review. In reality, most of the time creep is driven by combined fluid and impact forces except for conditions at or near the fluid threshold of motion when impact forces are absent. Under most transport circumstances, impact creep will contribute much more to total sand flux than fluid creep. The distinction, however, remains important because of implications for transport over lag surfaces or where grain populations are multi-model, such as those often reported for Martian surfaces (Baker et al., 2018; Foroutan and Zimbelman, 2020). In such environments the role of either mode of creep might be exaggerated relative to creep involving aeolian sand populations that are typically well graded (Bagnold, 1936; Valance et al., 2015; Sullivan and Kok, 2017).

Our search of the literature revealed 154 articles that discussed the occurrence and nature of creep motion in wind tunnel, field, and modeling studies, and 30 articles that focused on creep transport rate

studies, of which 24 included reports on q_c/q. Key elements of the 30 articles are summarized in Table 2.1, in the discussion section below. The literature on creep transport rates and the relative proportions of creep flux are at the heart of the review. Many more articles, too many to review or cite, make incidental mention of creep. Most studies on the initiation of motion, for example, will make at least passing mention of creep as grains begin to move (Creyssels et al., 2009; Kok et al., 2012; van Rijn and Strypsteen, 2020). These are reviewed only incidentally herein. We also do not review the set of papers concerned with ripple migration rates in sand-size sediments, except as they are related to creep transport equivalence e.g., Jerolmack et al., (2006); Andreotti et al., (2006). The relevant sand-size ripple migration literature was reviewed in Sherman et al. (2019). For this review we organize discussion of the literature based on the nature of creep study, approaches to measure or estimate creep flux, the contribution of creep flux to total transport, discussion on creep studies, and three main conclusions about creep.

Fluid creep

When wind blows over an unconsolidated sand surface it exerts drag (F_D) and lift forces (F_L) on grains. The grain will be dislodged when a threshold velocity (u_t), or threshold shear velocity (u_{*t}), is surpassed. At the threshold condition, the fluid force (comprising drag and lift forces), F_f is exactly sufficient to balance the resisting force of gravity, F_G (Figure 2.2):

$$F_f(cos\alpha_1)a_1 = F_G(sin\alpha_2)a_2 \qquad (1)$$

where α is the pivot angle around which a grain must rotate, α_1 is the angle between fluid force direction and the direction of fluid force projected on the motion direction, α_2 is the angle between gravity direction and the direction perpendicular to the motion direction, and a_1 and a_2 are the moment arms for the fluid force and gravity force, respectively. The importance of lift force at the initiation of motion is controversial and many argue that the drag force is substantially most important (e.g., Chepil, 1961; Bagnold, 1973; White and Schulz, 1977; Andreotti, 2004; Valance et al., 2015). This underpins Anderson's (1989) argument that because the drag force dominates over the lift force, grains tend not to leave the bed vertically, but rather pivot out of their pockets up into the higher velocity flow. The grains

may then roll or slide as fluid creep until they encounter other grains and are blocked or they may contribute to the movement of other grains. Because of the range of grain sizes and pivot angles that characterize natural sand surfaces, there is no single threshold condition for the entire surface. As wind speed increases over a surface there will be sporadic motion of grains from different areas. As described by Bagnold (1936) from his wind tunnel experiments, most fluid creep will be of short duration and at a constant wind speed it will stop and the surface stabilizes. This type of temporary creep has been described in several other studies concerned with grain behavior near the fluid threshold of motion (Willetts et al., 1991; Li and Martz, 1995; Sullivan and Kok, 2017; Swann et al., 2020) where wind speeds are not sufficient to induce sustained saltation.

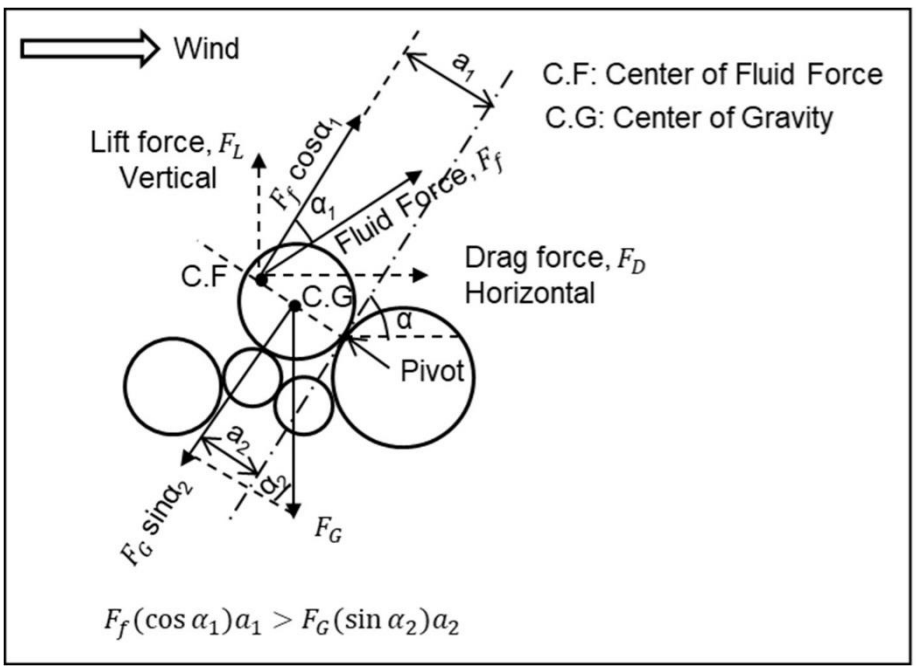

Figure 2. 2. Forces on a grain and the mechanics of the initiation of (modified from Middleton and Southard (1984). Here, α is pivot angle and a_1 and a_2 are moment arms for F_f and F_G

In natural environments, fluid creep at wind speeds near the threshold for motion is common. Although it may be a locally a temporary phenomenon, turbulent velocity fluctuations may continue to move patches of sand over different parts of the surface. Some of these patches, if they last long enough, will include transport that has transitioned to saltation (Carneiro et al., 2015; Sullivan and Kok, 2017), as it is common for fluid creep to precede saltation as grains gain momentum after leaving their immobile

state. Bagnold (1936) described grains rolling and bouncing for perceptible distances before attaining the momentum to transition to saltation. The wind tunnel experiments of Willetts et al. (1991) demonstrated that even with shear velocities well above the threshold for motion, most grains will creep before saltating, a process described in numerous other laboratory studies (e.g., Chepil and Milne, 1939; Greeley and Marshall, 1985; Greeley and Iversen, 1987; Burr et al., 2020; Swann et al., 2020). Contradictorily, Bisal and Nielsen (1962) and Lyles and Krauss (1971) argue that most grains are ejected from the bed directly into saltation. These observations were partly corroborated by the results of Nickling (1988), who observed creep and direct saltation at the initiation of motion. Calder and Smith (1990) developed a theory which explained the direct entrainment to saltation without a creep phase, based on a model for saltating grains in water by Wiberg and Smith (1985).

In a different sense of fluid creep, Pähtz et al. (2020) used the term "creep" motion to describe an irreversible, superslow granular motion associated with sporadic microscopic rearrangements of grains, typically an intermittent flow that occurs below a macroscopic yield threshold. This describes the mechanisms of creep initiation from a perspective of local rheology, although presently minimal evidence supports the concept.

Impact creep

With fluid creep on the surface and a sustained or increasing wind speed, a number of grains will gain sufficient momentum from the wind or from the impact of other creeping particles to be ejected to elevations well above the surface (relative to grain diameter). As the grains rise they extract momentum from the wind, accelerate, and then return to the surface with increased momentum. When these grains return to the surface, they rebound and splash other grains into saltation and dislodge some grains as high or low energy impact creep or cause local grain vibration. Mitha et al. (1986), in their wind tunnel studies of saltation-induced grain splash, categorized the scattered grains as what we would recognize as a high energy salton and a number of low energy reptons. These experiments provided the basic details for the "splash function" model of Ungar and Haff (1987), which plays a central role in simulating saltation motion.

The nature of saltation splash has been investigated mainly with regard to the number of grains moved by impacts and the angles and velocities of ejected particles (Mitha et al., 1986; Willetts et al., 1986; Haff and Anderson, 1993; Zheng et al., 2005; Zheng et al., 2006; Creyssels et al., 2009; Gordon and Neuman, 2011; Ho et al., 2012; Lammel et al., 2017). Many, perhaps most, of the grains mobilized by impact are not promoted to saltation, but move rather as creep (Rice et al., 1995; Lammel et al., 2012; Zhang et al., 2016). Andreotti's (2004) model indicates that impact creep is the common precursor to saltation as grains bounce progressively higher once they have been motivated and may or may not transition to saltation. This model is partially based on that of Owen (1964, p. 226), who suggested that the air-borne shear stress at the surface "…is just sufficient to ensure that the surface grains are in a mobile state." With saturated, or equilibrium, sand transport, therefore, we would find coincident fluid creep, impact creep, and saltation, and this is seen in several, slow-motion videos available online.

Two mechanisms drive impact creep. First, there may be a relatively low-energy impact creep caused by vibrating grains nudging others into motion, or associated with local rheology, or by impacts between creeping grains (Bisal and Nielsen, 1962; Owen, 1964; Sarre, 1987; Hardisty and Whitehouse, 1988; Nickling, 1988; Spaan and Van den Abeele, 1991; Hoyle and Woods, 1997; Pahtz et al., 2020). This source of creep transport usually will not contribute substantially to the total transport rate when there is also saturated saltation. Much more important is the second, higher energy source of impact creep, that is driven by the impacts of saltons upon their return to the surface (Andreotti, 2004).

Review of literature

Creep studies

We consider here the importance of creep mainly with regard to its contribution to total aeolian sand flux and focus on the limited number of creep-specific studies. Results of those studies point to widely divergent estimates of the role of creep as a factor in sand transport, caused, in part, by the technological and methodological challenges in defining and measuring creep. Advances in detection and measurement of creep have been made (detailed below), but standardized protocols have not been adopted. Methodological innovations have lagged those for the measurement of wind and saltation

systems (e.g., Sherman, 2020), perhaps because of the general perception that creep motion is not critical to understand wind-blown sand transport rates. The shortcomings are especially evident in field studies where only a few approaches have been applied, whereas laboratory experiments have become much more sophisticated. Progress has been slow in the three decades since Anderson et al. (1991) argued the necessity of direct observation of near surface grain movement in order to properly validate postulations. In this section we will first review the different methods used to measure or estimate creep transport rates, and then discuss field studies, wind tunnel studies, and modeling studies, in turn.

Method

Quantifying creep transport rates in field and laboratory studies has mainly involved application of methods that relied on sand (creep) traps, curve fitting, ripple migration surrogates, particle-tracking velocimetry (PTV), and sedimentological approaches. The methods discussed here and their applications are summarized in Table 2.1.

Sand traps

Most direct attempts to measure creep transport involve the use of sand traps, including buried traps and near-surface vertical traps. In this section, we review the methods to measure creep rates by different types of sand traps.

Bagnold designed a buried, slot-type trap to capture creep load (Figure 2.3 (a)). The creep trap (Bagnold, 1937) used in his wind tunnel had an opening described as a 20.0 x 5.0 mm rectangle oriented with the long axis perpendicular to the wind. In Bagnold's (1938) Figure 3, however, the version used in the field had an opening that appeared much larger, approximately 40 x 10 mm (if the figure is to scale). One drawback of this type of trap is that some saltation is able to fall through the slot, and the wider the slot the more likely that this will happen. To the degree that occurs, creep transport will be over-estimated.

In a series of experiments concerned with soil erosion by wind, scientists with the Canadian Soil Research Laboratory (e.g., Chepil and Milne, 1939; Chepil and Milne, 1941; Chepil, 1945), measured creep and saltation transport using Bagnold-type traps. The dimensions of the traps they used were not

specified, so the size of the trap slot(s) and thus the potential that creep and saltation flux are comingled, cannot be estimated. Nickling (1978) also used a Bagnold-type slot trap in his field experiments, but orientation issues led him to adopt a circular-intake orifice 1.0 cm in diameter. He took care to keep the opening as close to the surface as possible to reduce the effects of scour when the bed was eroded or the effects of grains being funneled into the trap when the bed was elevated by accretion. He et al. (1990) also used a buried creep load trap in their wind tunnel study, but of very different design and scale. This trap comprised a buried triangular prism with a slot at its apex that was 8 mm wide with a 400 mm spanwise length (Figure 2.3 (b)). The trap was positioned so that the opening was flush with the sand surface. Hijma and Lodder (2001) used a large buried box as a collector, gathering creep through a 10 mm x 500 mm slot.

Butterfield (1991) built a direct vertical creep (reptation) trap (Figure 2.3 (c)) based on a design intended to solve the problem of scouring around the base of traps. The trap has a rectangular aperture 22 mm wide × 14 mm high and a downward duct section to convey the slow moving grains to a buried reservoir. Butterfield credits Rasmussen and Mikkelsen (1991, but cited as in press) with the design, presumably a version of the wedge trap published in Rasmussen and Mikkelsen (1998), but developed much earlier.

A creep trap based on the Big Springs Number Eight (BSNE) trap (Stout and Fryrear, 1989) was used by Stout and Zobeck (1996) in their field study. They measured sediment (mainly sand) transport at three elevations within the first 20 mm above the surface. The lowest trap spanned the elevation from 0-3 mm (Figure 2.3 (d)) and Stout and Zobeck (1996) considered sediments captured in this lowest trap to represent creep transport. The design of this creep trap was adopted for the commercially-available trap marketed by Custom Products and Consulting, LLC (of Big Springs, Texas) and it has been used in the field experiments of Zobeck et al. (2003), Sharratt et al. (2007), Feng and Sharratt (2007), Sharratt and Feng (2009), Pi et al. (2014), Hedding et al. (2015), and Pi et al. (2016). One drawback of this design is that the vertical opening, although small, will catch some saltation in addition to creep load.

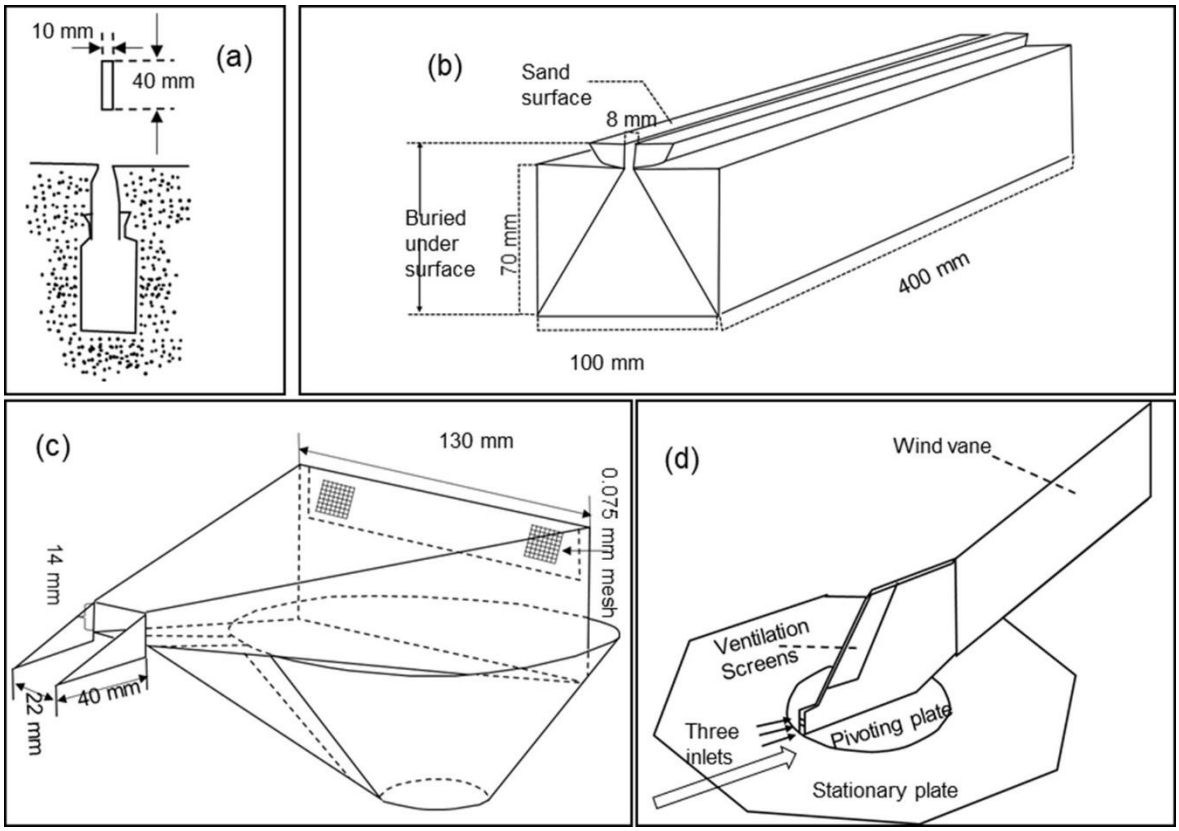

Figure 2. 3. (a) Bagnold (1938) buried slot trap: field version. (b) He et al. (1990) buried slot trap. (c) Creep (reptation) trap used by Butterfield (1991), based on a design later published in Rasmussen and Mikkelsen (1998). (d) Stout & Zobeck (1996) trap, measuring creep caught in the lowest of the three inlets depicted.

Qi et al. (2001) used a Bagnold-type approach in their wind tunnel study. Instead of involving a slotted aperture leading to a buried container, however, they used a trench-style trap (Figure 2.4 (a)) in the sand bed. The up-wind side of the trap was vertical and the down-wind side was about 30° off vertical. This trap is also susceptible to sample contamination by saltation.

In sets of field experiments, Yang et al. (2011) and Liu et al. (2014) used creep traps of unspecified design to measure transport from the secondary intercardinal compass points. The trap was oriented and buried with the sixteen slot openings, each with its own sand collector, aligned perpendicular to the respective compass point. According to Liu (personal communication) one drawback with the design is that sand drifting across the trap could be captured by any one or all of the individual traps, thereby complicating the interpretation of directionally specific transport.

Gillies et al. (2012) used a set of six, 27 x 255 mm slot-type traps (similar to Bagnold's slot trap), aligned relative to local bedform crests. The relatively wide slot mouth was chosen because of the coarse nature of sediments. In this study, the authors also used colored, faceted, tracer particles with diameters up to 14 mm to measure multiyear creep rates.

Swann and Sherman (2013) designed a bedload trap with a square opening adjusted to be flush with the sand surface, allowing creep and saltation to enter a chimney. Within the chimney was a barrier designed to segregate the modes of transport so that creep fell to the front of the trap and saltation to the rear, using a 45° internal angle for the barrier (Figure 2.4 (b)). Swann used this same design to detect the initiation of fluid creep.

In a wind tunnel experiment, Wang et al. (2020) designed and deployed a trap to measure creep and saltation loads (Figure 2.4 (c)). The operational concept is that saltating grains will return to the surface at angles greater than 9° and not be able to enter the opening of the creep trap, instead being caught by the saltation trap. The effectiveness of this design hinges on the effectiveness of the trajectory segregation, discounting some of the natural variability in sand transport (see Table 2.1 in Swann and Sherman, 2013). It is also unclear how creep transport is driven through the 15 mm long path beneath the shelter of the bottom of the saltation trap and how all saltation is excluded.

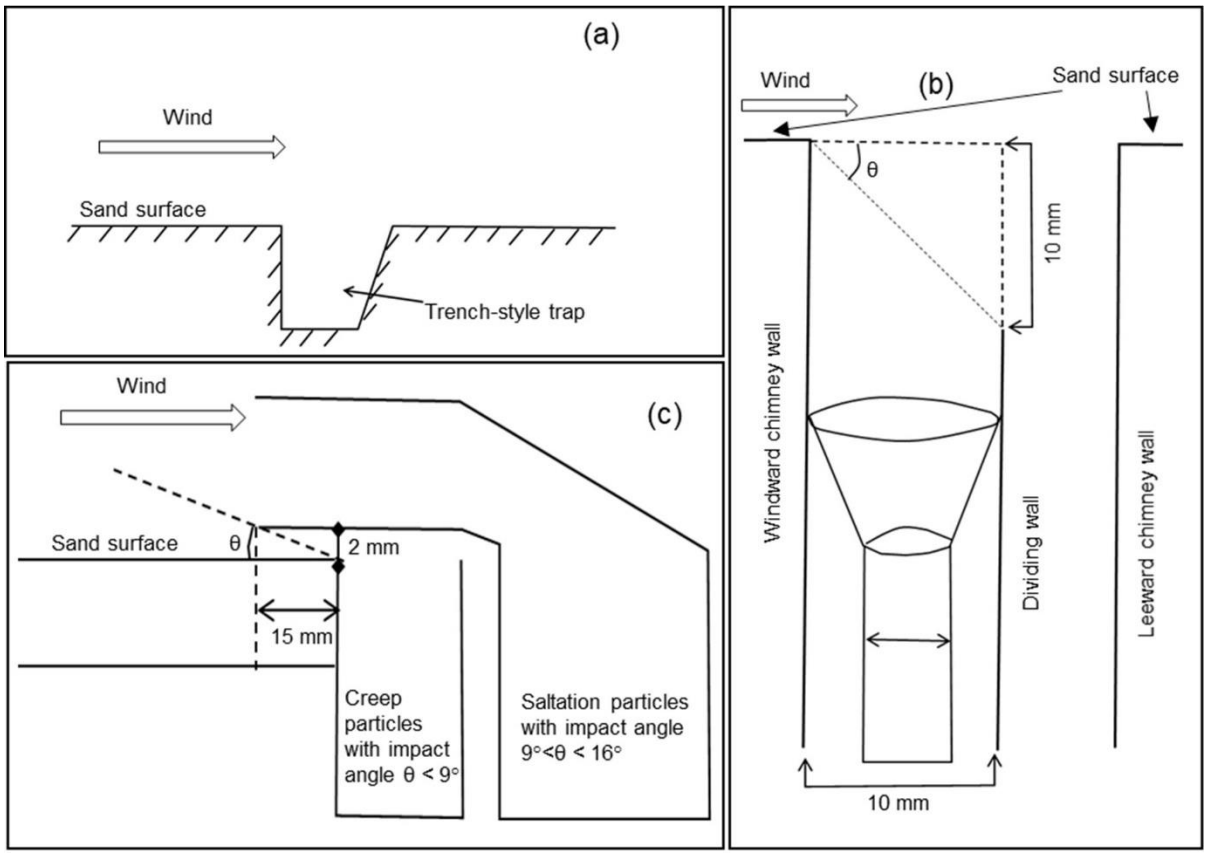

Figure 2. 4. (a) Trench style strap (adapted from Qi et al., 2001). Dimension of the trap was not reported in their paper. (b) Swann and Sherman (2013) trap, where grains fall through a surface flush, horizontal orifice. (c) Wang et al. (2020) trap, where grains enter through a surface flush, vertical orifice.

Curve fitting

Curve fitting methods have been developed to quantify creep transport rates from data obtained from either horizontal or vertical traps arrays. Horikawa and Shen (1960) tested three trap designs (Figure 2.5 (a)) with capability of providing creep transport data. Their H-1, horizontal, compartmentalized trap captured creep and saltation in its windward compartment. Their V-2 and V-4 traps were designed to capture creep separately from saltation through 10.3 mm wide surface flush slots (Figure 2.5 (a)) located just upwind of vertical saltation traps. They used only H-1 data to estimate creep transport rates as they deemed the other creep trap data unreliable. The saltation mass caught in that trap showed a systematic horizontal distribution and a curve was fit to the data (Figure 2.6). The substantial excess sand caught in the upwind trap compartment, relative to the mass predicted by the curve, was identified as creep. Most analogous methods have relied on vertical, rather than horizontal distributions based on trap data and

empirical distribution fitting. For example, Dong et al. (2003) measured the distribution of sand flux in a wind tunnel with a vertical array of 60, 10 mm high x 5 mm wide traps. They used their data to fit the exponential function $q_h = ae^{(-z/b)}$, where q_h is the transport rate at elevation z, and a and b are the fitting parameters. Dong et al. (2003) suggest that a, the y-intercept, represents the creep flux and used that relationship estimate creep transport relative to total transport. This approach was used by Namikas (2003) who measured vertical flux profiles with 15 traps distributed from the bed surface to 0.35 m above the surface and used the data to fit an exponential distribution to the profiles. Yang et al. (2011) and Han et al. (2012) also used this method with their vertical flux data. A distinction between their vertical flux profile approaches and that of Horikawa and Shen (1960) is that the latter did not use the y-intercept to estimate creep but used instead the mid-point width of their upwind trap (as depicted in Figure 2.6).

Vertical sand trap designs were also tested by Rasmussen and Mikkelsen (1998) in a wind tunnel study. They mention that two of the trap types are capable of capturing creep: their isokinetic trap with one of its suction tubes mounted flush with the surface, and a similarly mounted Ames trap (Greeley et al., 1982). They indicated short-comings with both trap types, and no creep transport data were reported in the paper. The traps suggested by Rasmussen and Mikkelsen (1998), and similar surface deployed traps (e.g., Rasmussen and Sørensen, 1999; Gu and Guo, 2007; Rasmussen et al. 2011), do collect creep, but it is mixed with saltation. Estimations of creep load can be made, however, from vertical flux profiles as described above.

Wu et al. (2011) used two types of horizontal sand traps, each divided into five, 10 mm wide compartments. One of the traps was deployed with its compartments flush with the sand surface and the other with its compartments recessed 30 mm below the sand surface (Figure 2.5 (b)). By comparing the amount of sand collected by the two types of traps, they argued that an efficient creep trap should include a recessed slot with 2 cm wide opening.

Cheng et al. (2013) developed an ingenious method to estimate creep transport using a series of slot-type traps (Figure 2.5 (c)) with different flow parallel widths. They first experimented with a number of slot widths as narrow as 0.45 mm, finding that slot apertures needed to be more than 0.75 mm so that

they would not be clogged by the sands that they used. They settled on a set of traps with opening slot width 1, 2, 3, 4, 5, and 6 mm wide, each 20 mm long. Their reasoning is that for given sand and wind conditions, the creep mass caught by the different traps should be the same. The saltation load caught, however, should increase with trap width. They fit linear regression lines of sand transport rate against slot width and interpreted the "y" intercept as representing creep flux.

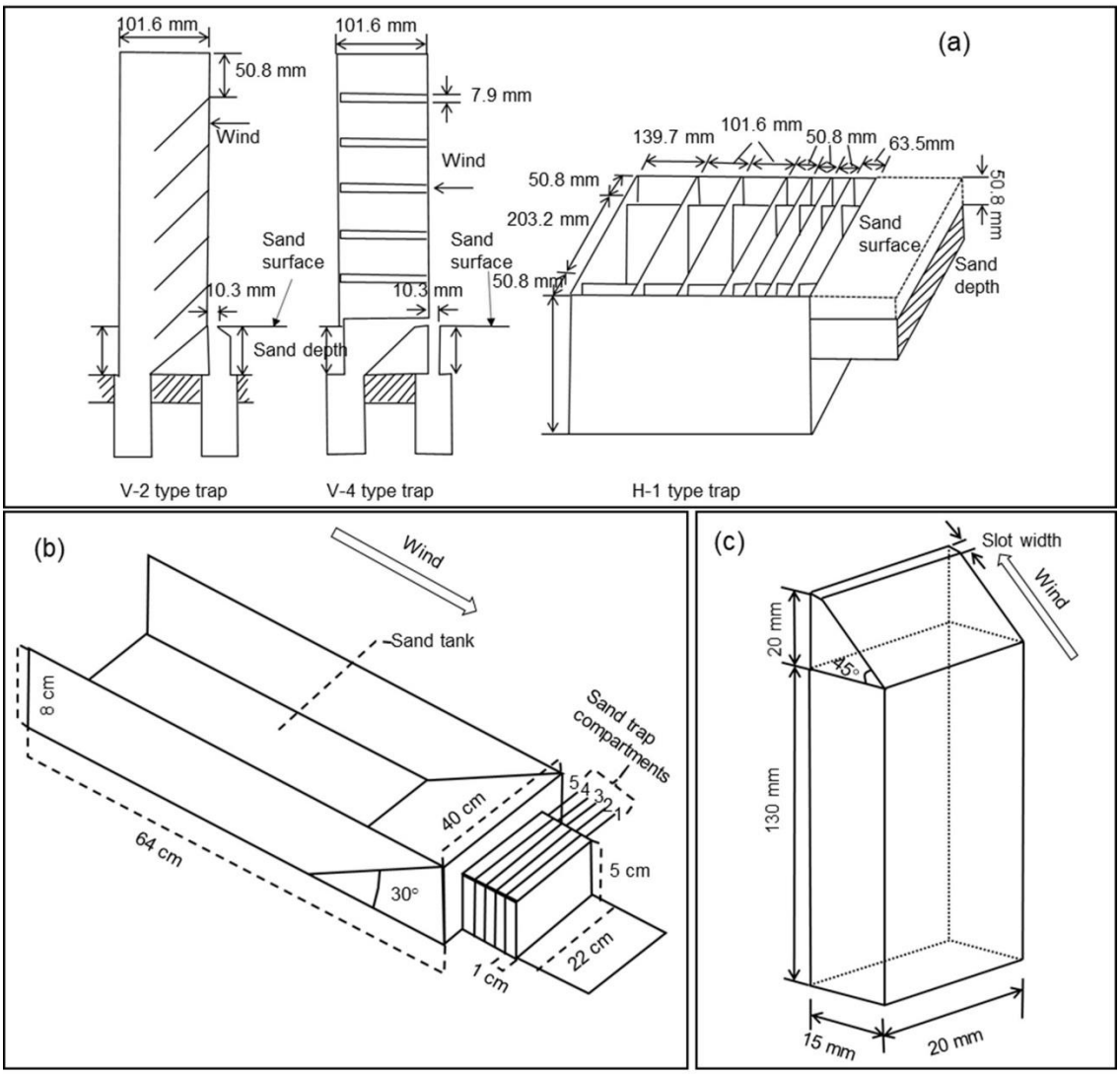

Figure 2. 5. (a) Three creep trap designs tested by Horikawa and Shen (1960). The H-1 type trap was used for the development of their analytic method. (b) The slot type trap of Wu et al. (2011). The slot openings were recessed below the sand surface. (c) Buried slot trap of Cheng et al. (2013). The opening slot width varied with 1, 2, 3, 4, 5, and 6 mm wide.

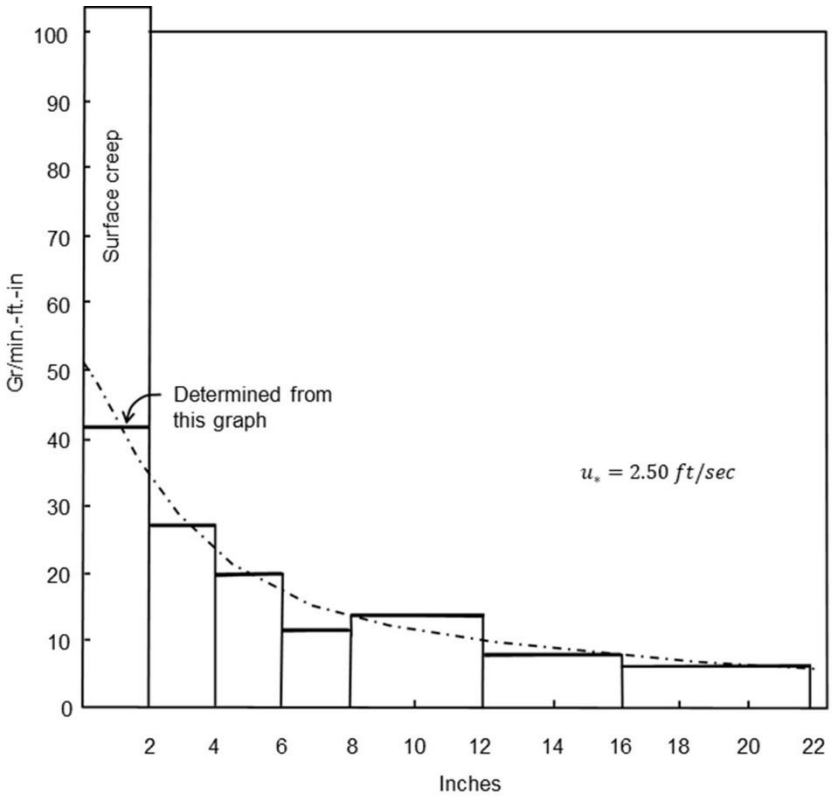

Figure 2. 6. The method of Horikawa and Shen (1960) for estimating creep transport based on measurements from their H-1 type trap.

Ripple migration surrogates

Bedform migration rates are often associated with bedload transport rates in natural environments (Miles et al., 2014) and Bagnold (1941, p. 146) indicated specifically that ripple migration is a manifestation of aeolian creep. Measurements of ripple migration rates, u_r, represent creep transport rates, q_c, according to:

$$q_c = (1 - P)\rho_s u_r H/2 \qquad (2)$$

where P is porosity (usually ~ 0.4), ρ_s is sediment density, and H is ripple height. Migration rates have been measured directly (e.g., Cornish, 1914; Sharp, 1963; Borsy, 1973; Isenberg et al., 2011; Zhu, 2011; Gillies et al., 2012), but the use of indirect methods is much more common. These methods include photogrammetry (Seppala and Linde, 1978; Walker, 1981; LING et al., 2003; Andreotti et al., 2006; Yizhaq et al., 2009; Silvestro et al., 2010; Isenberg et al., 2011; Lorenz, 2011; Lorenz and Valdez, 2011;

Zhu, 2011; Cheng et al., 2018; Sherman et al., 2019), 3D laser scanner (Neuman and Bedard, 2017), and laser distance sensing (Boulton, 1997; Sherman et al., 2019).

Direct measurement of ripple migration rates involves a ruler or tape to measure displacement over time, relative to some reference point. Jerolmack et al. (2006) and Gillies et al. (2012) measured the displacement of coarse grain ripples over time to obtain migration rates, thus inferred those as creep transport rates. Zimbelman et al. (2009) used similar methods with flags planted on the crests of granule ripples.

Most photogrammetric approaches that quantify ripple migration rates use time series of images to record ripple movement relative to a fixed reference point (e.g., Andreotti et al., 2006; Zimbelman et al., 2009; Isenberg et al., 2011; Sherman et al., 2019), or as they pass through a time series of rectified image frames. In these cases, ripple height or spacing are either measured independently (by hand, for example) or estimated from the photographs. A more technical approach was the photogrammetry-based stereo technique used by Yizhaq et al. (2009) and Isenberg et al. (2011). They mounted a camera on a rail that allowed the camera to be translocated along a known geometry. Using ground control points and sets of photographs taken transverse to ripple crest orientation, they were able to develop digital elevation models of the megaripples. They used Erdas Imagine and its Leica Photogrammetry Software extension (LPS) to extract ripple height, wavelength, and slope. To trace the ripple migration rates, Isenberg et al. (2011) made repeated transverse scans at intervals that were short relative to the megaripple speeds.

Andreotti et al. (2006) used repeat photography and an inclined laser sheet to measure ripple geometry and speed. The low-angle sheet illuminated a line across the sand bed and that line was photographed. An autocorrelation function reproduced the ripple profile at each time step. McKenna Neuman and Bédard (2017) used a 3D laser scanner to produce high-resolution (<0.01 mm) DEMs of the surface. Each scan required about 2 minutes to complete, and during that time the wind tunnel was stopped. Repeat scans were conducted at run-time intervals that ranged from 1 – 20 minutes, dependent on the rate of bed evolution. Sherman et al. (2019) used a flow-parallel pair of laser distance sensors, 60 mm apart, to measure surface elevation changes caused by ripple migration. The time required for a ripple

to move the 60 mm distance from one sensor to the other (using ripple crests, for example) was used to estimate migration rates.

Particle-tracking velocimetry (PTV)

Applying photogrammetric approach, Wang et al. (2009) and Zhang et al. (2016) used high-speed (500 frames per second) digital photography with a particle-tracking velocimetry (PTV) algorithm to trace velocities and mesoscopic features of creeping grains. The methods include pre-processing steps to reduce the image noise and extract particle motion. Flux is measured by counting the number of grains crossing a virtual line in sequential images.

Sedimentological approaches

A few studies have estimated creep based on the assumption that large grains are only moved as creep. This method was used by Zhu et al. (2014), who analyzed the grain size distributions of samples and assumed that the proportion of grains larger than 0.5 mm was moved by creep. Qian et al. (2015) used the same method but used $d \geq 1.15$ mm as the creep threshold. Liu et al. (2017) assumed that grain sizes in the range of 0.5 – 2 mm moved as creep at their field site.

Results

Field studies

The earliest field effort to measure creep transport and associated wind data that we found is Bagnold's experiments in the Libyan Desert (Bagnold, 1938). He used a vertically segmented trap and creep trap to measure saltation and creep. He added the sand masses from the two types of traps to obtain estimates of total transport and used that sum to obtain the relative load moved as creep. No specific results were reported in his paper, but he did make the general statement that the field measurements confirmed his wind tunnel finding that creep transport accounted for about 25% of the total transport rate. It is clear that Bagnold's trap would capture more than just creep, as saltating grains landing in the slot or the funnel-like depression around the trap would also fall into the trap.

Nickling (1978) conducted a field experiment to measure creep transport (described in section 3.1.1) during dust storms in Yukon Territory, Canada. He found the mean proportion of creep movement

was about 4.6% of total, non-suspended, transport (q), with a range 2.3 – 7.9%. The small creep percentage, compared to Bagnold's findings, was ascribed to the presence of very fine sands and silts and the irregular nature of the surface. It is likely that Nickling's use of his trap was more efficient than Bagnold's in excluding accidentally trapped saltation because the trap orifice was kept as close to the surface as possible.

In a reassessment of the Stout and Zobeck (1996)(1996) data set, Zobeck et al. (2003) reported that creep can make up to 40 percent of the total sediment flux, based (apparently) on data presented in Stout and Zobeck's (1996) Table 3. This is one of the largest proportions of creep transport reported in the literature. It is likely that some unknown portion of sediment caught in the lowest trap would have been moving as saltation rather than creep.

The relationship between the amount of creep transport and shear velocity was explored by Hijima and Lodder (2001) who found a best-fit power function $q_c = 0.0175u_*^{1.64}$ for their data from the Netherlands. When compared to the total sediment transport, they found that creep accounted for 13 – 54% (digitalized from their Figure 22) of total transport. Based on the model that they tested with their data, total transport increased with a relationship $q = 0.2166u_*^{2.97}$. According to the two relationships with u_*, total transport must increase faster than creep, and the latter will be a decreasing component of sand transport as u_* increases.

Namikas (2003) reported creep based on vertical flux profiles obtained at Oceano Dunes, California, USA. He found an exponential function of the same form as Dong et al. (2003), that always underestimated the transport at lowest elevation (within 10 mm of the surface). He defined the "excess" flux at the lowest elevation as creep and found that the creep transport accounted for about 10% of the total load.

Yang et al. (2011) measured sediment transport during sandstorms in the Taklimakan Desert of China. Mean grain sizes ranged from 0.063 – 0.125 mm. Comparing their creep and saltation trap data they found that q_c/q was in the range of 2 – 30%. They also estimated creep transport by fitting vertical

flux profiles, finding that creep accounted for about 12% of total transport. Liu et al. (2014) measured creep transport in the Ulanbuh Desert of China using the same creep trap as Yang et al. (2011). The mean grain sizes at the site varied from 0.100 to 0.152 mm. Based upon a digitization of their Figure 6f, it appears that creep transport accounted for about 5 - 11% of the total transport rate during their study.

In a multiyear project in the Wright Valley of Antarctica, Gillies et al. (2012) measured the movement of creep with a set of six buried traps. The dominate, mean grain-size collected by the creep traps was 1 mm. Most transport occurred as saltation with q_c/q about 0.2%. The large proportion of saltation transport relative to similar studies was likely caused by a slow moving, coarse-particle creep load and a saltation load comprising finer sands (mid-range d = 0.5 mm).

Han et al. (2015) used a portable wind tunnel at nine field locations with altitude ranging from -154 m (below sea level) to 5076 m to test the influence of air density on aeolian sand transport. They used a vertical sand trap with 25 compartments in a 0.5 m high array. They used the methods of Dong et al. (2003) to estimate creep transport. Their results show that q_c/q varied from 10 - 32.5%, decreasing with wind velocity. The creep proportion with denser air (0.869 and 0.990 kg/m^3) ranged from 22.5 to 32.5% and was greater than that with less dense air (0.676 and 0.761 kg/m^3), ranging from 10 to 23%.

Studies of ripple migration rates were reviewed or described in Sherman et al. (2019), including four that were detailed enough that migration (creep) rates could be compared to shear velocity and/or total transport rates (Sharp, 1963; Andreotti et al., 2006; and their two original studies). The Sharp (1963) and Andreotti et al. (2006) studies did not measure total transport rates so there can be no comparison of creep to total sand flux. Sherman et al. (2019) reported field measurements from Jericoacoara, Ceará, Brazil, and from Oceano, California, USA (as described above). In the former, ripple migration rates were compared to estimates of shear velocity from ultrasonic anemometers and measurements of total transport made with arrays of mesh traps (Sherman et al., 2014). In the Oceano experiments, shear velocity was derived from ultrasonic anemometer data and total transport rates from vertical arrays of BSNE traps. The Jericoacoara data indicated that creep transport averaged about 5% of total transport. At Oceano the average was about 2.5%.

Several studies consider the role of creep in environments with sediments coarser than sand or where megaripples were present. Jerolmack et al. (2006) estimated creep flux based on the migration rates of coarse-grained ripples comprising 0.10 to 1 mm diameter gypsum and 1 to 3 mm diameter siliciclastic particles at White Sands National Monument, USA. They measured saltation transport by one trap with five vertical segments and integrated the saltation flux between 0 – 4.5 m above the surface. The creep proportion was estimated as about 1% of the total flux.

Zimbelman et al. (2009) measured the migration of granule ripples at Great Sand Dunes National Park and Preserve, USA, and used equation (2) to calculate creep transport rates. Mean grain size was about 1.5 mm. They measured coincident wind speeds of about 9 ms^{-1} at a height above 1 m, but did not report associated shear velocities or measure total transport rates. They report saltation-induced, creep transport rates of 8×10^{-2} and 10×10^{-2} $gm^{-1}s^{-1}$ for 3 cm and 10 cm high ripples, respectively. Isenberg et al. (2011) also measured megaripple creep in the southern Negev Desert of Israel using the digital image process described above. At bedform crests the grain size distribution was bimodal with a coarse mode at 0.78 mm and a fine mode at 0.12 mm. They estimated creep flux using equation (2) and found $q_c = 6.23 \times 10^{-2}$ $gm^{-1}s^{-1}$. They evaluated the accuracy of the creep flux estimate using photogrammetric measurements of ripple height and migration rates, and suggested that the magnitude of error might be as large as 30%. They did not measure total transport, and thus could not estimate the relative proportion of creep.

Zhu et al. (2014) measured the sizes of Gobi sands in the Ejina desert basin, China. By assuming that coarse grains (≥0.5 mm) moved as creep they estimated that creep accounted for about 20% (their figure 9f) of transport. Qian et al. (2015) surveyed the grain sizes of oblique zibars in the Kumtagh Desert of Northwestern China, specifying that grains larger than 1.15 mm moved as creep. They estimated that creep transport accounted for 16.3% and 32.6% of total transport for linear dune and oblique zibar deposits, respectively. Liu et al. (2017) studied different sand environments in the Mu Us Desert, China and assumed that grains in the range of 0.5 – 2 mm would be creep. They found that the proportion of

creep on fixed, semi-fixed, semi-mobile, and mobile sand dunes was about 5%, 7.4%, 7.8%, and 10% of total flux, respectively.

We summarize results from the different field studies on creep transport in Figure 2.7. We normalize creep transport using total transport, q_c/q, and normalize u_* by u_{*t} to account for grain size differences between the studies. Regression analysis indicates no significant trend between q_c/q and u_*/u_{*t} for all field data ($R^2 = 0.018$, $P = 0.14$). However, there is a statistically negative relationship $q_c/q = -0.13 \times u_*/u_{*t} + 0.49$ ($R^2 = 0.40, P = 0.0028$) for field data based on results from vertical curve fitting. No significant trend exists for field data derived from buried traps ($R^2 = 0.070$, $P = 0.14$) data, although there is a negative relationship $q_c/q = -0.16 \times u_*/u_{*t} + 0.59$ ($R^2 = 0.46, P = 0.0020$) for data from buried traps when the data of Nickling (1978) are omitted. There is a statistically positive relationship $q_c/q = 0.028 \times u_*/u_{*t} - 0.0089$ ($R^2 = 0.14, P = 0.0013$) for the ripple migration data. The mean with standard deviation of all field studies of q_c/q and u_*/u_{*t} are 10.3% with standard deviation 11.8% and 1.74 with standard deviation 0.43, respectively.

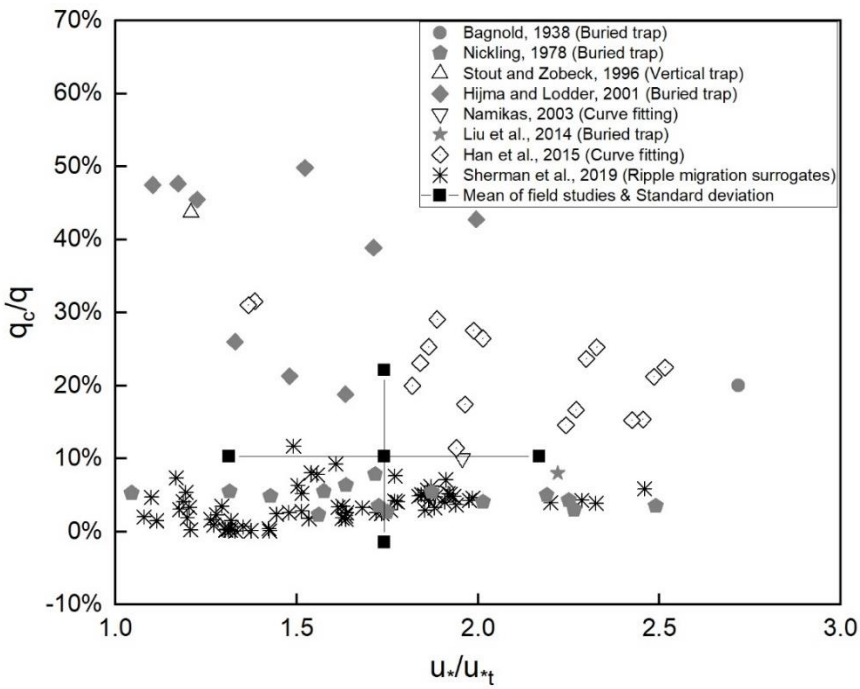

Figure 2. 7. Summary of field data for the distribution of $q_c/q \propto u_*/u_{*t}$. There is no statistically significant relationship according to the bulk field data. The cross bars indicate +/- one standard deviation of values around the mean.

Wind tunnel studies

The earliest creep-related sediment transport research in wind tunnels dates back to the experiments of Bagnold (1937). Bagnold measured creep with the slot traps described above. He presented very few details of his measurements, but reported that q_c/q was typically in the range of 25% (Bagnold, 1941, p.105). From the illustration of his trap (Bagnold, 1937, Figure 2), it is clear that it would also collect some unknown proportion of the saltation load. His results also suggest that the creep load of a mixed sand population would be coarser than the saltation load. Chepil (1945) used methods similar to those of Bagnold (1937) to measure the amount of surface creep for three types of soils and fine dune sand in the laboratory. His results indicated that creep accounted for about 7 - 25% of total transport for the soils and 15.7% for fine dune sand. The wind velocities in his experiments varied from 5.8 - 13.4 ms^{-1} at 0.3 m height.

Horikawa and Shen (1960) used wind tunnel experiments to study sand trap design, including the ability of some traps to capture creep. They used grain sizes between 0.125 and 0.5 mm with shear velocities of 0.3 - 0.97 ms^{-1}. Using the curve fitting method described above, they estimated that q_c/q was about 20% and that proportion is independent of the wind velocity.

He et al. (1990) measured creep of 0.18 mm and 0.23 mm sands driven by wind speeds (u) from 8.1 to 17.7 ms^{-1}. Although they reported creep transport associated with the range of wind speeds, they did not present a separate comparison of the creep load to total transport. From hydrodynamic analysis, they argued that a minor increase in fluid velocity would cause an exaggerated increase in the maximum grain size which can be carried. Under the assumption that $q \propto u^3$, they concluded that the increase of u would increase the proportion of larger grains in creep motion.

Dong et al. (2003) conducted wind tunnel studies using nine sand sizes with wind speeds that ranged from 8 to 22 ms^{-1}. Using data from their vertical trap array, they used the exponential fitting method to derive creep estimation and estimated that q_c/q ranged from 4% to 29%, with an average of 9%. Their data also indicate that the proportion of creep transport decreases with increased wind speed. The same methods were used by Dong et al. (2004) to test the influences of fetch length on the transport

of 0.18 mm sand over gravel surfaces. They found that q_c/q ranged from 1.7% to 18%, decreasing with increase in both wind speed and fetch length. With their longest (12 m) and shortest (0.5 m) experimental fetch lengths, they found the average proportions of creep to be 2.3% and 11.8%, respectively.

Ni et al. (2003) analyzed vertical flux profiles of sand flux and found that measured near-surface (about 0 – 2 cm) transport was significantly greater than that predicted by exponential curves. They argued that the "excess" flux near the surface was the contribution of creep. They did not compare the relative contribution of creep to total transport. By digitizing the vertical flux profiles depicted in their Figure 7, however, we can estimates values of q_c/q of about 8% and 19% for the grain sizes of 0.35 mm and 0.17 mm, respectively. Vertical trap arrays were also used by Wu et al. (2011a) to test the influences of trap height and compartment width on trap efficiency and measured creep transport. They evaluated a trap with five compartments and two heights (Figure 2.5 (b)), finding that the best of these combinations, based on the amount of sediment transport, was 5 cm high × 2 cm wide. They did not measure the ratio of creep transport to total transport rate.

Creep transport over a wet sand surface was studied by Han et al. (2012), using the methods of Dong et al. (2003) and testing with 0.2 mm sands, eight moisture contents (0.143, 0.231, 0.351, 0.587, 0.996, 1.448, 2.030, and 2.713%) and wind speeds of 10 - 20 ms^{-1}. The results indicated that q_c/q ranged between 12% and 33% (averaging 22%), and it decreased with increase in moisture content and wind velocity. An abrupt decrease in relative creep (from about 26% to 21%) occurred at moisture contents > 0.587% because of increasing capillary forces.

Particle tracking technology was used by Wang et al. (2009) to measure creep flux on a flat sand bed and to calculate the velocity and trajectory of creeping grains. They deployed eight grain size populations with shear velocities of 0.4 - 2.2 ms^{-1}. They estimated creep flux through the range of 10^{-7} - 10^{-2} $kgm^{-1}s^{-1}$, but did not report q_c/q and this value could not be derived from the data in their paper.

Cheng et al. (2013) measured creep transport rates (as described above) at four shear velocities (0.26, 0.35, 0.47, and 0.56 ms^{-1}) in wind tunnel experiments. Their main conclusion was $q_c \propto u_*^{2.8}$, a rate

slightly less than that normally attributed to the power function relationship $q \propto u_*^3$. As implied by these relationships, Cheng et al. (2013) found that the proportion of creep to total transport decreased through a range from 57 – 19% with increasing shear velocity.

Cheng et al. (2015a) studied the grain size characteristics of creeping particles. The data in their Table 2 indicate that more than 97% of creep involved grains larger than 0.25 mm. For the shear velocities that they used (0.55 ms^{-1} and 0.61 ms^{-1}) the mean grain size of creep was 1.14 times larger than that of the sand bed. In these experiments they found that $q_c \propto u_*^3$ and q_c/q increased with faster u_*. The results comparing q_c/q with u_*/u_{*t} contradict those of Cheng et al. (2013), likely because part of the flux caught by the traps used in this study would have included some unknown portion of saltation. They found that q_c/q averaged 2.4% for their test conditions (based on digitalized data from their Figure 5 and 9). In a following study, Cheng et al. (2015b) measured creep transport mass under different sand bed lengths. They found the effect of bed length on creep was dependent on grain size. Creep transport mass first increased with bed length (2.0 – 10.0 m) and then decreased when they used 0.15, 0.26, and 0.32 mm sands, but increased with bed length for 0.38 mm grains. No physical explanation was offered for these results. They did not measure the total amount of sand transport, thus the proportion of creep is unknown.

Wang et al. (2020) measured creep transport using 0.25 mm sand and the specialized trap described above (Figure 2.4 (c)). They found that q_c/q varied from 1 - 4% for shear velocity about 0.31 – 0.61 ms^{-1}. These data were used to validate their theoretical model that $q_c \propto u_*^5$.

We summarize results from the different wind tunnel studies in Figure 2.8, normalizing by q_c/q and u_*/u_{*t}. Regression analysis indicates no significant trend between q_c/q and u_*/u_{*t} for all wind tunnel data ($R^2 = 0.03$, $P = 0.088$). If the wind tunnel data are segregated, there are no statistically significant trends for the trap data alone ($R^2 = 0.38$, $P = 0.20$), or data obtained from curve fitting ($R^2 = 0.024$, $P = 0.15$). The mean with standard deviation of all wind tunnel studies of q_c/q and u_*/u_{*t} are 11.1% with standard deviation 9.3% and 2.24 with standard deviation 0.79, respectively.

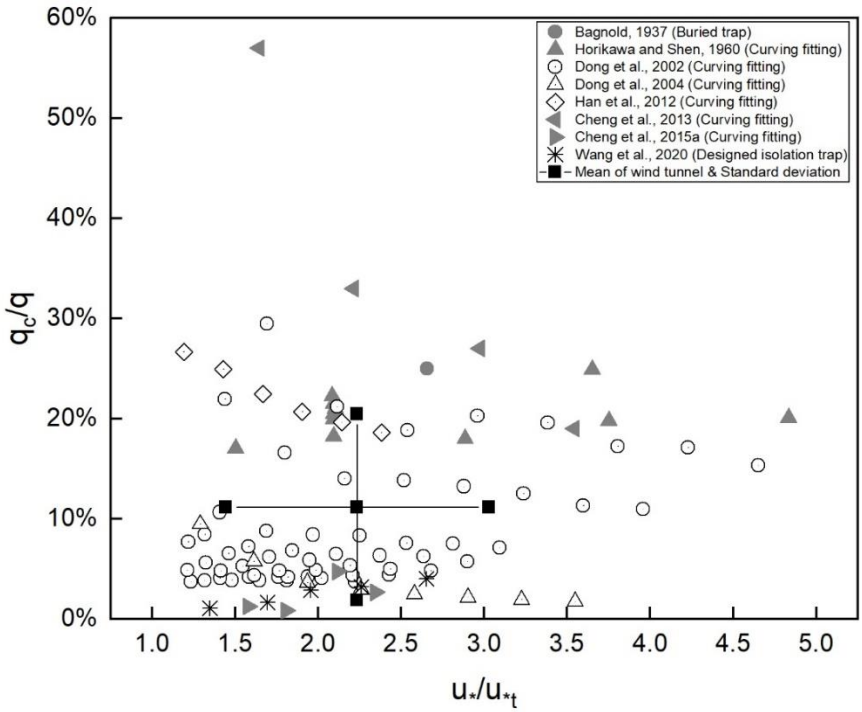

Figure 2. 8. Summary of wind tunnel data for the distribution of $q_c/q \propto u_*/u_{*t}$. There is no statistical significant relationship according to the bulk wind tunnel data. The cross bars indicate +/- one standard deviation of values around the mean.

Creep models

The dynamics of the aeolian creep process have been treated in a series of physical and empirical models as means to understand, replicate, or predict creep behavior and the contribution of creep to total sand transport. Many of these involve simulation of ripples as explicit or implicit surrogates for creep. Several studies, however, approach the issue of predicting creep from a theoretical perspective, including those of Kalinske (1943), Anderson (1987), Andreotti et al. (2002), Wang and Zheng (2004), Lämmel et al. (2012), and Wang et al. (2020). However, the development of empirical relationships, morphodynamic models, or abstracted (cellular automaton, or CA) simulations have been much more common.

Theoretical models

The earliest theoretical model we could find was that of Kalinske (1943) who used a mechanistic approach to derive his equation:

$$q_c = u_g \rho_s g \eta d \qquad (3)$$

where u_g is the speed of the creeping grains, g is the gravity constant, η is the number of grains in motion, and d is mean grain diameter. There are no explicit forcing parameters (e.g., wind speed or shear velocity) in equation (3), rather a counting of the number and size of grains passing a cross section per unit time. Kalinske does however, relate u_g to wind speed according to $u_g = f(\delta, \bar{u},\ u_t)$ where $\delta = \sqrt{(u - \bar{u})^2}$, $\bar{u}$ is mean wind speed, and u_t is the threshold wind speed for the initiation of grain motion. We are not aware of this model being tested empirically.

Anderson's (1987) work was a milestone in creep modeling. He argued that ripple evolution and morphology were governed by creep (reptation) transport rather than by saltation as originally posited by Bagnold (1936). Bagnold (1936) argued that ripple wavelength is controlled by characteristic saltation trajectory length. According to Anderson, the role of saltation is to provide the energy that initiates and maintains creep. The acceptance of the concept that creep is important to ripple morphodynamics changed, fundamentally, most subsequent approaches to ripple simulation. Four assumptions are in Anderson's creep model: (1) an infinitesimally perturbed surface, (2) creep energy supplied by salton impacts, (3) uniform grain size, (4) uniform salton impact angles. There is no explicit wind shear stress or velocity term. From these conditions, creep is predicted by:

$$q_c = m_p n_1 (N_{im})_0 \frac{2v_{ej}^2}{g} sin\gamma cos\gamma + m_p n_1 (N_{im})_0 cot\alpha \int_{x-a}^{x} \frac{\partial z}{\partial x} dx \qquad (4)$$

where m_p is particle mass, n_1 is the average number of creep particles, N_{im} is the uniform impact number (impact rate) of saltons per unit area per unit time which is a function a surface slope angle α, $(N_{im})_0$ is the impact rate for a flat surface, v_{ej} is the ejection velocity of reptating grains, γ is their ejection angle, and x is the horizontal distance. The roots of this model are similar to those of Kalinske (1943). Fluid forcing is linked to the model through the ejection velocity, assumed to be proportional to shear velocity. Anderson links the transport divergence that results from his model to ripple development using an Exner approach (described below). A linear stability analysis of the model predictions suggested that a fastest-growing wavelength, about six times the mean creep hop length, would emerge (Anderson, 1987). The increase in ripple wavelength conforms to the findings in the wind tunnel experiments of Seppälä and

Lindé (1978) and Walker (1981), supporting the validity of Anderson's approach. More detail concerning the interactions of sand surface grains with impacting saltons can be found in Crassous et al. (2007), and the processes are simulated in Sun et al. (2001).

Prigozhin (1999) developed a ripple/creep model with an approach similar to that developed by Anderson (1987). Prigozhin assumed that creeping particles will roll some distance before losing their momentum through collisions with other grains and the average distance traveled by a creeping grain depends on the surface slope. In the model, it is more difficult for creep to move up the stoss slope of a ripple and easier to move down the lee slope. With approximations:

$$q_c = 1 + k_\theta p_0 * \delta_x z + k_m p_0' * \delta_x z \quad (5)$$

where k_θ is approximated by cotθ and θ is the surface impact angle of saltons, p_0 is the density of the normal distribution, * is the operator of convolution, k_m is the mean stability of a grain on a horizontal surface (2.01 according to Prigozhin, 1999), and p_0' is the derivative of p_0. The model was able to produce realistic ripple morphology that evolved from irregularities on a perturbed bed to appropriate morphologies.

Andreotti et al. (2002) modeled creep (reptation) transport based on the work of Anderson (1987) and Anderson and Haff (1988; Anderson and Haff, 1991), especially the basic assumption that grains moving as creep were motivated by the impacts of saltons. From this they inferred that creep flux was simply proportional to the saltation flux and a function of the trajectory lengths of creeping grains compared to saltating grains:

$$q_c = \frac{l_c N_{ej}}{l_s} q_s \quad (6)$$

where l_c and l_s are the trajectory (hop) lengths of creep and saltation, respectively, N_{ej} is the total number of grains ejected (linearly increase with $u_*/\sqrt{gd}$), and q_s is the saltation transport rate. They also argued that l_c/l_s decreases with gd/u_*^2, indicating that q_c/q decreases with increasing shear velocity. They did not test their model against empirical studies, relying instead on characteristic and derived values for the variables.

Wang and Zheng (2004) modeled creep as a mode of transport distinct from reptation. They used two approaches to the problem, both rooted in theories of granular flow. First, following the work of Douady et al. (1999) they used the de Barré Saint-Venant (1850) model for depth-averaged flow and with a linear velocity profile within the grain flow with maximum speed at the surface. This approach results in the creep transport model:

$$q_c = Au_*^4 + B\rho_s d\bar{v}u_* \tag{7}$$

where A is defined below, B is a non-dimensional parameter, ρ_s is sediment density, d is mean grain diameter, and $\bar{v}$ is the average volume fraction (i.e., inverse of porosity).

$$A = \frac{\rho_a^2}{2\rho_s\bar{v}g\mu_m^2}\sqrt{\frac{\mu_m-\mu_d}{cdg}} \tag{8}$$

ρ_a is air density, ρ_s is sand grain density, g is gravity, ν is volume fraction, $c \approx 1.5$, μ_m is the coefficient of static friction, and μ_d is the coefficient of dynamic friction. In equation (7), the first term to the right of the equal sign represents the surface creep flux and the second term represents the depth-integrated, subsurface flux.

Their second model was based on the Navier-Stokes equations and built on the work of Rajagopal and Massoudi (1990):

$$q_c = \frac{2\rho_a C_0^2}{\rho_s g^2 C_1}\left[(1+\nu_0)ln\frac{(1+\nu_0)\nu_{max}}{(1+\nu_{max})\nu_0} - \frac{\nu_{max}-\nu_0}{\nu_{max}}\right] \times u_*^2 \tag{9}$$

where C_0 is a constant with value less than 0, C_1 is a constant with value greater than 0, v_0 is the fractional value at the surface and $\nu_{max} = \frac{\pi}{3\sqrt{2}}$ is the maximum fractional value (the attainment of which will cause motion to cease). Based on the experiments of Rajagopal et al. (2000), sample values for C_1 and C_0 were derived as 3.262 x 10^3 $kgm^{-1}s^{-1}$ and -3.232 x 10^3 Pa.

The Wang and Zheng (2004) models were tested against the wind tunnel data of Dong et al. (2003) by a comparison of observed and predicted q_c/q (recalling that Wang and Zheng (2004) use a restrictive definition of creep). For each of the four data sets tested both of the creep models over-predict q_c/q for shear velocities slower than about 0.6 – 0.8 ms^{-1}, and under-predict for shear velocities faster

than those. Wang and Zheng attribute the differences to issues with the methods of Dong et al. (2003), as the latter data would have included some reptation and saltation.

Lämmel et al. (2012) developed a continuum model by analyzing creep (reptation) and saltation motion and a turbulent wind field. Assuming reptating particles follow parabolic grain trajectories, saturated creep flux is predicted as:

$$q_c = 0.7 \times \rho_{b\prime}(1-\varphi)(\nu\psi)^{\frac{1}{3}} \quad (10)$$

where $\rho_{b\prime}$ is the mass density of sand grains per unit area, ν is kinematic viscosity ($1.5 \times 10^{-5} m^2 s^{-1}$), ψ is submerged specific weight ($\psi = \left(\frac{\rho_s - \rho_a}{\rho_a}\right) g$), $1-\beta$ is q_c/q and is obtained from:

$$\beta = \frac{\epsilon}{\epsilon + \eta(1 - v_s^c/u_g)} \quad (11)$$

where $\epsilon = 1 - d_0/d$, $d_0 = 4({}^{\nu^2}/_{\psi})^{1/3}$, η is a constant value (9 for sand trap data or 3.8 for particle tracking data), $v_s^c = 10u_{*t}$, $u_{*t} = 0.1\sqrt{\psi d}$, and u_g is salton velocity. According to the model, q_c/q increases with u_*/u_{*t}. For example, when $1 < u_*/u_{*t} < 2$, q_c/q is less than 30% of total sand flux. However, q_c/q increases to more than 44% when $u_*/u_{*t} \approx 4$ (their Figure 4). They reported that their creep model (equation 10), used with their saltation model performed well compared with the data sets of Iversen and Rasmussen (1999) and Creyssels et al. (2009).

Wang et al. (2020) examined creep as a granular flow phenomenon, developing a continuum theory based on 2-D Navier-Stokes momentum balance for incompressible flow, with the assumption that creep is driven by salton impacts on the surface layer. For equilibrium (steady state) creep:

$$q_c = \frac{4}{15}\frac{\tau_0^{5/2}}{\rho_s^{3/2} v g^2 \chi^{1/2} \mu_d^2 d} \quad (12)$$

where χ is a model parameter. They note that the Shields number $\theta = \tau_0/\rho_s g d$, making $q_c \sim \theta^{5/2}$. Because most models indicate that $q \sim \theta^{3/2}$, it follows that q_c/q must increase with shear velocity. This conclusion is supported by their wind tunnel experiments (described above), the wind tunnel data of Cheng et al. (2015b) and the field data of Sherman et al. (2019).

Figure 5 in Wang et al. (2020) shows good agreement between model results and wind tunnel data and a trend similar to that suggested by the field data.

Morphodynamic and Cellular Automaton models

There are two other common numerical methods used to simulate impact-driven creep. In some cases, the models are concerned with the development and migration of aeolian ripples. Some of these models are included in this review because ripple migration, as described above, is considered here to be an analog for creep motion. Most of the creep (in this case ripple migration) models are based on morphodynamic (continuum) concepts (Sauermann et al., 2001; Kroy et al., 2002; Giri and Shimizu, 2006; Duran et al., 2010; Parteli et al., 2014) or adopt cellular automaton (CA) approaches (Werner and Haff, 1988; Forrest and Haff, 1992; Nield and Baas, 2008; Pelletier, 2009; Eastwood et al., 2011; Rozier et al., 2019).

The morphodynamic model is established on the Exner equation (1920); Exner (1925) which relates the divergence of the sediment flux to local, temporal bed elevations and the continuum surface-morphology changes. This approach was developed for application to the evolution of river morphology. The original Exner (1920) equation used flow velocity as a proxy for sediment transport (because of ease of measurement). The model is now commonly formulated as:

$$\frac{\partial z}{\partial t} = -\frac{1}{\rho_b}\frac{\partial \mathrm{q}}{\partial \mathrm{x}} \tag{13}$$

where z is bed elevation relative to fixed datum, t is time, ρ_b is the bulk density of sand, and x is down flow distance. In aeolian studies, the Exner equation has been applied to models of wind fields over dunes, sand transport, avalanching on dunes, beginning with Exner's (1927) own studies. The different morphodynamic models concerning creep are developed to adjust specific conditions such as the surface micro-slopes (Manukyan and Prigozhin, 2009), creep behavior (Prigozhin, 1999; Yizhaq et al., 2004), or ripple growth (Yizhaq, 2004; Manukyan and Prigozhin, 2009). The morphodynamic approach is implicit or explicit in the model studies of Anderson (1987), Anderson (1990), Prigozhin (1999), Yizhaq et al.

(2004), Yizhaq (2008), Farimani et al. (2011), and Siminovich et al. (2019), but is most relevant here as it is applied to ripple development and migration, thus creep.

Similarly, cellular automaton models have been formulated to replicate the features of ripples according to grain-size sorting processes (Landry and Werner, 1994), creep paths, surface roughness, or shear stresses (Pelletier, 2009). Cellular automaton models were employed in some of the earliest attempts to simulate ripple (and dune) development and migration, usually with fidelity to either length or time scales, but not both (Werner, 1995; Nield and Baas, 2008; Pelletier, 2009; Eastwood et al., 2011). The CA method is used to produce discrete models that are formulated using time-dependent stochastic interaction rules between nearest neighbors of a lattice (Werner, 1995; Baas, 2007; Hyandye and Martz, 2017; Rozier et al., 2019). After combining one of the methods with a set of physical processes, e.g., fluid forcing, saltation trajectories, impacts with the bed surface, or interactions with the wind field, the saltation-induced creep (represented by ripple migration) can be simulated.

Discussion

In this paper, we reviewed the two types of creep and the main studies that measured, derived, or modeled creep transport and its contribution to total transport. As discussed in section 2, fluid creep and impact creep are the result of two dynamic mechanisms that motivate the creep load. Fluid creep dominates transport for conditions near the threshold of motion. Turbulent wind fluctuations dislodge grains from an immobile state to begin rolling or sliding along the surface when velocities exceed the threshold of motion. Although this phenomenon is observed in numerous laboratory studies (Bagnold, 1936; Chepil and Milne, 1939; Greeley and Marshall, 1985; Greeley and Iversen, 1987; Swann et al., 2020; Burr et al., 2020), there are several studies that argue that grains can be directly set into saltation without first moving as fluid creep along the surface (Bisal and Nielsen, 1962; Lyles and Krauss, 1971; Calder and Smith, 1990). The importance of fluid creep is a temporary phenomenon and diminishes with the increase of wind speed. The impact from saltating particles quickly becomes the major energy source to drive impact creep along the surface.

The principle studies that quantify creep transport are summarized in Table 2.1 (all data are accessible online via the Zenodo data repository (Zhang et al., 2021). In order to compare different experimental results, we plotted data from those studies with the normalized variables q_c/q and u_*/u_{*t} in Figure 2.7 and Figure 2.8. Regression analysis indicates no statistically significant trend between q_c/q and u_*/u_{*t} for field ($P = 0.14$) and wind tunnel studies ($P = 0.088$). If Bagnold's (1937) contention that creep comprises about 25% of total transport is valid, then we expect that there would be no relationship between q_c/q and u_*/u_{*t}. Most of the individual studies that we reviewed and the creep models, however, did indicate that there is a relationship, although the nature of that relationship remains uncertain.

The averages of q_c/q for field and wind tunnel studies are 10.3% and 11.1%, respectively. The standard deviations of q_c/q are 11.8% and 9.3% for field and wind tunnel experiments, respectively. These data are also indicated in Figure 2.7 and Figure 2.8 by plotting the means and including bars to represent +/- one standard deviation for each variable. A two tail t-test suggests that u_*/u_{*t} found in the field studies are significantly ($P < 0.001$) different from those in wind tunnel studies while no significant ($P = 0.56$) difference for q_c/q in field and wind tunnel studies. These findings suggest that there are not significant scaling differences between the wind tunnel and field data for relative transport rates, but such scaling issues do arise for the transport forcing represented by u_*/u_{*t}.

In considering the differences between the wind tunnel and field results and the scatter within each, there are several potential sources of error that might be in play. One involves the different methods used to measure and quantify creep transport, as described in sections 2 and 3. The methods include using buried sand traps or vertical traps arrays with small openings at the surface, curve fitting to vertical or horizontal saltation flux profiles, ripple migration surrogates, particle-tracking velocimetry, and sedimentological approaches. First, the buried traps, even with narrow openings flush with the surface will capture some unknown portion of saltation, as will the surface vertical traps. Other versions of slot traps may capture substantial saltation with the creep sample. The approach used by Cheng et al. (2013)

likely produced the most reliable results, based on the assumption that the amount of collected creep should not change with different opening widths. The assumption needs independent validation, although we believe that it is sound. Cheng et al. (2015b, p. 1415) conclude "…*that the direct measurement of creep using a* (single) *bed trap is not possible*."

The second method is that suggested by Dong et al. (2003), related to that developed by Horikawa and Shen (1960), that estimated creep flux by extrapolating vertical flux profiles, derived from trap data, to the bed. The calculated results by this method include some unknown portion of saltation. This is a mathematically appealing concept, but unverified empirically or theoretically. The data for this method are sensitive to potential scouring or other disturbances at the base of vertical trap arrays that might decrease the quantities of sand captured. Further, in the curve fitting exercise, the representation of trap elevations with arithmetic centers instead of geometric centers would systematically increase the magnitude of the estimates of creep flux (Ellis et al., 2009).

The third method is to treat ripple migration flux as a surrogate for creep transport based on equation (2). There are three assumptions with this method: (1) the ripple migration rate is the same as the creep transport rate; (2) the morphology of the volume of the ripples is adequately represented by $H/2$; and (3) the porosity of ripples is uniform and constant, e.g. 0.4 for p in equation (2). Our view is that this is a reasonable proposition, but that $q_r \approx q_c$ because although most creep movement is represented by the ripple movement, some proportion of creeping grains may move faster or slower than the bedforms propagate.

The fourth method is the particle tracking velocimetry approach developed by Wang et al. (2009). There are two main constraints with this method: (1) this method depends upon illuminating the bed, the reflection of concentrated scattered light, and the presence of ripples, for example, will significantly disturb the grain tracking process; (2) the method is only viable if creep involves flow only a few grains deep (e.g., 1 mm depth as in Wang et al., 2009), and it assumes that the net creep velocity is the same as that of the surface grains. Zhang et al. (2010) and Cheng et al. (2013) criticized that this method would

underestimate creep flux under high sediment transport rate; contrarily, the creep transport might be overestimated by using faster surface grains as representing a deeper sediment transport flux.

The last method is based on the application of sedimentological approaches. These are based on the simple assumption that relatively large grains are only transported as creep. This method, however, depends on the local wind shear stress being insufficient to move the larger grains, i.e., large grains are moved only by impacts from smaller saltating particles.

The data presented in Figures 2.7 and 2.8 are assumed to represent equilibrium transport conditions for both creep and saltation. The data of Dong et al. (2004) and Cheng et al. (2015b) show a fetch length control on creep transport rates that is largely unaccounted for in the other studies we have reviewed, although the ripple migration data of Sherman et al. (2019) were collected in long fetch length conditions. There are no comparable studies concerning potential saturation length effects on q_c/q.

The sophistication of models to predict creep transport has substantially exceeded the empiricism necessary to support those models, often including variables about which our knowledge is scant. Beyond that, there are two main issues that have challenged the development and acceptance of creep models. First is what seems to be the complex, nonlinear relationships between creep, saltation, and the wind field, characteristic of issues with all modes of transport. Second is the disagreement concerning the behavior of the creep system. Indeed, there persists disagreement concerning the definition of creep or a process-related distinction between creep, reptation, and saltation. Further, different models predict contradictory relationships between creep and shear velocity. For example, the model of Wang and Zheng (2004) indicates that q_c/q decreases with u_*, while the results of Lämmel et al. (2012) and Wang et al. (2020) indicate that q_c/q increases with u_*. In this sense, the models reflect the contradictory empirical findings.

Table 2. 1. Summary of conditions associated with the creep studies described above. Type refers to field (F) or wind tunnel (WT) studies. In many studies the threshold condition is predicted based on grain size (indicated with †). NA indicates no data available.

Study	Type	u_*, u (ms^{-1})	d (mm)	u_{*t}, u_t (ms^{-1})	q_c/q (%)
Bagnold (1938)	F	0.43 - 0.82	~ 0.28	0.23	20
Nickling (1978)	F	0.26 - 0.62	~ 0.062	0.25	2.29-7.87
Stout and Zobeck (1996)	F	9.06 at 10 m (u)	0.25	7-8 at 10 m (u_t)	43.7
Hijma and Lodder (2001)	F	0.24 - 0.65	0.23	0.22†	31-53
Namikas (2003)	F	0.27 - 0.63	0.25	0.23†	10
Yang et al. (2011)	F	NA	0.063 - 0.125	NA	2-30
Liu et al. (2014)	F	5.2 - 13 at 2 m (u)	0.1 - 0.152	4.1 at 2 m (u_t)	5-11
Gillies et al. (2012)	F	NA	1	NA	0.20
Han et al. (2015)	F	0.22 - 0.4	0.19 (ρ_s=1958 kg/m$^{3)}$	0.159-0.165	10-32.5
Sherman et al. (2019)	F	0.3-0.59	0.27-0.47	0.24-0.32	0.09-11.69
Jerolmack et al. (2006)	F	NA	0.1 - 1 and 1 - 3	NA	1
Zimbelman et al. (2009)	F	9 at 1 m (u)	1.5	NA	NA
Isenberg et al. (2011)	F	NA	0.16-0.87	NA	NA
Zhu et al. (2014)	F	NA	NA	NA	20
Qian et al. (2015)	F	NA	NA	NA	16.3-32.6
Liu et al. (2017)	F	NA	NA	NA	5-10
Bagnold (1937)	WT	0.4 - 0.62	0.25	0.192	25
Chepil (1945)	WT	5.8 - 13.4 at 0.3 m (u)	0.15-0.42	NA	7.4-24.9
Horikawa and Shen (1960)	WT	0.3 - 0.91	0.2	0.21†	20
He et al. (1990)	WT	8.1 - 17.7 (u)	0.18 and 0.23	NA	NA
Dong et al. (2002)	WT	8 - 22 (u)	0.10 - 1.00	0.35-0.51	4-29
Dong et al. (2004)	WT	8-22 (u)	0.18	6.2 (u_t)	1.7-9.5
Ni et al. (2002)	WT	0.47 - 2.36	0.17 and 0.35	NA	19 and 8
Wu et al. (2011)	WT	8.4 - 14.6 (u)	0.26	7.59 (u_t)	NA
Han et al. (2012)	WT	10 - 20 (u)	0.2	8.4 (u_t)	12-33
Wang et al. (2009)	WT	0.4 - 2.2	NA	NA	NA
Cheng et al. (2013)	WT	0.26 - 0.56	0.12	0.158	19-57
Cheng et al. (2015a)	WT	0.41 - 0.61	0.32	0.26†	0.8-4.7
Cheng et al. (2015b)	WT	0.23 – 0.61	0.15-0.38	0.18-0.29	NA
Wang et al. (2020)	WT	0.31 - 0.61	0.25	0.23†	1 -4

One of the main consequences of particles moving as creep is resulting entrainment of other grains into higher energy motion, e.g. saltation, which is manifest through the reduction of the threshold

shear velocity as demonstrated by the early studies by Bagnold (1936) and many others. As sand flux increases, particles moved as fluid and impact creep will trigger other particles for additional saltation. From this process, it is generally agreed that creep plays an important role in maintaining equilibrium sand transport (e.g., Owen, 1964; Anderson et al., 1991; Andreotti et al., 2002; Pahtz et al., 2020).

There remains no consensus on the relative contribution of creep to total transport. It has been commonly assumed that Bagnold's (1937 and 1938) estimates that $q_c/q \approx 0.25$ is reasonable. The review of field and wind tunnel studies, however, indicates that there is a much wider range for this ratio as indicated with the summary in Table 2.1 and the data plotted in Figures 2.7 and 2.8. There is a range of from less than 1% to more than 50%. From the combined studies, those studies, the mean and standard deviation of q_c/q are 10.7% and 10.7%. The frequency distributions of estimates for q_c/q from the wind tunnel and field studies are depicted in Figure 2.9, indicating that creep more commonly represents about 10% of total transport.

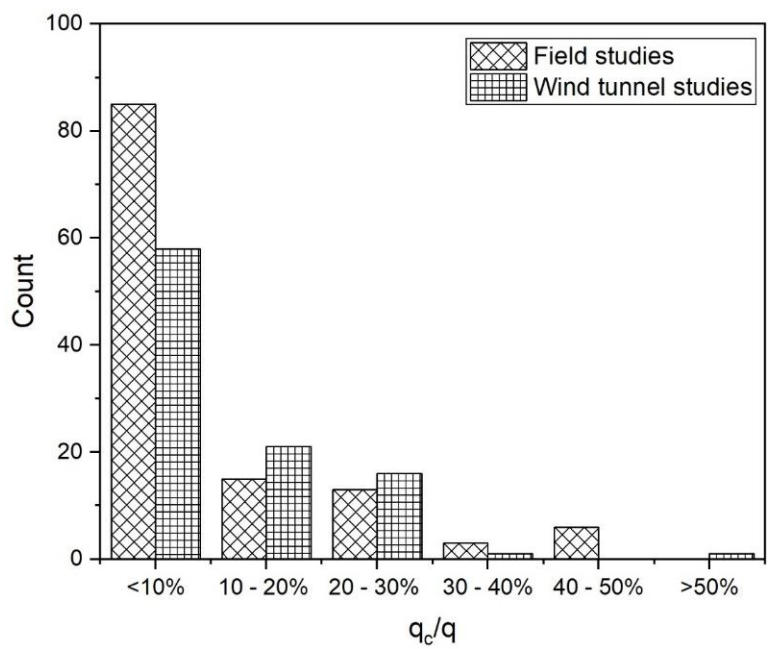

Figure 2. 9. The frequency distribution of values of q_c/q found in the field and wind tunnel studies.

The processes associated with saltation and suspension have been studied extensively, and our understanding of these modes of transport is well advanced. By comparison, it is apparent that we know relatively little about the behavior of creep. As noted above, the results of experiments and the predictions

of models produce contradictory relationships between q_c/q and u_*/u_{*t}. This indicates flaws in empiricism that need resolution. One issue may be that of trap efficiencies in both field and laboratory environments. In cases where traps catch more or less sand than is carried by the wind, due to basal scour or aerodynamic effects, for example, the resulting distortion of relationships may mask the nature or presence of a functional dependence. There are also important implications for some field studies of total transport that rely on sets of sand traps that do not extend to the surface. Studies using BSNE 8 traps, for example have arrays where the lowest trap is installed 0.05 to 0.1 m above the surface. Total flux is estimated by curve fitting, a process that has been indicated to not account for creep flux as indicated by the approach of Dong et al. (2003). Estimates derived using such methods will under-represent total transport by amounts of 1% (trivial) to as much as 50%, according to the findings summarized in Figure 2.9. A resolution of this disparity is worthy of further study.

Creep processes involving movement of large grains over surfaces of much finer materials or over lag surfaces deserve greater attention. This paper has focused on creep transport in environments with graded sands. In other environments, where the relationships between fluid and impact creep or creep transport relative to total transport the findings of the papers reviewed herein may not be applicable.

Conclusions

There are three main conclusions that we can draw from this review of studies focused on creep transport. First, according to most studies, the development of fluid creep is critical to the subsequent development of saltation and thus total sand transport. Second, the proportion of creep transport relative to total flux is not constant at about 25% as initially suggested by Bagnold (1937 and 1938). After normalizing creep transport with wind speed and grain size, q_c/q shows a wide range of variation from about 1% to more than 50%. This degree of variability, apparently unexplained from one study to another, has important implications for understanding aeolian sand transport. Third, the disagreement about whether there is a direct or inverse relationship between q_c/q and u_*/u_{*t} suggests a fundamental deficit in our understanding of the sand transport system. Our assumption that the individual studies have

correctly interpreted the results of experiments points to the conclusion that the disparate findings point to methodological or definitional differences that require resolution.

Since Bagnold's experiments (1936) to quantitatively relate sand transport to wind speed, great advances have been made in understanding the mechanisms responsible. Consensus on how to define and measure creep transport alone, however, remains elusive. We know relatively little about the characteristics of creep movements, especially the trajectories and speeds of grains bouncing close to the bed. We cannot recognize a robust relationship between rates of creep and total transport as a response to wind forcing, and the field and wind tunnel data remain contradictory. With agreement and protocols to mitigate these hurdles, and careful experimental design, we can look to improved empiricism to elucidate the nature of, controls on, and importance of, aeolian creep.

Reference List for Chapter 2

Anderson, R.S., 1987. A Theoretical-Model for Aeolian Impact Ripples. Sedimentology 34, 943-956.

Anderson, R.S., 1989. Saltation of Sand - a Qualitative Review with Biological Analogy. P Roy Soc Edinb B 96, 149-165.

Anderson, R.S., 1990. Eolian Ripples as Examples of Self-Organization in Geomorphological Systems. Earth-Science Reviews 29, 77-96.

Anderson, R.S., Haff, P., 1991. Wind modification and bed response during saltation of sand in air, Aeolian Grain Transport 1. Springer, pp. 21-51.

Anderson, R.S., Haff, P.K., 1988. Simulation of Eolian Saltation. Science 241, 820-823.

Anderson, R.S., Hallet, B., 1986. Sediment Transport by Wind - toward a General-Model. Geological Society of America Bulletin 97, 523-535.

Anderson, R.S., Sørensen, M., Willetts, B.B., 1991. A review of recent progress in our understanding of aeolian sediment transport. Aeolian Grain Transport 1, 1-19.

Andreotti, B., 2004. A two-species model of aeolian sand transport. J Fluid Mech 510, 47-70.

Andreotti, B., Claudin, P., Douady, S., 2002. Selection of dune shapes and velocities - Part 1: Dynamics of sand, wind and barchans. Eur Phys J B 28, 321-339.

Andreotti, B., Claudin, P., Pouliquen, O., 2006. Aeolian sand ripples: Experimental study of fully developed states. Phys Rev Lett 96.

Ashrafi, K., Kalhor, M., Shafie-Pour, M., Esfahanian, V., 2015. Numerical simulation of aerodynamic suspension of particles during wind erosion. Environ Earth Sci 74, 1569-1578.

Baas, A.C., 2019. Grains in motion, Aeolian Geomorphology: A New Introduction. John Wiley & Sons, Ltd Chichester, UK, pp. 27-60.

Baas, A.C.W., 2004. Evaluation of saltation flux impact responders (Safires) for measuring instantaneous aeolian sand transport intensity. Geomorphology 59, 99-118.

Baas, A.C.W., 2007. Complex systems in aeolian geomorphology. Geomorphology 91, 311-331.

Bagnold, R.A., 1936. The movement of desert sand. Proceedings of the Royal Society of London. Series A-Mathematical and Physical Sciences 157, 594-620.

Bagnold, R.A., 1937. The transport of sand by wind. The Geographical Journal 89, 409-438.

Bagnold, R.A., 1938. The measurement of sand storms. Proceedings of the Royal Society of London. Series A. Mathematical and Physical Sciences 167, 282-291.

Bagnold, R.A., 1941. The Physics of Blown Sands and Desert Dunes, London: Methuen.

Bagnold, R.A., 1973. The nature of saltation and of 'bed-load'transport in water. Proceedings of the Royal Society of London. A. Mathematical and Physical Sciences 332, 473-504.

Baker, M.M., Newman, C.E., Lapotre, M.G.A., Sullivan, R., Bridges, N.T., Lewis, K.W., 2018. Coarse Sediment Transport in the Modern Martian Environment. J Geophys Res-Planet 123, 1380-1394.

Barchyn, T.E., Martin, R.L., Kok, J.F., Hugenholtz, C.H., 2014. Fundamental mismatches between measurements and models in aeolian sediment transport prediction: The role of small-scale variability. Aeolian Research 15, 245-251.

Belly, P.-Y., 1962. Sand movement by wind. California University Berkeley Institution Of Engineering Research.

Bisal, F., Nielsen, K., 1962. Movement of soil particles in saltation. Canadian Journal of Soil Science 42, 81-86.

Bolles, K., Forman, S.L., Sweeney, M., 2017. Eolian processes and heterogeneous dust emissivity during the 1930s Dust Bowl Drought and implications for projected 21st-century megadroughts. The Holocene 27, 1578-1588.

Borsy, Z., 1973. A Homokfodrok. Foldrajzi Ertesuto, 109-115.

Boulton, J.W., 1997. Quantifying the morphology of aeolian impact ripples formed in a natural dune setting.

Brunsden, D., Thornes, J., 1979. Landscape sensitivity and change. Transactions of the Institute of British Geographers, 463-484.

Burr, D.M., Sutton, S.L.F., Emery, J.P., Nield, E.V., Kok, J.F., Smith, J.K., Bridges, N.T., 2020. A wind tunnel study of the effect of intermediate density ratio on saltation threshold. Aeolian Research 45.

Butterfield, G., 1991. Grain transport rates in steady and unsteady turbulent airflows, Aeolian Grain Transport 1. Springer, pp. 97-122.

Calder, S., Smith, J., 1990. Mechanics of bedload transport by wind. Geological Society of America Bulletin.

Carneiro, M.V., Rasmussen, K.R., Herrmann, H.J., 2015. Bursts in discontinuous Aeolian saltation. Scientific Reports 5, 1-8.

Cheng, H., He, J.J., Zou, X.Y., Li, J.F., Liu, C.C., Liu, B., Zhang, C.L., Wu, Y.Q., Kang, L.Q., 2015a. Characteristics of particle size for creeping and saltating sand grains in aeolian transport. Sedimentology 62, 1497-1511.

Cheng, H., Liu, C.C., Li, J.F., Liu, B., Zheng, Z.Q., Zou, X.Y., Kang, L.Q., Fang, Y., 2018. Experimental study of aeolian sand ripples in a wind tunnel. Earth Surface Processes and Landforms 43, 312-321.

Cheng, H., Liu, C.C., Zou, X.Y., Li, J.F., He, J.J., Liu, B., Wu, Y.Q., Kang, L.Q., Fang, Y., 2015b. Aeolian creeping mass of different grain sizes over sand beds of varying length. J Geophys Res-Earth 120, 1404-1417.

Cheng, H., Zou, X.Y., Liu, C.C., He, J.J., Wu, Y.Q., 2013. Transport mass of creeping sand grains and their movement velocities. J Geophys Res-Atmos 118, 6374-6382.

Chepil, W., 1945. Dynamics of wind erosion: I. Nature of movement of soil by wind. Soil Science 60, 305-320.

Chepil, W., 1961. The use of spheres to measure lift and drag on wind-eroded soil grains. Soil Science Society of America Journal 25, 343-345.

Chepil, W., Milne, R., 1941. Wind erosion of soil in relation to roughness of surface. Soil Science 52, 417-434.

Chepil, W.S., Milne, R., 1939. Comparative study of soil drifting in the field and in a wind tunnel. Scientific Agriculture 19, 249-257.

Cornish, V., 1914. Waves of sand and snow and the eddies which make them. TF Unwin.

Crassous, J., Beladjine, D., Valance, A., 2007. Impact of a projectile on a granular medium described by a collision model. Phys Rev Lett 99, 248001.

Creyssels, M., Dupont, P., El Moctar, A.O., Valance, A., Cantat, I., Jenkins, J.T., Pasini, J.M., Rasmussen, K.R., 2009. Saltating particles in a turbulent boundary layer: experiment and theory. J Fluid Mech 625, 47-74.

Daliang, H., Jianyou, S., Dayou, L., 1990. Three forms of movement of blowing sand and their measurement. Journal of Desert Research 10, 9.

de Barré Saint-Venant, A., 1850. Mémoire sur des formules nouvelles pour la solution des problemes relatifs aux eaux courantes. CR Acad. Sci. Paris 31, 283.

Douady, S., Andreotti, B., Daerr, A., 1999. On granular surface flow equations. Eur Phys J B 11, 131-142.

Duniway, M.C., Pfennigwerth, A.A., Fick, S.E., Nauman, T.W., Belnap, J., Barger, N.N., 2019. Wind erosion and dust from US drylands: a review of causes, consequences, and solutions in a changing world. Ecosphere 10, e02650.

Duran, O., Claudin, P., Andreotti, B., 2011. On aeolian transport: Grain-scale interactions, dynamical mechanisms and scaling laws. Aeolian Research 3, 243-270.

Duran, O., Parteli, E.J.R., Herrmann, H.J., 2010. A continuous model for sand dunes: Review, new developments and application to barchan dunes and barchan dune fields. Earth Surface Processes and Landforms 35, 1591-1600.

Eastwood, E., Nield, J., Baas, A., Kocurek, G., 2011. Modelling controls on aeolian dune-field pattern evolution. Sedimentology 58, 1391-1406.

Einstein, H.A., 1950. The bed-load function for sediment transportation in open channel flows. US Government Printing Office.

Ellis, J.T., Li, B., Farrell, E.J., Sherman, D.J., 2009. Protocols, for characterizing aeolian mass-flux profiles. Aeolian Research 1, 19-26.

Exner, F., 1920. Zur physik der dunen, Akad. Wiss. Wien Math. Naturwiss. Klasse 129, 929-952.

Exner, F.M., 1925. Uber die wechselwirkung zwischen wasser und geschiebe in flussen. Akad. Wiss. Wien Math. Naturwiss. Klasse 134, 165-204.

Exner, F.M., 1927. Über Dünen und Sandwellen. Geografiska Annaler 9, 81-99.

Farimani, A.B., Ferreira, A.D., Sousa, A.C.M., 2011. Computational modeling of the wind erosion on a sinusoidal pile using a moving boundary method. Geomorphology 130, 299-311.

Feng, G., Sharratt, B., 2007. Validation of WEPS for soil and PM10 loss from agricultural fields within the Columbia Plateau of the United States. Earth Surface Processes and Landforms 32, 743-753.

Flagg, C.B., Neff, J.C., Reynolds, R.L., Belnap, J., 2014. Spatial and temporal patterns of dust emissions (2004–2012) in semi-arid landscapes, southeastern Utah, USA. Aeolian Research 15, 31-43.

Foroutan, M., Zimbelman, J.R., 2016. Mega-ripples in Iran: A new analog for transverse aeolian ridges on Mars. Icarus 274, 99-105.

Foroutan, M., Zimbelman, J.R., 2020. Evaluation of large data sets for Transverse Aeolian Ridges (TARs) on Earth and Mars. Planetary and Space Science, 104966.

Forrest, S.B., Haff, P.K., 1992. Mechanics of Wind Ripple Stratigraphy. Science 255, 1240-1243.

Gilbert, G.K., Murphy, E.C., 1914. The transportation of debris by running water. US Government Printing Office.

Gillies, J.A., Etyemezian, V., Nikolich, G., Nickling, W.G., Kok, J.F., 2018. Changes in the saltation flux following a step-change in macro-roughness. Earth Surface Processes and Landforms 43, 1871-1884.

Gillies, J.A., Nickling, W.G., Tilson, M., Furtak-Cole, E., 2012. Wind-formed gravel bed forms, Wright Valley, Antarctica. J Geophys Res-Earth 117.

Giri, S., Shimizu, Y., 2006. Numerical computation of sand dune migration with free surface flow. Water Resour Res 42.

Goossens, D., Buck, B., 2011. Gross erosion, net erosion and gross deposition of dust by wind: field data from 17 desert surfaces. Earth Surface Processes and Landforms 36, 610-623.

Gordon, M., Neuman, C.M., 2011. A study of particle splash on developing ripple forms for two bed materials. Geomorphology 129, 79-91.

Greeley, R., Iversen, J.D., 1987. Wind as a geological process: on Earth, Mars, Venus and Titan. CUP Archive.

Greeley, R., Marshall, J.R., 1985. Transport of Venusian Rolling Stones by Wind. Nature 313, 771-773.

Haff, P.K., Anderson, R.S., 1993. Grain Scale Simulations of Loose Sedimentary Beds - the Example of Grain-Bed Impacts in Aeolian Saltation. Sedimentology 40, 175-198.

Halfen, A.F., Lancaster, N., Wolfe, S., 2016. Interpretations and common challenges of aeolian records from North American dune fields. Quaternary International 410, 75-95.

Han, Q.J., Qu, J.J., Liao, K.T., Zhang, K.C., Zu, R.P., Niu, Q.H., 2012. A wind tunnel study of the parameters for aeolian sand transport above a wetted sand surface using sands from a tropical humid coastal region of southern China. Environ Earth Sci 67, 243-250.

Hardisty, J., Whitehouse, R.J.S., 1988. Evidence for a New Sand Transport Process from Experiments on Saharan Dunes. Nature 332, 532-534.

Hedding, D.W., Nel, W., Anderson, R.L., 2015. Aeolian processes and landforms in the sub-Antarctic: preliminary observations from Marion Island. Polar Res 34.

Hijma, M., Lodder, Q.J., 2001. An evaluation of aeolian sand transport models using four different sand traps at the Hors, Texel.

Ho, T.D., Dupont, P., El Moctar, A.O., Valance, A., 2012. Particle velocity distribution in saltation transport. Phys Rev E 85.

Ho, T.D., Valance, A., Dupont, P., El Moctar, A.O., 2014. Aeolian sand transport: Length and height distributions of saltation trajectories. Aeolian Research 12, 65-74.

Horikawa, K., Shen, H.W., 1960. Sand movement by wind action:(on the characteristics of sand traps).

Howard, A.D., 1977. Effect of slope on the threshold of motion and its application to orientation of wind ripples. Geological Society of America Bulletin 88, 853-856.

Hoyle, R.B., Woods, A.W., 1997. Analytical model of propagating sand ripples. Phys Rev E 56, 6861-6868.

Huo, W., He, Q., Yang, F., Yang, X., Yang, Q., Zhang, F., Mamtimin, A., Liu, X., Wang, M., Zhao, Y., 2017. Observed particle sizes and fluxes of Aeolian sediment in the near surface layer during sand-dust storms in the Taklamakan Desert. Theoretical and Applied Climatology 130, 735-746.

Hyandye, C., Martz, L.W., 2017. A Markovian and cellular automata land-use change predictive model of the Usangu Catchment. Int J Remote Sens 38, 64-81.

Isenberg, O., Yizhaq, H., Tsoar, H., Wenkart, R., Karnieli, A., Kok, J.F., Katra, I., 2011. Megaripple flattening due to strong winds. Geomorphology 131, 69-84.

Iversen, J.D., Rasmussen, K.R., 1999. The effect of wind speed and bed slope on sand transport. Sedimentology 46, 723-731.

Jerolmack, D.J., Mohrig, D., Grotzinger, J.P., Fike, D.A., Watters, W.A., 2006. Spatial grain size sorting in eolian ripples and estimation of wind conditions on planetary surfaces: Application to Meridiani Planum, Mars. J Geophys Res-Planet 111.

Kalinske, A.A., 1943. Turbulence and the transport of sand and silt by wind. Annals of the New York Academy of Sciences 44, 41-54.

Kawamura, R., 1951. Study on sand movement by wind. Rept. Inst. Sci. Technol. 5, 95-112.

Kerber, L., Head, J.W., 2012. A progression of induration in Medusae Fossae Formation transverse aeolian ridges: evidence for ancient aeolian bedforms and extensive reworking. Earth Surface Processes and Landforms 37, 422-433.

Kjelgaard, J.F., Chandler, D.G., Saxton, K.E., 2004. Evidence for direct suspension of loessial soils on the Columbia Plateau. Earth Surface Processes and Landforms 29, 221-236.

Kok, J.F., Parteli, E.J.R., Michaels, T.I., Karam, D.B., 2012. The physics of wind-blown sand and dust. Rep Prog Phys 75.

Kok, J.F., Renno, N.O., 2009. A comprehensive numerical model of steady state saltation (COMSALT). J Geophys Res-Atmos 114.

Kroy, K., Sauermann, G., Herrmann, H.J., 2002. Minimal model for aeolian sand dunes. Phys Rev E 66.

Lammel, M., Dzikowski, K., Kroy, K., Oger, L., Valance, A., 2017. Grain-scale modeling and splash parametrization for aeolian sand transport. Phys Rev E 95.

Lammel, M., Meiwald, A., Yizhaq, H., Tsoar, H., Katra, I., Kroy, K., 2018. Aeolian sand sorting and megaripple formation. Nat Phys 14, 759-+.

Lammel, M., Rings, D., Kroy, K., 2012. A two-species continuum model for aeolian sand transport. New J Phys 14.

Landry, W., Werner, B., 1994. Computer simulations of self-organized wind ripple patterns. Physica D: Nonlinear Phenomena 77, 238-260.

Lapotre, M., Ewing, R., Lamb, M., Fischer, W., Grotzinger, J., Rubin, D., Lewis, K., Ballard, M., Day, M., Gupta, S., 2016. Large wind ripples on Mars: A record of atmospheric evolution. Science 353, 55-58.

Li, B.L., Neuman, C.M., 2012. Boundary-layer turbulence characteristics during aeolian saltation. Geophys Res Lett 39.

Li, L., Martz, L.W., 1995. Aerodynamic dislodgement of multiple-size sand grains over time. Sedimentology 42, 683-694.

Li, Y.T., Guo, Y., 2008. Numerical simulation of aeolian dusty sand transport in a marginal desert region at the early entrainment stage. Geomorphology 100, 335-344.

Ling, Y.Q., Qu, J.J., Li, C.Z., 2003. Study on sand ripple movement with close shoot method. Journal of Desert Research 23, 118 (in Chinese with English abstract).

Liu, F., Hao, Y., Xin, Z., Chen, H., Xu, J., Zhao, Y., 2014. The surface aeolian-sand flow structure in the northeastern margin of the Ulanbuh desert. J. Desert Research. 34 (5), 1200–1207 (in Chinese with English abstract).

Liu, B., Jin, H.L., Sun, L.Y., Sun, Z., Zhang, C.X., 2017. Grain size and geochemical study of the surface deposits of the sand dunes in the Mu Us desert, northern China. Geol J 52, 1009-1019.

Liu, L., Bo, T.L., 2019. A study on the initiation of saltation in the model of wind-blown sand transport considering the effect of turbulence. Granul Matter 21.

Lorenz, R.D., 2011. Observations of wind ripple migration on an Egyptian seif dune using an inexpensive digital timelapse camera. Aeolian Research 3, 229-234.

Lorenz, R.D., Valdez, A., 2011. Variable wind ripple migration at Great Sand Dunes National Park and Preserve, observed by timelapse imaging. Geomorphology 133, 1-10.

Lyles, L., Krauss, R.K., 1971. Threshold Velocities and Initial Particle Motion as Influenced by Air Turbulence. T Asae 14, 563-&.

Mahowald, N.M., Kloster, S., Engelstaedter, S., Moore, J.K., Mukhopadhyay, S., McConnell, J.R., Albani, S., Doney, S.C., Bhattacharya, A., Curran, M., 2010. Observed 20th century desert dust variability: impact on climate and biogeochemistry. Atmospheric Chemistry and Physics 10, 10875-10893.

Manukyan, E., Prigozhin, L., 2009. Formation of aeolian ripples and sand sorting. Phys Rev E 79.

Martin, R.L., Kok, J.F., 2017. Wind-invariant saltation heights imply linear scaling of aeolian saltation flux with shear stress. Sci Adv 3.

Martin, R.L., Kok, J.F., 2018. Distinct Thresholds for the Initiation and Cessation of Aeolian Saltation From Field Measurements. J Geophys Res-Earth 123, 1546-1565.

Mayaud, J.R., Bailey, R.M., Wiggs, G.F.S., Weaver, C.M., 2017. Modelling aeolian sand transport using a dynamic mass balancing approach. Geomorphology 280, 108-121.

Merrison, J.P., 2012. Sand transport, erosion and granular electrification. Aeolian Research 4, 1-16.

Middleton, G., Southard, J., 1984. Mechanics of Sediment Movement. Soc. of Econ. Paleontol. and Mineral., Tulsa, Okla.

Miles, J., Thorpe, A., Russell, P., Masselink, G., 2014. Megaripple dynamics on a dissipative sandy beach. Journal of Coastal Research, 187-192.

Mitha, S., Tran, M.Q., Werner, B.T., Haff, P.K., 1986. The Grain-Bed Impact Process in Aeolian Saltation. Acta Mech 63, 267-278.

Namikas, S.L., 2003. Field measurement and numerical modelling of aeolian mass flux distributions on a sandy beach. Sedimentology 50, 303-326.

Neuman, C.M., Bedard, O., 2017. A wind tunnel investigation of particle segregation, ripple formation and armouring within sand beds of systematically varied texture. Earth Surface Processes and Landforms 42, 749-762.

Ni, J.R., Li, Z.S., Mendoza, C., 2003. Vertical profiles of aeolian sand mass flux. Geomorphology 49, 205-218.

Nickling, W.G., 1978. Eolian Sediment Transport during Dust Storms - Slims River Valley, Yukon Territory. Can J Earth Sci 15, 1069-1084.

Nickling, W.G., 1988. The Initiation of Particle Movement by Wind. Sedimentology 35, 499-511.

Nickling, W.G., Neuman, C.M., 2009. Aeolian sediment transport, Geomorphology of desert environments. Springer, 517-555.

Nield, J.M., Baas, A.C.W., 2008. Investigating parabolic and nebkha dune formation using a cellular automaton modelling approach. Earth Surface Processes and Landforms 33, 724-740.

Nishimura, K., Hunt, J.C.R., 2000. Saltation and incipient suspension above a flat particle bed below a turbulent boundary layer. J Fluid Mech 417, 77-102.

O'Brien, P., Neuman, C.M., 2019. Experimental Validation of the Near-Bed Particle-Borne Stress Profile in Aeolian Transport Systems. J Geophys Res-Earth 124, 2463-2474.

Okin, G.S., 2005. Dependence of wind erosion and dust emission on surface heterogeneity: Stochastic modeling. Journal of Geophysical Research: Atmospheres 110.

Owen, P.R., 1964. Saltation of Uniform Grains in Air. J Fluid Mech 20, 225-242.

Pahtz, T., Clark, A.H., Valyrakis, M., Duran, O., 2020. The Physics of Sediment Transport Initiation, Cessation, and Entrainment Across Aeolian and Fluvial Environments. Rev Geophys 58.

Pahtz, T., Parteli, E.J.R., Kok, J.F., Herrmann, H.J., 2014. Analytical model for flux saturation in sediment transport. Phys Rev E 89.

Pahtz, T., Valyrakis, M., Zhao, X.H., Li, Z.S., 2018. The Critical Role of the Boundary Layer Thickness for the Initiation of Aeolian Sediment Transport. Geosciences 8.

Parteli, E.J.R., Duran, O., Bourke, M.C., Tsoar, H., Poschel, T., Herrmann, H., 2014. Origins of barchan dune asymmetry: Insights from numerical simulations. Aeolian Research 12, 121-133.

Pelletier, J.D., 2009. Controls on the height and spacing of eolian ripples and transverse dunes: A numerical modeling investigation. Geomorphology 105, 322-333.

Pi, H., Sharratt, B., Feng, G., Lei, J., Li, X., Zheng, Z., 2016. Validation of SWEEP for creep, saltation, and suspension in a desert-oasis ecotone. Aeolian Research 20, 157-168.

Pi, H.W., Feng, G., Sharratt, B.S., Li, X.H., Zheng, Z.H., 2014. Validation of SWEEP for Contrasting Agricultural Land Use Types in the Tarim Basin. Soil Science 179, 433-445.

Prigozhin, L., 1999. Nonlinear dynamics of Aeolian sand ripples. Phys Rev E 60, 729-733.

Prospero, J.M., Lamb, P.J., 2003. African droughts and dust transport to the Caribbean: Climate change implications. Science 302, 1024-1027.

Qi, L., Dong, F., Chen, Q., Wang, B., 2001. Study of onset-wind-speed of blown sand. Mechanics in engineering 23, 13-14.

Qian, G.Q., Dong, Z.B., Zhang, Z.C., Luo, W.Y., Lu, J.F., Yang, Z.L., 2015. Morphological and sedimentary features of oblique zibars in the Kumtagh Desert of Northwestern China. Geomorphology 228, 714-722.

Rajagopal, K., Massoudi, M., Ekmann, J., 1990. Mathematical modeling of fluid-solid mixtures. USDOE Pittsburgh Energy Technology Center (PETC), PA (United States).

Rajagopal, K.R., Gupta, G., Yalamanchili, R.C., 2000. A rheometer for measuring the properties of granular materials. Particul Sci Technol 18, 39-55.

Rasmussen, K., Mikkelsen, H., 1991. Wind tunnel observations of aeolian transport rates, Aeolian Grain Transport 1. Springer, 135-144.

Rasmussen, K.R., Merrison, J., Nornberg, P., 2011. Wind tunnels for the study of particle transport. IntechOpen.

Rasmussen, K.R., Mikkelsen, H.E., 1998. On the efficiency of vertical array aeolian field traps. Sedimentology 45, 789-800.

Rice, M.A., Willetts, B.B., Mcewan, I.K., 1995. An Experimental-Study of Multiple Grain-Size Ejecta Produced by Collisions of Saltating Grains with a Flat Bed. Sedimentology 42, 695-706.

Roney, J.A., White, B.R., 2004. Definition and measurement of dust aeolian thresholds. J Geophys Res-Earth 109.

Rozier, O., Narteau, C., Gadal, C., Claudin, P., du Pont, S.C., 2019. Elongation and Stability of a Linear Dune. Geophys Res Lett 46, 14521-14530.

Samarkandi, O.A., Khan, A.A., Alazmy, W., Alobaid, A.M., Bashatah, A.S., 2017. The pulmonary consequences of sandstorms in Saudi Arabia: a comprehensive review and update. Am J Disaster Med 12, 179-188.

Sarre, R., 1987. Aeolian sand transport. Progress in Physical Geography 11, 157-182.

Sauermann, G., Kroy, K., Herrmann, H.J., 2001. Continuum saltation model for sand dunes. Phys Rev E 64.

Scott, W.D., Hopwood, J.M., Summers, K.J., 1995. A Mathematical-Model of Suspension with Saltation. Acta Mech 108, 1-22.

Seppala, M., Linde, K., 1978. Wind-Tunnel Studies of Ripple Formation. Geogr Ann A 60, 29-42.

Shao, Y., Raupach, M.R., 1993. Effect of Saltation Bombardment on the Entrainment of Dust by Wind. J Geophys Res-Atmos 98, 12719-12726.

Shao, Y.P., 2005. A similarity theory for saltation and application to aeolian mass flux. Bound-Lay Meteorol 115, 319-338.

Shao, Y.P., Raupach, M.R., Leys, J.F., 1996. A model for predicting aeolian sand drift and dust entrainment on scales from paddock to region. Aust J Soil Res 34, 309-342.

Sharp, R.P., 1963. Wind Ripples. J Geol 71, 617-636.

Sharratt, B., Feng, G., Wendling, L., 2007. Loss of soil and PM10 from agricultural fields associated with high winds on the Columbia Plateau. Earth Surface Processes and Landforms 32, 621-630.

Sharratt, B.S., Feng, G., 2009. Windblown dust influenced by conventional and undercutter tillage within the Columbia Plateau, USA. Earth Surface Processes and Landforms 34, 1323-1332.

Sherman, D.J., 2020. Understanding wind-blown sand: Six vexations. Geomorphology 366.

Sherman, D.J., Li, B.L., Ellis, J.T., Swann, C., 2018. Intermittent Aeolian Saltation: A Protocol for Quantification. Geogr Rev 108, 296-314.

Sherman, D.J., Swann, C., Barron, J.D., 2014. A high-efficiency, low-cost aeolian sand trap. Aeolian Research 13, 31-34.

Sherman, D.J., Zhang, P., Martin, R.L., Ellis, J.T., Kok, J.F., Farrell, E.J., Li, B.L., 2019. Aeolian Ripple Migration and Associated Creep Transport Rates. Geosciences 9.

Silvestro, S., Chojnacki, M., Vaz, D.A., Cardinale, M., Yizhaq, H., Esposito, F., 2020. Megaripple Migration on Mars. J Geophys Res-Planet 125.

Silvestro, S., Fenton, L.K., Vaz, D.A., Bridges, N.T., Ori, G.G., 2010. Ripple migration and dune activity on Mars: Evidence for dynamic wind processes. Geophys Res Lett 37.

Siminovich, A., Elperin, T., Katra, I., Kok, J.F., Sullivan, R., Silvestro, S., Yizhaq, H., 2019. Numerical Study of Shear Stress Distribution Over Sand Ripples Under Terrestrial and Martian Conditions. J Geophys Res-Planet 124, 175-185.

Spaan, W., Van den Abeele, G., 1991. Wind borne particle measurements with acoustic sensors. Soil technology 4, 51-63.

Stout, J.E., Fryrear, D.W., 1989. Performance of a Windblown-Particle Sampler. T Asae 32, 2041-2045.

Stout, J.E., Zobeck, T.M., 1996. The Wolfforth field experiment: A wind erosion study. Soil Science 161, 616-632.

Sullivan, R., Kok, J.F., 2017. Aeolian saltation on Mars at low wind speeds. J Geophys Res-Planet 122, 2111-2143.

Sullivan, R., Kok, J.F., Katra, I., Yizhaq, H., 2020. A Broad Continuum of Aeolian Impact Ripple Morphologies on Mars is Enabled by Low Wind Dynamic Pressures. J Geophys Res-Planet 125.

Sun, Q.C., Wang, G.Q., Xu, Y., 2001. DEM applications to aeolian sediment transport and impact process in saltation. Particul Sci Technol 19, 339-353.

Swann, C., Sherman, D., Ewing, R.C., 2020. Experimentally Derived Thresholds for Windblown Sand on Mars. Geophys Res Lett 47.

Swann, C., Sherman, D.J., 2013. A bedload trap for aeolian sand transport. Aeolian Research 11, 61-66.

Tsiouri, V., Kakosimos, K.E., Kumar, P., 2015. Concentrations, sources and exposure risks associated with particulate matter in the Middle East Area—a review. Air Quality, Atmosphere & Health 8, 67-80.

Tsoar, H., 2013. Critical environments: Sand dunes and climate change, Aeolian Geomorphology. Elsevier Inc., pp. 414-427.

Ungar, J.E., Haff, P.K., 1987. Steady-State Saltation in Air. Sedimentology 34, 289-299.

Valance, A., Rasmussen, K.R., El Moctar, A.O., Dupont, P., 2015. The physics of Aeolian sand transport. Cr Phys 16, 105-117.

Van Rijn, L.C., 1993. Principles of sediment transport in rivers, estuaries and coastal seas. Aqua publications Amsterdam.

van Rijn, L.C., Strypsteen, G., 2020. A fully predictive model for aeolian sand transport. Coastal Engineering 156.

Walker, J.D., 1981. An experimental study of wind ripples. Massachusetts Institute of Technology.

Wang, P., Zhang, J., Dun, H.C., Herrmann, H.J., Huang, N., 2020. Aeolian Creep Transport: Theory and Experiment. Geophys Res Lett 47.

Wang, X.L., Chow, J.C., Kohl, S.D., Yatavelli, L.N.R., Percy, K.E., Legge, A.H., Watson, J.G., 2015. Wind erosion potential for fugitive dust sources in the Athabasca Oil Sands Region. Aeolian Research 18, 121-134.

Wang, Y., Wang, D.W., Wang, L., Zhang, Y., 2009. Measurement of sand creep on a flat sand bed using a high-speed digital camera. Sedimentology 56, 1705-1712.

Wang, Z.T., Zheng, X.J., 2004. Theoretical prediction of creep flux in aeolian sand transport. Powder Technol 139, 123-128.

Werner, B.T., 1995. Eolian Dunes - Computer-Simulations and Attractor Interpretation. Geology 23, 1107-1110.

Werner, B.T., Haff, P.K., 1988. The Impact Process in Aeolian Saltation - Two-Dimensional Simulations. Sedimentology 35, 189-196.

White, B.R., Schulz, J.C., 1977. Magnus Effect in Saltation. J Fluid Mech 81, 497-512.

Wiberg, P.L., Smith, J.D., 1985. A Theoretical-Model for Saltating Grains in Water. J Geophys Res-Oceans 90, 7341-7354.

Willetts, B., McEwan, I., Rice, M., 1991. Initiation of motion of quartz sand grains, Aeolian Grain Transport 1. Springer, pp. 123-134.

Willetts, B.B., Rice, M.A., Nickling, W., 1986. Collision in aeolian transport: the saltation/creep link.

Williams, G., 1964. Some Aspects of the Eolian Saltation Load. Sedimentology 3, 257-287.

Wu, J., Sun, H., Li, J., Luo, S., 2011a. Experimental research on threshold wind velocity for creeping sand. J. Desert Res 31, 571-574.

Yang, X., He, Q., Aili, M., 2011. Sand-transporting of sand flow at the Tazhong area in the hinterland of the Taklimakan Desert. Arid Land Geogr. 34 (3), 479–485 (in Chinese with English abstract).

Yizhaq, H., 2004. A simple model of aeolian megaripples. Physica A 338, 211-217.

Yizhaq, H., 2008. Aeolian Megaripples: Mathematical Model and Numerical Simulations. Journal of Coastal Research 24, 1369-1378.

Yizhaq, H., Balmforth, N.J., Provenzale, A., 2004. Blown by wind: nonlinear dynamics of aeolian sand ripples. Physica D 195, 207-228.

Yizhaq, H., Bel, G., Silvestro, S., Elperin, T., Kok, J.F., Cardinale, M., Provenzale, A., Katra, I., 2019. The origin of the transverse instability of aeolian megaripples. Earth Planet Sc Lett 512, 59-70.

Yizhaq, H., Isenberg, O., Wenkart, R., Tsoar, H., Karnieli, A., 2009. Morphology and dynamics of aeolian mega-ripples in Nahal Kasuy, southern Israel. Israel Journal of Earth Sciences 57, 149-165.

Zhan, K.J., Liu, S.Z., Yang, Z.H., Fang, E.T., Zhou, L.P., Wang, Q.Q., Guo, S.J., Zhang, J.H., Huang, N., 2017. Suspended dust particle characteristics during an sandstorm on 29 February 2008 in Minqin area, China. Aeolian Research 25, 79-86.

Zhang, K.C., Qu, J.J., Zu, R.P., Fang, H.Y., 2005. Temporal variations of sandstorms in Minqin oasis during 1954-2000. Environ Geol 49, 332-338.

Zhang Pei., S.D., Li Bailiang, 2021. Aeolian Creep Transport: A Review, Zenodo.

Zhang, Y., Wang, Y., Yang, B., Jia, P., 2016. Measurement of sand creep on a flat sand bed using a high-speed digital camera: Mesoscopic features of creeping grains. Sedimentology 63, 629-644.

Zhao, X., Li, Z., 2008. Transition of probability of sand grain creep at the initial stage of aeolian transport. Arid Land Geography 31, 348-354.

Zheng, X., 2009. Mechanics of wind-blown sand movements. Springer Science & Business Media.

Zheng, X.J., Xie, L., Zhou, Y.H., 2005. Exploration of probability distribution of velocities of saltating sand particles based on the stochastic particle-bed collisions. Phys Lett A 341, 107-118.

Zheng, X.J., Xie, L., Zou, X.Y., 2006. Theoretical prediction of liftoff angular velocity distributions of sand particles in windblown sand flux. J Geophys Res-Atmos 111.

Zhu, B.Q., Yu, J.J., Rioual, P., Ren, X.Z., 2014. Particle size variation of aeolian dune deposits in the lower reaches of the Heihe River basin, China. Sediment Geol 301, 54-69.

Zhu, W., 2011. Investigations on the Formation and Evolution of Aeolian Sand Ripples. Lanzhou University Lanzhou, China.

Zimbelman, J.R., 2010. Transverse Aeolian Ridges on Mars: First results from HiRISE images. Geomorphology 121, 22-29.

Zimbelman, J.R., Irwin, R.P., Williams, S.H., Bunch, F., Valdez, A., Stevens, S., 2009. The rate of granule ripple movement on Earth and Mars. Icarus 203, 71-76.

Zobeck, T.M., Sterk, G., Funk, R., Rajot, J.L., Stout, J.E., Van Pelt, R.S., 2003. Measurement and data analysis methods for field-scale wind erosion studies and model validation. Earth Surface Processes and Landforms 28, 1163-1188.

CHAPTER 3 AN ALGORITHM FOR OBJECTIVE ANALYSIS OF GRAINFLOW MORPHOLOGY

Abstract:

Grainflows produce temporary geomorphological signatures on the slipfaces of aeolian dunes, and are a fundamental agency by which dunes migrate. The purpose of this study is to present an algorithm to objectively and efficiently delineate grainflow boundaries by processing Digital Elevation Models (DEMs) in Matlab and ArcGIS. Grainflows can be identified by analyzing temporal changes in slipface elevation, and the morphology can be extracted by defining the boundary that encloses the area of movement. The method allows large numbers of grainflows to be quickly and objectively delineated and extracted from LiDAR data. The process avoids the subjective nature of manual measurement, thereby improving the commensurability of different grainflow regimes in both terrestrial and extraterrestrial environments. The algorithm is presented here in the context of analyzing grainflows and related processes on the slipfaces of dunes, but it is applicable over the broader scope of other forms of slope failure and geophysical flows, such as avalanches, snowslides, landslides, and debris flows.

Keywords: Dune migration, Sediment transport, Aeolian geomorphology, Terrestrial Laser Scanning, Digital Elevation Model

Introduction

Grainflow is a gravity-driven sediment transport process typical on the slipfaces of aeolian dunes. It is an important process that shapes slipface morphology and contributes to dune migration. Therefore, a better understanding of grainflow morphology (e.g., length, width, and shape) is warranted to elucidate the dynamics of dune migration and sediment transport processes on slipfaces. Studies of grainflows provide a basic understanding of their dynamics in both aeolian and non-aeolian environments on earth (Gomez et al., 2002; Loope et al., 2012; Görüm, 2019), and provide an important analog for sand transport and dune migration on Mars (Silvestro et al., 2010). When sediment is deposited near a dune

brink line (i.e., the top of the slipface), a topographic grainflow bulge forms and steepens the local surface. When the local slope exceeds the angle of repose, a grainflow will redistribute the sediment and relax the local slope. Most grainflows, therefore, begin near the brink line of a sand dune (Anderson, 1988; Nickling et al., 2002; Sutton et al., 2013a, b; Cornwall et al., 2018b). After a grainflow stops, it leaves prominent signatures on a slipface, namely a scarp and erosion alcove on the upper portion of the slope and a deposition tongue on the lower slope (Sutton et al., 2013a; Cornwall et al., 2018b). These shapes are the signatures of a grainflow.

Although it is easy to identify grainflow signatures by differencing time series of Digital Elevation Models (DEMs), there have been relatively few studies that have done so (e.g., Sutton et al., 2013a; Nield et al., 2017b; Cornwall et al., 2018b). The challenge for developing an algorithm to delineate a grainflow signature is in automatically linking the conjoined grainflow sections of erosion and accretion, either of which can be identified with object-oriented processing (e.g., Liu et al., 2010a). This challenge is also common to the delineation of boundaries in landslide studies (McKean and Roering, 2004; Görüm, 2019; Tang et al., 2019; Pirasteh et al., 2020), where manual tracing of a landslide boundary remains the means for extracting morphology from a DEM. Manual methods are, however subjective and, when treating with large sample sizes, tedious and time inefficient.

Grainflow signatures are indicators of sediment transport processes on a slipface, which reflect the influence of wind speed, secondary flow circulations, and topographic variations (Breed et al., 1979; Sweet and Kocurek, 1990; Mcdonald and Anderson, 1995; Acosta et al., 2007; Cornwall et al., 2018b; Dundas, 2020). The preserved signatures in strata can reveal the history of a dune migration and be formulated to predict the evolution of aeolian dune systems (Hunter, 1985; Sweet et al., 1988; McDonald and Anderson, 1996; Nickling et al., 2002; Cornwall et al., 2018a; Cornwall et al., 2018b; Dundas, 2020). However, there are few studies for geometric analysis of grainflow boundaries (Ewing et al., 2017; Cornwall et al., 2018a; Cornwall et al., 2018b). This study presents an algorithm that was developed to objectively and rapidly extract what amounted to 1609 grainflow signatures and delineate their shapes from sequential DEMs made from a barchan slipface in the Jericoacoara dune field in Brazil. There is no

other algorithm currently qualified for the task, especially when two or more adjacent grainflows require segregation. This method uses a polygon mask to guide a GIS function to identify multiple grainflows and automatically delineate the boundaries of individual grainflows in Matlab. Another benefit of this method is it is a solution to the challenge of conjoining the erosional and accretional sections of scarp and tongue/lobe signatures.

Review of literature

There have been several studies concerning grainflow dynamics on dunes (Mcdonald and Anderson, 1995, 1996; Daerr and Douady, 1999; Tischer et al., 2001; Borzsonyi et al., 2008), but few concern grainflow signatures. One of the earlier field experiments to study grainflow signatures was done by Breton et al. (2008). They used a video camera to document the grainflows on the slipface of a dune in the Namib Desert. The recorded grainflow images were transferred onto the acetate paper to manually measure the lengths and widths of grainflows. The length measurements were geometrically corrected by assuming a surface slope angle of 32º, and no correction was made on width. The areas were estimated by multiplying the corrected lengths and widths and by assuming either a trapezoid or kite shape for a grainflow.

Sutton et al. (2013a) studied grainflow-induced topographic variations by building a sand dune in a wind tunnel. The topographic details of the slipface were measured by a laser scanner and stored in DEMs. By differencing the sequential DEMs, they found that their grainflow signatures were of hourglass shape. Using DEMs from their field studies, Nield et al. (2017b) and Cornwall et al. (2018b) found that grainflows occurred in a range of shapes, of which hourglass was but one.

Ewing et al. (2017) reported four characteristic dimensions of grainflows, derived from DEMs from Mars and Earth. The characteristic dimensions are scarp width, scarp length, lobe width, and lobe length, manually measured using tools in ArcGIS and Qgis. Cornwall et al. (2018b) used a ground-based laser scanner and a video camera to record grainflows on the southern end of Gran Canaria island, Spain and manually measured three characteristic dimensions of grainflows drawn on the video images:

specifically, grainflow length, initiation point width, and base width. Cornwall et al. (2018a) also included the characteristic dimensions of grainflows on Mars.

The literature on this subject suggests that images captured by camera and DEMs are the two main methods used to study grainflow morphology. In capturing grainflow images, researchers obtained some characteristic dimensions of grainflows by manual measurement, with or without length or width corrections (McDonald and Anderson, 1996; Borzsonyi et al., 2008; Breton et al., 2008). Studies that process sequential DEMs can not only derive grainflow dimensions but also calculate the resulting grainflow-induced amount of sediment transport (Sutton et al., 2013b; Nield et al., 2017b; Cornwall et al., 2018b).

Experiments have been conducted to study grainflows by analyzing sequential DEMs to produce the Difference of DEMs (DoDs) (Sutton et al., 2013a; Nield et al., 2017b; Cornwall et al., 2018b). The grainflows are characterized by erosional scallop, with negative DoDs, in the upper slope, and an accretional fan, with positive DoDs, in the lower slope. Further, where there are multiple grainflows present in a single DoD, especially when they are in close proximity, their signatures may be complex enough that it becomes difficult to correctly distinguish individual grainflows. In such cases a conceptual challenge is to isolate individual signatures.

Method

Study site

Field experiments were conducted on November 7 and 9, 2013, in the Jericoacoara dune field, Ceará, Brazil, to observe grainflows on the slipface of a barchan. The dune (40°32'17.66"W, 2°49'53.08"S) was 21.3 m high, and the horizontal length of the slipface that was scanned was about 80 m. A Leica C10, Terrestrial Laser Scanning (TLS) was used to measure the slipface elevation. The TLS was located at a fixed location downwind of the dune. Once initiated, scanning was continuous, and each scan required about seven minutes to complete one traverse slipface. A total of 56 and 61 scans were collected within 7.15 hours and 7.5 hours on November 7 and November 9, respectively. The point clouds

were georeferenced, filtered, and interpolated to create DEMs, following Pelletier et al. (2015). A video camera with resolution 1440×1088 pixels was set on a tripod to record the grainflows dynamical movement processes. The video camera was located about 20 meters downwind from the centroid of the slipface and adjacent to the scanner. The video images were used to compare the results of this method. The video camera field view was only wide enough to cover the grainflows along the central slipface approximately 20 m.

Extraction method

The workflow chart (Figure 3.1) describes the processes applied to the DEMs and shows examples from the data set. The steps are described below.

Dataset

In this study, the DEM files are established from sequentially scanned point clouds that are binary, floating raster-files with ".rtg" extensions. The pixel size of the DEMs is 0.04 m, with a vertical resolution of 2 mm. The dimension of each DEM is 1126 rows × 2001 columns. The files can be read and visualized with the Matlab "fopen" and "fread" functions with the above-described metadata. Another standard extension of DEM files, ".tif" can also be read and visualized with either the above two functions or "imread" in Matlab. Alternatively, it can be directly imported and opened into software like ArcMap, Qgis, or Erdas Imagine. The key steps to process the DEMs are presented in Figure 3.1, and the details are described below.

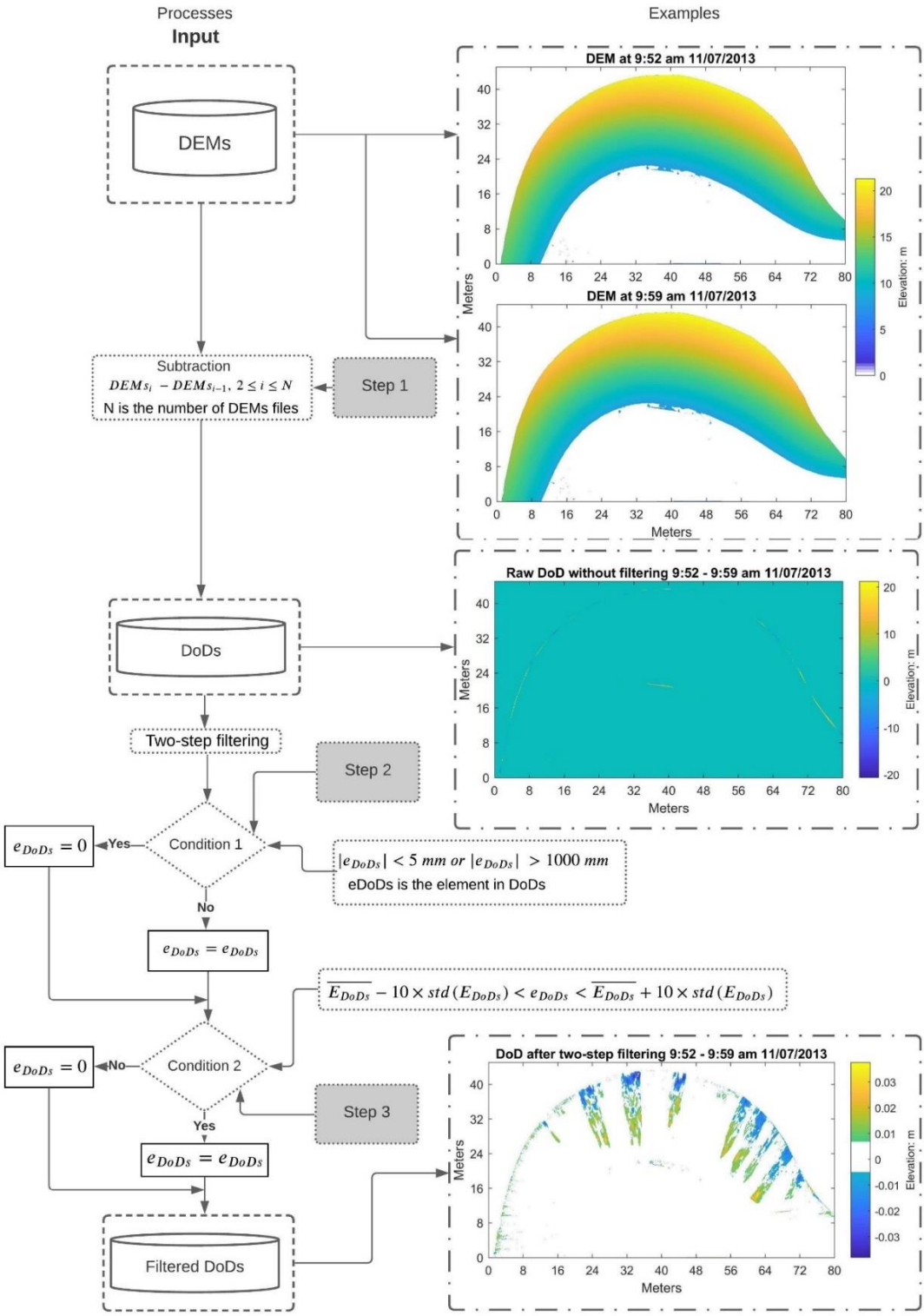
Processes
Input
Examples
DEMs
DEM at 9:52 am 11/07/2013
DEM at 9:59 am 11/07/2013
Meters
Elevation: m
Subtraction
$DEMs_i - DEMs_{i-1}$, $2 \le i \le N$
N is the number of DEMs files
Step 1
DoDs
Raw DoD without filtering 9:52 - 9:59 am 11/07/2013
Two-step filtering
Step 2
Condition 1
$e_{DoDs} = 0$
Yes
No
$|e_{DoDs}| < 5\ mm\ or\ |e_{DoDs}| > 1000\ mm$
eDoDs is the element in DoDs
$e_{DoDs} = e_{DoDs}$
$\overline{E_{DoDs}} - 10 \times std(E_{DoDs}) < e_{DoDs} < \overline{E_{DoDs}} + 10 \times std(E_{DoDs})$
Condition 2
Step 3
DoD after two-step filtering 9:52 - 9:59 am 11/07/2013
Filtered DoDs

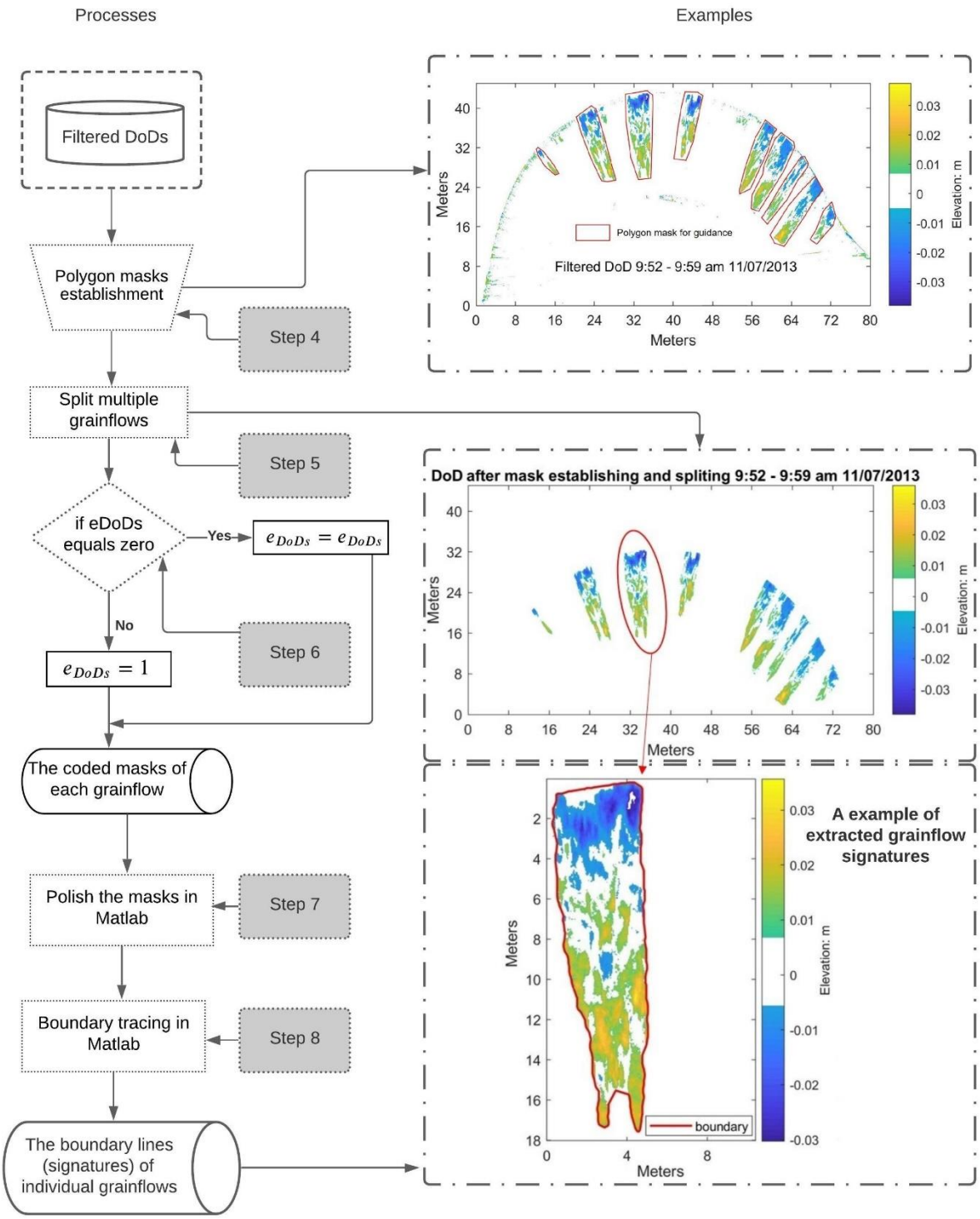

Figure 3. 1. The processes and examples to identify and extract multiple grainflows from the DEMs of the slipface. The detailed steps are described in the main text.

DEM processing and noise filtering

With sequential DEMs, DoDs are derived in step 1 (Figure 3.1) by subtracting the DEM_i from DEM_{i-1}, where $2 \leq i \leq N$ (N is the number of the DEMs files). The raw DoDs include too much noise to see a grainflow (an example of a raw DoD is the third image in Figure 3.1). A two-step filtering process is applied to remove outliers and extreme noise. First, the DoDs with absolute values |DoDs|>1000 mm or |DoDs|<5 mm are treated as noise and reset to zero (step 2 in Figure 3.1). The noise (|DoDs|>1000 mm) come from sequential DEMs offset along the brink line. The threshold value "|DoDs|>5 mm" is adopted to detect elevation changes and exclude potential errors from the buffeting of the instrument by wind gusts, as suggested by Pelletier et al. (2015). After the first filtering process, it remains difficult to discern any grainflow signatures. Therefore, a second filtering process is applied (step 3, Figure 3.1). Two other threshold values are adopted to remove some extreme values: in this case, mean values plus or minus ten times standard deviations of the results from the first step filtering. These two threshold values are determined by trial and error, which filter out the extreme values while preserving a wide variation range for DoDs. Multiple grainflows become apparent after the two-step filtering process (the fourth image in Figure 3.1).

Grainflow identification

The method to identify individual grainflows requires some supervised work, needing a polygon mask to guide the function ("Extract by Mask") in ArcGIS to identify individual grainflows from the slipface (step 4, Figure 3.1). The polygon mask works as a guide to isolate individual grainflows. Without this guidance, the function would often fail to distinguish one grainflow from adjacent ones. As shown in Figure 3.1 (step 4), the mask does not include the boundary shape. Instead, it guides the function to identify individual grainflows properly. It typically requires 5 – 10 seconds to identify and mask one grainflow. Based on the established mask, a function "Split Raster" in ArcGIS (step 5) is used to split multiple grainflows into individuals. The output files are the individual grainflows extracted from each DoD.

Signature extraction

Before extracting grainflow signatures, it is necessary to code the grainflows (step 6). Pixels within erosion or accretion zones are coded as 1. These zones are polished by ignoring pixels in cases where there are fewer than four contiguous pixels coded as 1 (step 7). This is necessary to remove the influence of randomly scattered pixel sets (<4) and keep the boundary shape of a grainflow. The scattered pixel sets (<4) may come from the buffeting of the sensor. The threshold value of four pixels was determined by trial and error. Without the polishing process (step 7), the area of a particular grainflow will be expanded. Figure 3.2 shows an example of the influence of step 7. This polishing process is done through a Matlab built-in function, "bwareaopen.m" and the final step (step 8) is to extract grainflow boundaries with the Matlab function, "boundary.m". Two input variables for the "boundary" function are the polished zones indices and an adjustment scalar, "S" (0 - 1). The adjustment scalar is used to extract a compact and smooth boundary that envelops the input coded mask, and is determined by comparing the corresponding grainflows from video images and trial and error. The larger the value of "S", the more compact the boundary will be. If "S" is too large, it will cause some artificial holes (Figure 3.3c); otherwise, it will show a rough boundary line that distorts the real boundary shape of a grainflow (Figure 3.3a). The adjustment scalar is set as 0.8 to extract grainflow signatures by comparing the corresponding grainflow from video images (Figure 3.3b).

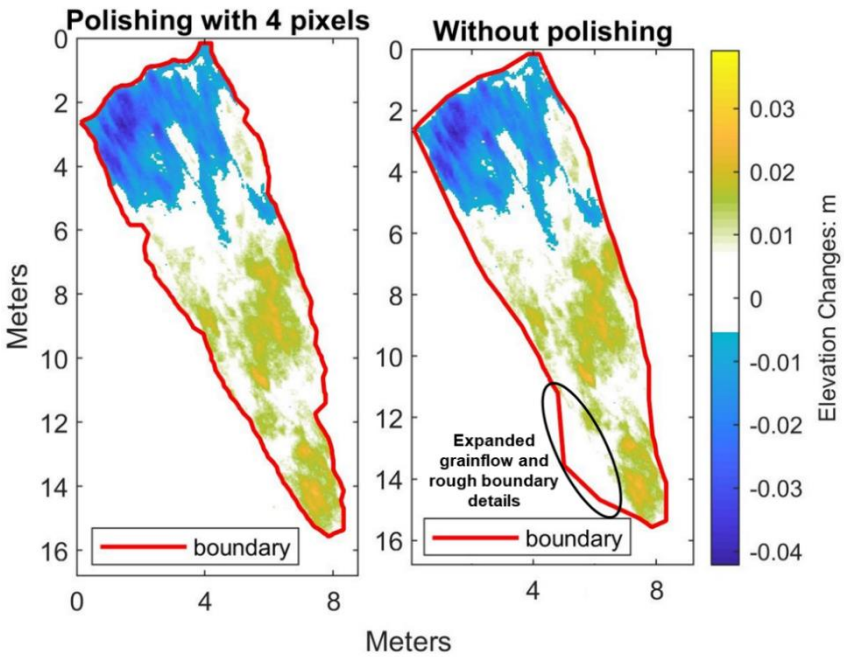

Figure 3. 2. The influence of the polishing step on extracting grainflow boundary

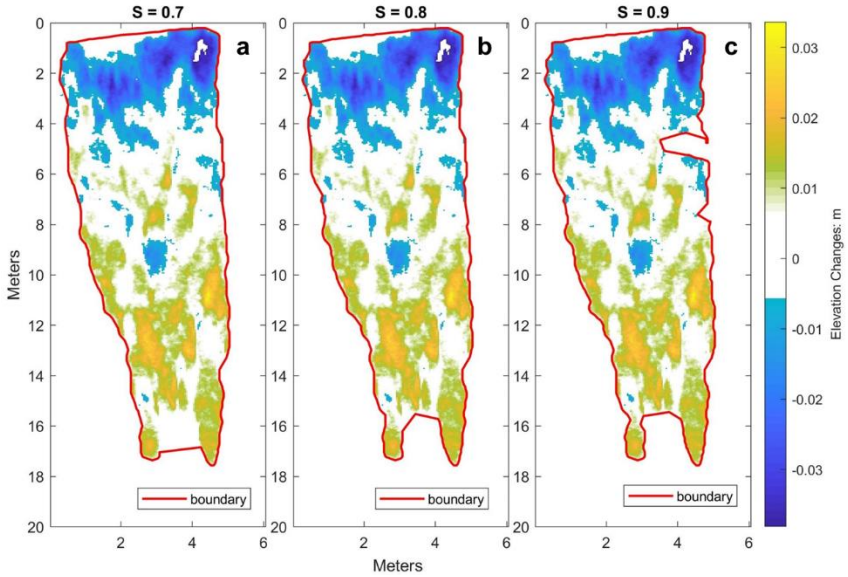

Figure 3. 3. The influence of adjustment scalar (S) on extracting grainflow boundary shape

Results

This method is evaluated by comparing the boundary shape of extracted grainflow signatures with the corresponding grainflow recorded by the video camera. Figure 3.4 shows an example with a manually drawn boundary, obtained by carefully analyzing the corresponding grainflow video. By

analyzing only the video image in Figure 3.4 (b), for example, it is difficult to draw the grainflow boundary because the previous grainflow signatures on the slipface are often misinterpreted. Because of the influence of the field view of the video image, the extracted grainflow signatures (Figure 3.4 (a)) are rotated for visual comparison in Figure 3.4. After comparing 151 extracted grainflows and corresponding grainflows from video images, it is found that the extraction method works well. Note that in Figure 3.4, the grainflows do not precisely match because of the different projections of the DoDs and the video image.

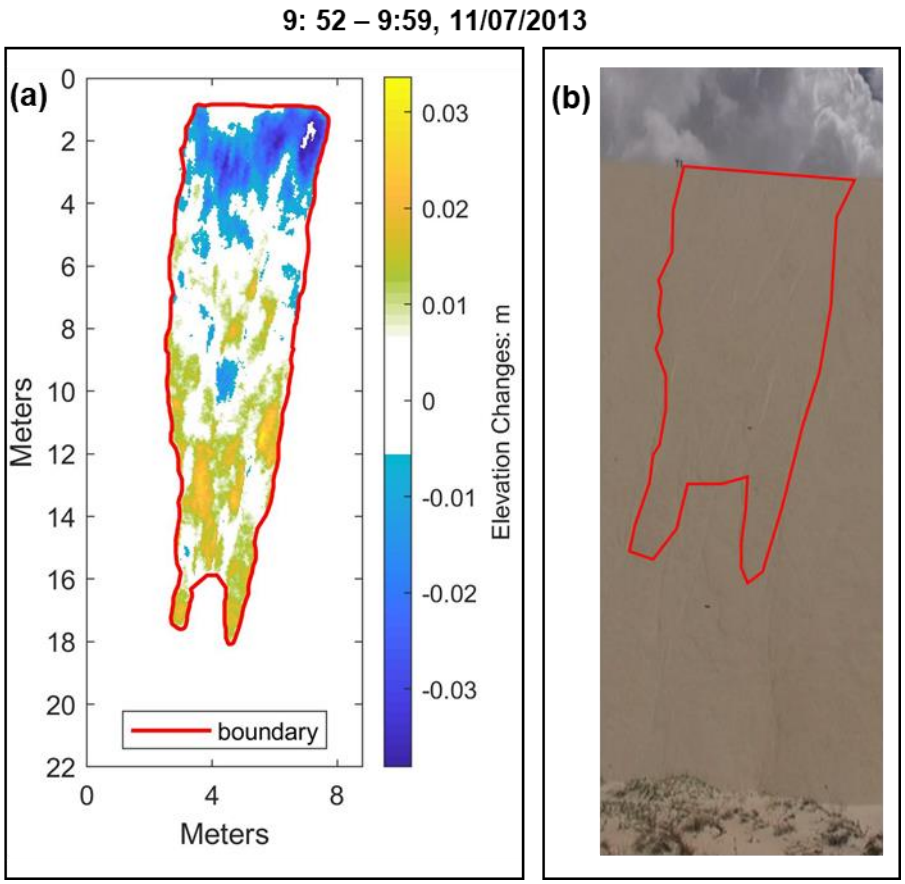

Figure 3. 4. (a) Extracted grainflow boundary from DEMs and (b) The corresponding grainflow from the video image

Discussion

The priority of this method is to establish a mask to guide a function to identify individual grainflows, and then automatically extract their signatures. Without the mask, the function cannot distinguish two or more adjacent grainflows. The mask is created by supervising grainflow distributions.

The comparison in Figure 3.4 indicates that the extracted grainflow is consistent with the corresponding grainflow delineated from the video record. The efficiency of this method is assessed by processing 117 scans in the Jericoacoara dune field. For this method, it requires 5 – 30 minutes to set up the workspace environment in Matlab and ArcGIS, depending on the users' familiarity with the software. It took less than four hours to identify and extract 1609 grainflows with this method. In contrast, using a manual method, it might take 100 – 160 hours to identify and extract the same number of grainflows from video images. If tracing a boundary from DoDs, it requires approximately 120 – 180 seconds to carefully digitize the boundary of one grainflow; and therefore would require 50 – 80 hours to process the 1609 grainflows. The efficiency of this method relative to manual methods increases rapidly when analyzing more than five grainflows from video images or more than fifteen from DoDs. In the event that there are only a few grainflows to analyze, it may be more efficient to manually trace the grainflow boundaries. In the landslide study by Görüm (2019), 902 landslides were traced (digitalized) manually. If each boundary required one or two minutes, that process would take 15 to 30 hours to complete. With the algorithm presented here, that task would take about two hours. Every manual measurement, however, is to some degree subjective and may vary based on the decisions of the researcher performing it or the number of measurements made by an individual.

Delineating grainflow signatures from DoDs is important for LiDAR-based studies of grainflow morphology (e.g., the length, width, compactness, and boundary shape) and for studies of the amount of sediment transport. After a grainflow boundary is extracted from a DoD it is relatively simple to quantify the morphological characteristics. For example, Pirasteh et al. (2020) presented an algorithm to automatically calculate the length, width, and area of manually-delineated landslide boundaries. The algorithm presented here standardizes the delineation of a grainflow boundary, avoiding the subjective nature of manual measurement. This method is also applicable to quantify the amount of sediment transport in non-aeolian environments when DEMs are available before and after sediment movement, e.g., snowslides, landslides, and debris flows (Claessens et al., 2005; Rivera et al., 2005; Gruber and Bartelt, 2007; Tsutsui et al., 2007; Wheaton et al., 2010; James et al., 2012; Dou et al., 2019).

This method is independent of the processes associated with forming the grainflow signatures. Regardless of the field conditions, the algorithm works well and efficiently with sequential, noise-free DEMs. The quality of the output products is related to the scanner resolution, scan rate, and spatial resolution of the DEMs. The algorithm is a tool that can only work with the data provided. If the input DEMs are noisy or otherwise flawed, the method will carry that noise and pass it to the output products.

The scale of using this method is constrained only by the input DEMs. There is no practical upper limit. The smallest size of grainflows that can be detected is dependent on several factors: the resolution of the scanner, scan rate, DEM spatial resolution, filtering processes, and the choice of input scale values. A finer resolution scanner with a denser scan rate can capture smaller topographic differences and produce finer scale DEMs. Filtering processes may also limit the detection of small grainflows. For example, narrower ranges of thresholds applied on the two-step filtering process in Section 4.2 will miss some smaller grainflows. The input scale values for polishing grainflow boundaries and the adjustment scalar (S) to delineate the boundary also influence the smallest size of detectable grainflows.

Conclusions

This paper has described a new method to detect and extract the boundaries of grainflow signatures from DEMs. A comparison of its results with video records confirms the viability and efficiency of the method. The approach becomes increasingly efficient relative to manual methods as the number of grainflows increases beyond about 15. For samples of the order of 100, for example, the grainflows can be delineated in about 10% of the time required for manual measurement. This method is an important tool for objective analysis of sediment transport and related processes on the slipfaces of dunes, and for the broader scope of assessing other geophysical flows such as snowslides, landslides, and debris flows.

Reference List for Chapter 3

Acosta, A., Ercole, S., Stanisci, A., Pillar, V.D., Blasi, C., 2007. Coastal vegetation zonation and dune morphology in some Mediterranean ecosystems. Journal of Coastal Research 23, 1518-1524.

Anderson, R.S., 1988. The Pattern of Grainfall Deposition in the Lee of Aeolian Dunes. Sedimentology 35, 175-188.

Borzsonyi, T., Halsey, T.C., Ecke, R.E., 2008. Avalanche dynamics on a rough inclined plane. Phys Rev E 78.

Breed, C.S., Grolier, M.J., Mccauley, J.F., 1979. Morphology and Distribution of Common Sand Dunes on Mars - Comparison with the Earth. J Geophys Res 84, 8183-8204.

Breton, C., Lancaster, N., Nickling, W.G., 2008. Magnitude and frequency of grain flows on a desert sand dune. Geomorphology 95, 518-523.

Claessens, L., Heuvelink, G.B.M., Schoorl, J.M., Veldkamp, A., 2005. DEM resolution effects on shallow landslide hazard and soil redistribution modelling. Earth Surface Processes and Landforms 30, 461-477.

Cornwall, C., Bourke, M.C., Jackson, D.W.T., Cooper, J.A.G., 2018a. Aeolian slipface dynamics and grainflow morphologies on Earth and Mars. Icarus 314, 311-326.

Cornwall, C., Jackson, D.W.T., Bourke, M.C., Cooper, J.A.G., 2018b. Morphometric analysis of slipface processes of an aeolian dune: Implications for grain-flow dynamics. Sedimentology 65, 2034-2054.

Daerr, A., Douady, S., 1999. Two types of avalanche behaviour in granular media. Nature 399, 241-243.

Dou, J., Yunus, A.P., Tien Bui, D., Sahana, M., Chen, C.W., Zhu, Z.F., Wang, W.D., Pham, B.T., 2019. Evaluating GIS-Based Multiple Statistical Models and Data Mining for Earthquake and Rainfall-Induced Landslide Susceptibility Using the LiDAR DEM. Remote Sens-Basel 11.

Dundas, C.M., 2020. An aeolian grainflow model for Martian Recurring Slope Lineae. Icarus 343.

Ewing, R.C., Lapotre, M.G.A., Lewis, K.W., Day, M., Stein, N., Rubin, D.M., Sullivan, R., Banham, S., Lamb, M.P., Bridges, N.T., Gupta, S., Fischer, W.W., 2017. Sedimentary processes of the Bagnold Dunes: Implications for the eolian rock record of Mars. J Geophys Res-Planet 122, 2544-2573.

Gomez, B., Page, M., Bak, P., Trustrum, N., 2002. Self-organized criticality in layered, lacustrine sediments formed by landsliding. Geology 30, 519-522.

Görüm, T., 2019. Landslide recognition and mapping in a mixed forest environment from airborne LiDAR data. Engineering Geology 258, 105155.

Gruber, U., Bartelt, P., 2007. Snow avalanche hazard modelling of large areas using shallow water numerical methods and GIS. Environ Modell Softw 22, 1472-1481.

Hunter, R.E., 1985. A Kinematic Model for the Structure of Lee-Side Deposits. Sedimentology 32, 409-422.

James, L.A., Hodgson, M.E., Ghoshal, S., Latiolais, M.M., 2012. Geomorphic change detection using historic maps and DEM differencing: The temporal dimension of geospatial analysis. Geomorphology 137, 181-198.

Liu, H., Wang, L., Sherman, D., Gao, Y., Wu, Q., 2010a. An object-based conceptual framework and computational method for representing and analyzing coastal morphological changes. International Journal of Geographical Information Science 24, 1015-1041.

Loope, D.B., Elder, J.F., Sweeney, M.R., 2012. Downslope coarsening in aeolian grainflows of the Navajo Sandstone. Sediment Geol 265, 156-162.

Mcdonald, R.R., Anderson, R.S., 1995. Experimental-Verification of Aeolian Saltation and Lee Side Deposition Models. Sedimentology 42, 39-56.

McDonald, R.R., Anderson, R.S., 1996. Constraints on eolian grain flow dynamics through laboratory experiments on sand slopes. Journal of Sedimentary Research 66, 642-653.

McKean, J., Roering, J., 2004. Objective landslide detection and surface morphology mapping using high-resolution airborne laser altimetry. Geomorphology 57, 331-351.

Nickling, W.G., Neuman, C.M., Lancaster, N., 2002. Grainfall processes in the lee of transverse dunes, Silver Peak, Nevada. Sedimentology 49, 191-209.

Nield, J.M., Wiggs, G.F.S., Baddock, M.C., Hipondoka, M.H.T., 2017b. Coupling leeside grainfall to avalanche characteristics in aeolian dune dynamics. Geology 45, 271-274.

Pelletier, J.D., Sherman, D.J., Ellis, J.T., Farrell, E.J., Jackson, N.L., Li, B.L., Nordstrom, K.F., Maia, L.P., Omidyeganeh, M., 2015. Dynamics of sediment storage and release on aeolian dune slip faces: A field study in Jericoacoara, Brazil. J Geophys Res-Earth 120, 1911-1934.

Pirasteh, S., Shamsipour, G., Liu, G., Zhu, Q., Chengming, Y., 2020. A new algorithm for landslide geometric and deformation analysis supported by digital elevation models. Earth Science Informatics 13, 361-375.

Rivera, A., Casassa, G., Bamber, J., Kaab, A., 2005. Ice-elevation changes of Glaciar Chico, southern Patagonia, using ASTER DEMs, aerial photographs and GPS data. J Glaciol 51, 105-112.

Silvestro, S., Fenton, L.K., Vaz, D.A., Bridges, N.T., Ori, G.G., 2010. Ripple migration and dune activity on Mars: Evidence for dynamic wind processes. Geophys Res Lett 37.

Sutton, S.L.F., Neuman, C.M., Nickling, W., 2013a. Avalanche grainflow on a simulated aeolian dune. J Geophys Res-Earth 118, 1767-1776.

Sutton, S.L.F., Neuman, C.M., Nickling, W., 2013b. Lee slope sediment processes leading to avalanche initiation on an aeolian dune. J Geophys Res-Earth 118, 1754-1766.

Sweet, M., Kocurek, G., 1990. An empirical model of aeolian dune lee-face airflow. Sedimentology 37, 1023-1038.

Sweet, M.L., Nielson, J., Havholm, K., Farrelley, J., 1988. Algodones Dune Field of Southeastern California - Case-History of a Migrating Modern Dune Field. Sedimentology 35, 939-952.

Tang, C., Tanyas, H., van Westen, C.J., Tang, C., Fan, X., Jetten, V.G., 2019. Analysing post-earthquake mass movement volume dynamics with multi-source DEMs. Engineering geology 248, 89-101.

Tischer, M., Bursik, M.I., Pitman, E.B., 2001. Kinematics of sand avalanches using particle-image velocimetry. Journal of Sedimentary Research 71, 355-364.

Tsutsui, K., Rokugawa, S., Nakagawa, H., Miyazaki, S., Cheng, C.T., Shiraishi, T., Yang, S.D., 2007. Detection and volume estimation of large-scale landslides based on elevation-change analysis using DEMs extracted from high-resolution satellite stereo imagery. Ieee T Geosci Remote 45, 1681-1696.

Wheaton, J.M., Brasington, J., Darby, S.E., Sear, D.A., 2010. Accounting for uncertainty in DEMs from repeat topographic surveys: improved sediment budgets. Earth Surface Processes and Landforms 35, 136-156.

CHAPTER 4 QUANTIFICATION AND CLASSIFICATION OF GRAINFLOW MORPHOLOGY ON NATURAL DUNES

Abstract:

Grainflows (or avalanches) are fundamental mechanisms associated with the evolution and migration of dunes. This study addresses grainflow morphology on the 21.3 m and 54.5 m high slipfaces of two barchans. A series of metrics to characterize shape is developed with the perspective that this approach may provide a key to recognizing different grainflow morphodynamic regimes. We provide the first detailed and objective measurements of grainflow morphometry based on terrestrial laser scanning and subsequent image analysis of 1243 grainflows on the larger dune and 1609 from the smaller dune. Grainflow shape was classified based on five representative morphometric attributes: average length, average width, rectangularity, triangularity, and elongation. Cluster analysis indicated three recognizable grainflow types: elongated, narrow grainflows (Type 1); long, triangular grainflows (Type 2); and short, rectangular grainflows (Type 3). The distributions of grainflow types were substantially different on the larger and smaller dune, and different from distributions found on smaller dunes in other studies.

Keywords: avalanche, barchan, dune slipface, morphodynamics, aeolian geomorphology, dune migration

Introduction

Grainflow, or avalanching, is one of the main sediment transport processes on the slipfaces of dunes. Grainflows are gravity-driven failures generated by an oversteepening of a slope after deposition of windblown sand near the brink of a slipface (Du Pont et al., 2005; Fenton, 2006; Atwood-Stone and McEwen, 2013; Sutton et al., 2013a, b; Zhao et al., 2021). This process is an integral aspect of dune migration yet has received relatively little attention. Available grainflow research has focused on several main themes: the inference for paleodune height and wind strength from grainflow thickness

(Hunter, 1977; Fryberger and Schenk, 1981; Kocurek and Dott, 1981; Kocurek, 1991; Loope et al., 2001; Silvestro et al., 2010; Eastwood et al., 2012; Horgan and Bell, 2012; Loope et al., 2012; Ewing et al., 2017; Banham et al., 2018; Zhao et al., 2021); grainflow dynamics, e.g., grainflow velocity profiles or critical angles for slope failures (McDonald and Anderson, 1996; Daerr and Douady, 1999; Tischer et al., 2001; Douady et al., 2002; Robinson and Friedman, 2002; Borzsonyi et al., 2005; Sutton et al., 2013b); or grainflow magnitude and frequency (Mcdonald and Anderson, 1995; Nickling et al., 2002; Breton et al., 2008; Sutton et al., 2013a; Nield et al., 2017b; Cornwall et al., 2018b). The complex morphodynamics on a dune slipface results in variable case study findings. For example, two formation mechanisms were raised by Hunter (1977) and Fryberger and Schenk (1981). Sutton et al. (2013a) indicated that grainflow magnitude was independent of wind speeds. Nield et al. (2017b), however, suggested that grainflow magnitude increased with wind speeds.

Grainfall and creep (reptation) transport past the dune brinkline produces a small topographic bulge that grows until the angle of repose is exceeded and failure occurs. McDonald and Anderson (1996) suggested that an important step toward generating a complete model of dune evolution, stratigraphy, and migration was to develop rules to describe the redistribution of the sand deposition in a manner consistent with the grainflow process. Grainfall and creep deposits produce the initial geometry for slope failure and consequent grainflow (Anderson, 1988; McDonald and Anderson, 1996). Little is known, however, about the morphodynamic linkages between the topographic bulge and grainflow. McDonald and Anderson (1995) indicated that bulge failure may trigger frequent but thin grainflows, but they noted that this cannot explain the large (i.e., thick) grainflow deposits found in the rock records. They suggested that a large grainflow required another depositional mode to accumulate a substantial enough sand mass. Nickling et al. (2002) indicated that grainfall patterns were related to dune height and width. The results of Nield et al. (2017b) showed that a longer extension of a grainfall pattern was caused by faster winds.

Hunter (1977) reported grainflows formed from scarp recession, a failure having a scarp form migrated upslope and laterally. Fryberger & Schenk (1981) described a grainflow formation mechanism termed slump degeneration, a failure that started as a slump sheet and gradually broke up and formed a

grainflow. The cause of apparent cohesion in the dry sand, however, has not been explained. Despite this and other studies on grainflow triggers, there has not been a quantitative theory or method to account for the morphodynamics associated with sediment delivery from the upper slope to the slipface base.

Boyce and Clark (1964) suggested that morphometric characteristics of an object may indicate answers for its associated complex dynamics. Grainflow morphometry, therefore, may be a key to revealing grainflow processes on a dune slipface, which physicists and geomorphologists have described. Physicists have treated grainflow on sand piles as a representative of self-criticality (Daerr and Douady, 1999; Tischer et al., 2001). Daerr and Douady (1999) reported that two types of grainflows were triangular but triggered by different physical mechanisms: a thin layer propagating downwards and laterally owing to collisions between neighboring grains and a thick layer also propagating upwards with upper grains tumbling down because of loss of support. Tischer et al. (2001) mentioned that their grainflows were in droplet-shaped flows, discerned using particle-image velocimetry.

Aeolian geomorphologists have studied grainflows in the field and wind tunnels. Breton et al. (2008) roughly categorized two types of grainflows in their field experiments: primary grainflows that started from grainfall deposits on the upper parts of a slipface and small secondary grainflows that were triggered by disturbances from primary grainflows. They estimated the lengths and areas of those grainflows by assuming that a grainflow was either a trapezoid or kite shape. Sutton et al. (2013a) observed an hourglass shape as the typical grainflow morphology in their wind tunnel. They measured the areas and volumes of both the erosional and depositional parts of a grainflow. Ewing et al. (2017) measured Martian grainflow scarp lengths and widths, and lobe length and lobe widths using high spatial resolution imagery. They described hourglass-shaped and translational slides (moving downslope as a cohesive block) grainflow shape types.

Cornwall et al. (2018b) made field-based measurements of grainflows using a Terrestrial Laser Scanner and a video camera. They categorized four types of grainflow shapes: hourglass, slab, funnel, and lobe. Cornwall et al. (2018b) attributed hourglass and slab shapes to primary grainflows while secondary grainflows manifested as funnel and lobe shapes. They used a wedge shape to approximate grainflow

morphology by measuring grainflow widths at the upper initiation point and the base. In a complementary study of Martian dunes, Cornwall et al. (2018a) estimated grainflow dimensions using their framework with remotely sensed images.

Previous literature suggests little agreement on best practices to characterize and quantify grainflow morphology. The grainflow morphometry studies that are available are limited in that they are based on manual measurement methods and small sample sizes (from as few as five to a maximum of 76 grainflows). Therefore, the two objectives of this research are: first, to quantify grainflow morphometric attributes in a standard and objective way, and second to use those data to classify grainflows into discernable types with recognizable features. The results from this study should prove helpful in the interpretation of complex morphodynamics on dune slipfaces.

Method

Field site

The field site lies within Jericoacoara National Park, located in the municipality of Jijoca de Jericoacoara in the state of Ceará (NE Brazil, Figure 4.1). The region has a pronounced dry season when the average total precipitation is less than about 130 mm from August to December (Maia et al., 2005). Winds in the study area have a persistent and large diurnal cycle during that dry season, increasing quickly through the morning and rotating counterclockwise from ESE in the early morning to the predominant dune-migration direction of ENE in the late morning and afternoon (Pelletier et al., 2015). The strong seasonality of rainfall and wind favor sustained aeolian sand transport, manifested in very mobile dune systems during these months. Dune migration in JNP has been studied extensively (Cooke et al., 1993; Jimenez et al., 1999; Maia et al., 2005; Levin et al., 2009). Jimenez et al. (1999), for example, reported that the barchans in the area moved, on average, 17.5 meters per year (ranging from 14-21 m/yr) with larger dunes migrating more slowly than smaller dunes). we selected two typical barchans with their height of 54.5 m (hereafter, larger dune) and 21.3 m (hereafter, smaller dune), respectively (Figure 4.1). According to the model reported by Maia et al. (2000, Figure 4), the migration rate for the smaller dune should be about 19 m/yr and for the larger dune, about 15 m/yr.

More recently, small-scale field experiments on individual barchans have focused on dismantling the complex grainflow processes that drive barchan migration (Pelletier et al., 2015; Sherman et al., under review). The large barchans and sand sheets that dominate the JNP landscape have been used for a multitude of different remote sensing and field-based scientific investigations ranging from aeolian transport processes (Sauermann et al., 2003; Li et al., 2010; Ellis et al., 2012; Farrell et al., 2012; Barrineau and Ellis, 2013; Sherman et al., 2013; Li et al., 2014a; Sherman et al., 2014; Martin et al., 2018) to studies of barchan behavior and evolution (Herrmann et al., 2005; Maia et al., 2005; Parteli et al., 2007; Wu et al., 2011b).

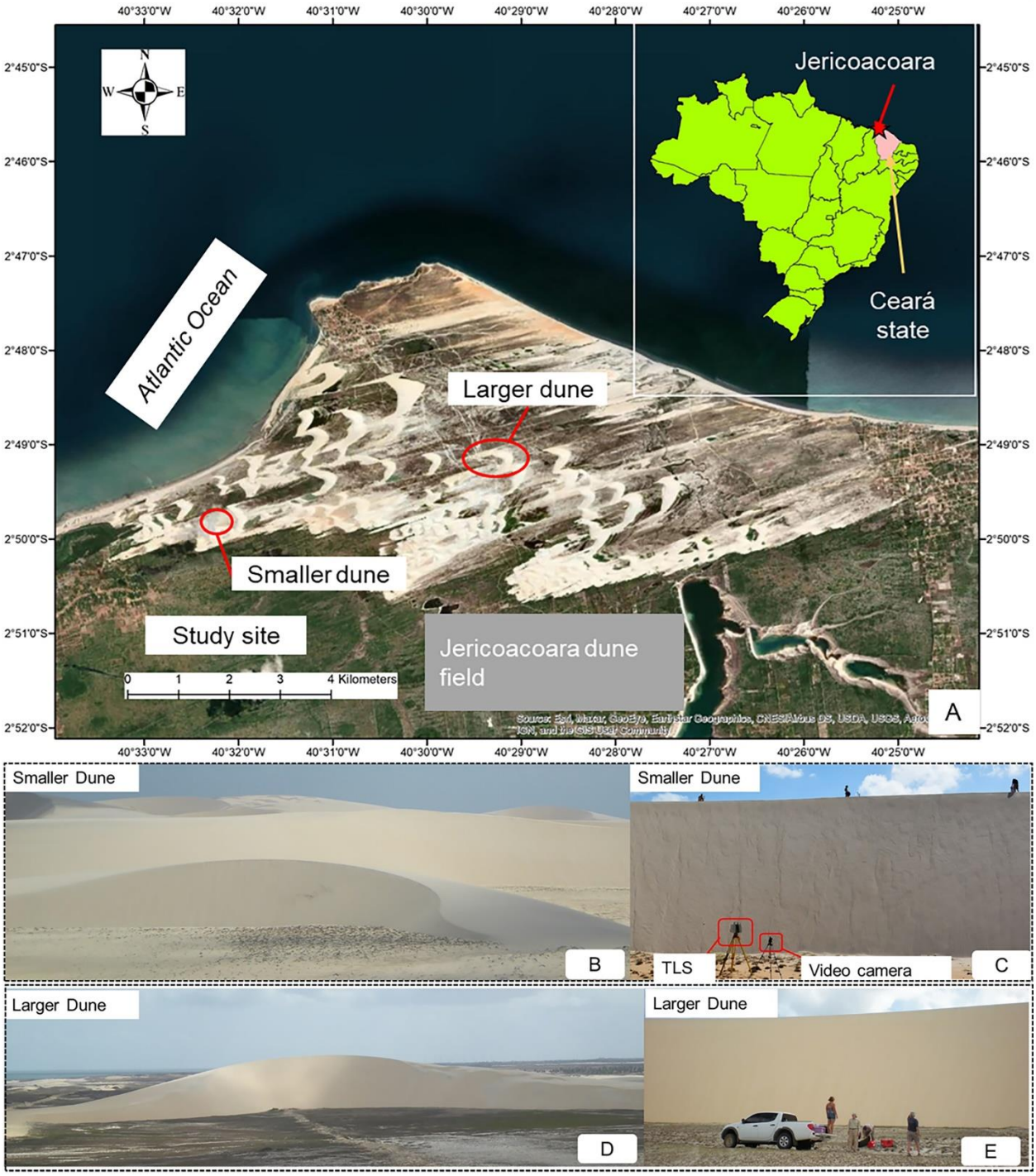

Figure 4. 1. (A) Field site location with the smaller and larger dunes labeled in the satellite imagery (source: Esri, Maxar, GeoEye, Earthstar Geographics, CNES/Airbus DS, USDA, USGS, AeroGRID, IGN, and the GIS User Community); (B) photo taken in the lee side of our smaller dune, the height of this dune is 21.3 m with a horn-to-horn width of about 120 m; (C) photo taken at central slipface base of the smaller dune; (D) photo taken in the lee side of our larger dune, the height of this dune is 54.5 m with a horn-to-horn width of about 405 m; (E) photo taken at central slipface base of the larger dune.

Data collection and pre-processing

Our study used a Leica C10 terrestrial laser scanner to repeatedly measure and record the slipface activities on two barchans (Figure 4.1). The vertical resolution of the scanner is 2 mm with a scan rate of about 50,000 points per second. Point cloud data were registered with three targets in fixed locations to get absolute georeferencing. DEMs with a spatial resolution of 4 cm were produced through filtering and interpolation (Pelletier et al., 2015).

Data were gathered on November 6 and November 8, 2013, on the larger dune (Figure 4.1a) and November 7 and November 9, 2013, on the smaller dune (Figure 4.1b) from approximately 09:00-16:00 on each day. During the same time, a video camera mounted adjacent to the scanner was set to record grainflow activity. The field of view of the camera only covered the central area of the slipface. The duration of an individual scan was approximately 7 minutes on the smaller dune and 13 minutes on the larger dune. We analyzed 114 scans from the smaller dune and 42 scans from the larger dune with corresponding Digital Elevation Models (DEMs) being established. Grainflow signatures are derived by differencing the sequential DEMs (DoDs) from individual measurement days with appropriate threshold values (Zhang, 2021). Typical grainflows captured by the video camera were used for visual validation of their digital representations.

Grainflow morphometry analysis

Using the method of Zhang (2021), 2852 grainflows, comprising the conjoint areas of erosion and deposition, were extracted from the DoDs. For this analysis, grainflows are treated as 'objects' that can be distinguished against a digital background (Liu et al., 2010b). The Zhang (2021) method requires that thresholds be used to identify the object. The method requires two steps filtering with corresponding threshold values to remove outliers and extreme noise. The first pair of threshold values ($|DoD_s| < 5mm$ or $|DoD_s| > 1m$) are to exclude potential errors from the buffering of the instrument by wind gusts (Pelletier et al., 2015). The second pair of threshold values ($|DoD_s| < mean\ of DoD_s - 10 \times standard\ deviation\ of\ DoD_s$ or $|DoD_s| > mean\ of DoD_s + 10 \times standard\ deviation\ of\ DoD_s$) are to remove some extreme values while preserving a wide variation

range for DoDs by trial and error. Table 4.1 shows the morphometric attributes of grainflows with corresponding mathematical calculations. We adopt the algorithm of Diener (2022) to calculate the length (l) and width (w) of the minimal bounding box enclosing a grainflow object. Diener (2022) defined the minimal bounding box as the smallest area rectangle enclosing a set of 2D points. The average length ($\bar{l}_g$) and width ($\bar{w}_g$) are calculated using the four corners of the minimal bounding box as reference points (Figure 4.2). We use the reference points to first find the central length line (magenta line in Figure 4.2a) and central width line (yellow line in Figure 4.2a) according to the four corners of the minimal bounding box. Then, the central length and width lines are equally divided into ten intervals by intersecting points (e.g., O and P in Figure 4.2a), resulting in nine equidistant lengths and widths (blue lines in Figure 4.2b and 4.2c). In the next step, our algorithm is designed to find the two points (e.g., M and N in Figure 4.2b, and S and T in Figure 4.2c) where a blue line (Figure 4.2b and 4.2c) first enters and last leaves a grainflow object. Finally, the equidistant lengths and widths are calculated as the lengths between those two points (e.g., the length between points M and N in Figure 4.2b, and the length between points S and T in Figure 4.2c). The $\bar{l}_g$ and $\bar{w}_g$ are the average of these equidistant lengths and widths. Grainflow area (A) is calculated as the number of pixels within a grainflow object multiplying the corresponding pixel area.

Table 4. 1. Definitions of planform morphometric attributes

Attributes	Definition
Average length ($\bar{l}_g$)	$$\bar{l}_g = \sum l_i / N$$ l_i is an equidistant length that is parallel to the longer side of the minimum bounding box enclosing the grainflow, N is the number of equidistant lengths. An example is shown in Figure 4.2.
Average width ($\bar{w}_g$)	$$\bar{w}_g = \sum w_i / N$$ w_i is an equidistant length that is parallel to the short side of the minimum bounding box enclosing the grainflow, N is the number of equidistant widths. An example is shown in Figure 4.2.
Area (A)	$$A = nr^2$$ n is the number of the grids within a grainflow object, and r is the pixel size.
Elongation (e_g)	$$e_g = \frac{l}{w}$$ l and w are the length and width of the minimum bounding box enclosing a grainflow object.
Rectangularity (r_t)	$$r_t = \frac{A}{l \times w}$$
Compactness (circularity) (c_p)	$$c_p = \frac{4\pi \times A}{P^2}$$ P is the perimeter of a grainflow object.
Asymmetry (ASM)	$$ASM = 1 - b/a$$ a and b are the length of the major and minor axis of the ellipse that has the same normalized second central moments as a grainflow object.
Ellipticity (ELP)	$$ELP = \begin{cases} 16\pi^2 I_1 & if\ I_1 \leq 1/16\pi^2 \\ 1/16\pi^2 I_1 & otherwise \end{cases}$$ $$I_1 = \frac{\mu_{20}\mu_{02} - \mu_{11}^2}{\mu_{00}^4}$$ μ_{pq} are the central moments, I_1 the affine moment invariant (Rosin, 2003)
Triangularity (TRI)	$$TRI = \begin{cases} 108 I_1 & if\ I_1 \leq 1/108 \\ 1/108 I_1 & otherwise \end{cases}$$ I_1 the affine moment invariant (Rosin, 2003)

We also calculated six shape descriptors: elongation (e_g), rectangularity (r_t), compactness (c_p), asymmetry (ASM), ellipticity (ELP), and triangularity (TRI) (Liu et al., 2010b). Elongation is the ratio of the length to the width of a minimum bounding box enclosing a grainflow object. Rectangularity (r_t), with the range 0-1, is the area of a grainflow compared to the corresponding area of the minimum bounding box. A larger r_t suggests a greater similarity to a rectangular shape. Compactness (c_p), also named circularity by Pratt (1991), is the area of a grainflow relative to the area of a circle with the same

perimeter, a widely used shape descriptor (Davis, 2002). A circle is the most compact shape with $c_p = 1$. The more irregular a grainflow boundary, the smaller c_p will be. Asymmetry (ASM) measures the relative ratio of the major and minor axis lengths of an ellipse that has the same normalized second central moments as a grainflow object. The asymmetry of a circle or square is zero. The ellipticity (ELP) and triangularity (TRI), both with the range 0-1, are defined by the affine moment invariant (Flusser and Suk, 1993; Rosin, 2003). A larger value for these indices indicates that a grainflow shape is more similar to the corresponding shape of an ellipse or triangle.

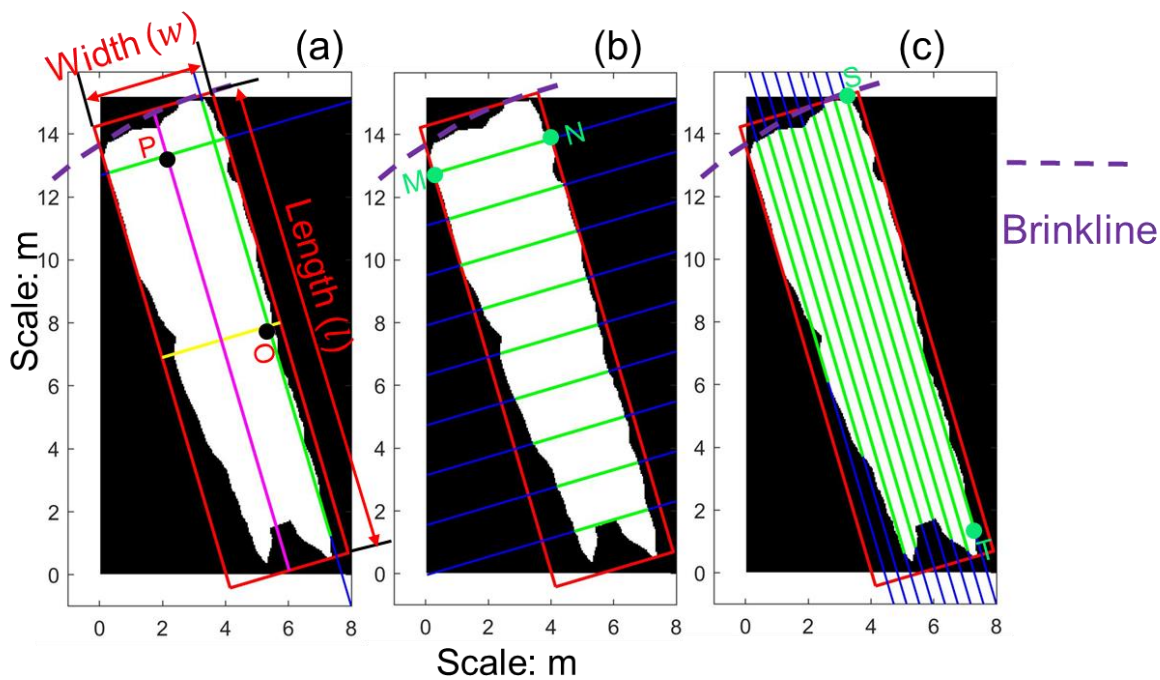

Figure 4. 2. An example illustrating the calculation of average length ($\bar{l}_g$) and width ($\bar{w}_g$). (a) l and w are the length and width of the minimum bounding box enclosing a grainflow object. O and P are the intersecting points which divide l and w into ten equal intervals; (b) equidistant blue lines in the direction of width, $\bar{w}_g$ is the average of green lines inscribing the grainflow. Points M and N are the intersected points where a blue line enters and leaves a grainflow object; (c) equidistant blue lines in the direction of length, $\bar{l}_g$ is the average length of green lines inscribing the grainflow. Points S and T are the intersections where a blue line enters and leaves a grainflow object.

Morphometric analysis

If a grainflow reaches a slipface base, its morphology will be dependent on the slipface length because the length will be controlled by an agency other than the dynamics of the flow itself. To classify grainflow morphometric characteristics which are dune independent, we filter out the samples that are restricted by a slipface length and analyze the remaining grainflow morphometry. We first use those filtered samples to conduct a correlation analysis among the nine morphometric characteristics to reveal redundant attributes and then remove attributes that are highly correlated ($R \geq 0.7$) with others. Decisions on which attribute to retain are made based on a large degree of morphometric variance which can be included in the retained attributes.

We use factor, z-score, and cluster analyses provided by IBM® SPSS® Statistics to identify underlying factors that explain the pattern of correlations within the morphometric attributes and to decide the optimal number of types that reflect grainflow morphometric characteristics. The extraction method of the factor analysis is principal component analysis. Then, we do a Direct Oblimin rotation on the main principal components to visualize the contribution of the morphometric attributes. Finally, we standardize these attributes with Z-Score and use K-Means cluster analysis with Euclidean distance to classify grainflow morphometric characteristics. We also plot the clustered centers of different grainflow types in Z-Score to interpret the differences among these typical types.

Results

A total of 2852 grainflows were measured, including 1609 samples from the smaller dune and 1243 samples from the larger dune. The data set was filtered to remove grainflows with shapes that were deemed to be constricted by slipface length as described in the method section. After removing those grainflows, 2196 samples were left for classification, including 1210 grainflows from the smaller dune and 986 grainflows from the larger dune. The nine morphometric attributes were assessed for redundancy with the result that four variables (A, c_p, ELP, ASM) were found duplicative, with $R \geq 0.7$ accounting for about or more than 50% of the variance in the retained variables (Table 4.2).

Table 4. 2. Correlation matrix of the grainflow morphometric attributes

	$\bar{l}_g$	$\bar{w}_g$	A	r_t	c_p	ELP	TRI	e_g	ASM
$\bar{l}_g$	1.00								
$\bar{w}_g$	0.67**	1.00							
A	0.77**	0.93**	1.00						
r_t	0.02	0.05*	-0.03	1.00					
c_p	-0.35**	0.20**	-0.01	0.38**	1.00				
ELP	-0.03	0.00	-0.07**	0.84**	0.40**	1.00			
TRI	0.05**	0.08**	0.10**	-0.38**	-0.19**	-0.35**	1.00		
e_g	0.24**	-0.37**	-0.17**	0.01	-0.76**	-0.03	-0.04**	1.00	
ASM	0.21**	-0.41**	-0.16**	-0.07**	-0.80**	-0.09**	0.00	0.78**	1.00

* correlation is significant at the 0.05 level (2-tailed).
** correlation is significant at the 0.01 level (2-tailed);

Grainflow morphometry

Five attributes, $\bar{l}_g$, $\bar{w}_g$, r_t, TRI, e_g, were used for factor analysis. The results indicate that there are three factors with eigenvalues greater than 1, which explains 87% variance in the data set. After a Direct Oblimin rotation on these factors, the distribution of the five variables is plotted in Figure 4.3. The variables $\bar{l}_g$ and $\bar{w}_g$ mainly contribute to the first principal component; r_t and TRI mainly contribute to the second principal component; and e_g and $\bar{w}_g$ mainly contribute to the third principal component. Considering the physical representation of the clustered grainflow, we then use the five morphology attributes, $\bar{l}_g$, $\bar{w}_g$, r_t, TRI, e_g for cluster analysis instead of the three principal components.

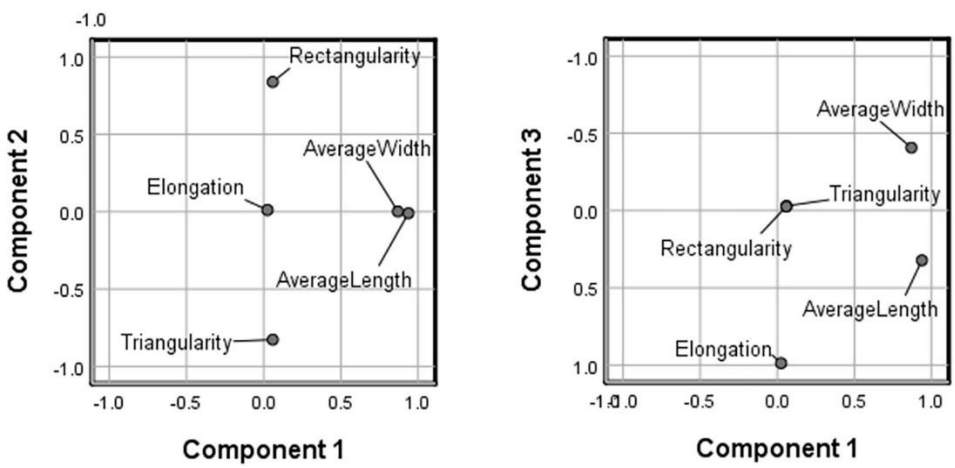

Figure 4. 3. The distribution of three principal components in rotated orthogonal space.

Types of grainflow morphometric characteristics

After K-Means cluster analysis, grainflows are classified into three types based on the Z-score of the five morphometric variables, $\bar{l}_g$, $\bar{w}_g$, r_t, TRI, e_g. Figure 4.4 shows the clustered centers (mean Z-score) of three grainflow types. Type 1 (elongated, narrow grainflows) is characterized by its elongation index. Type 1 grainflows have intermediate length and are most like a rectangular shape. Type 2 (long, triangular grainflows) comprises the longest and widest grainflows and approximates a triangular shape. Type 3 (short, rectangular grainflows) grainflows are short and narrow, with a compact rectangular shape. Descriptive statistics for each type are presented in Table 4.3.

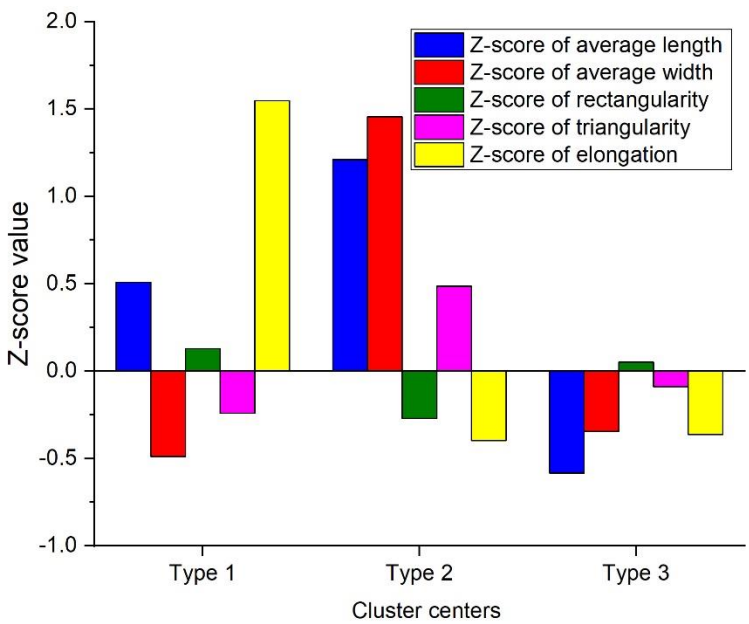

Figure 4. 4. Cluster centers of grainflow morphometric characteristics, graphically indicating key characteristics for each type.

Table 4. 3. Descriptive statistics for the metrics of the grainflow types for all classified grainflow samples. Dimensional unit is meter

	Type 1		Type 2		Type 3	
	Elongated, narrow		Long, triangular		Short, rectangular	
	Avg	Std. Dev	Avg	Std. Dev	Avg	Std. Dev
$\bar{l}_g$	15.7	7.5	21.0	5.9	7.5	3.4
$\bar{w}_g$	1.4	0.7	4.8	2.0	1.6	0.9
A	32.5	27.3	139.2	80.1	18.1	15.6
r_t	0.7	0.1	0.6	0.1	0.7	0.1
TRI	0.8	0.1	0.9	0.1	0.8	0.1
e_g	10.3	2.8	4.6	1.6	4.7	1.7

Elongated, narrow (Type 1) grainflows comprise 19% of the clustered samples. The average length of this type is 15.7 m, which is about 74% and 29% of the longest slipface length on the smaller and larger dune, respectively. Long, triangular grainflows (Type 2) account for 21% of the filtered samples. The average length, width, and area of long triangular grainflows (Type 2) are the largest among these three types. The average length of this type is 21 m, which is almost the longest length of the slipface on the smaller dune and 38% of the longest length on the larger dune slipface. Short, rectangular grainflows (Type 3) occupy the largest percent (60%) of the classified grainflows. The average length of short rectangular (Type 3) grainflows is 7.5, which is the shortest among the three types. On average, this type of grainflows is about 35% and 14% of the longest slipface on the smaller and larger dune, respectively. Figure 4.5 shows several composite examples of each type of grainflows both on the smaller and larger dune slipface. Figure 4.6 includes several examples of the three types of grainflows from video images.

The distribution of grainflow morphometry types is distinctly different on the larger and smaller dune. Of the 1210 grainflows from the smaller dune, the percent of Type 1, Type 2, and Type 3 grainflows are 15%, 2%, and 84%, respectively. On the larger dune, of the 986 grainflows measured, the percent of Type 1, Type 2, and Type 3 grainflows are 25%, 44%, and 31%, respectively. Descriptive statistics for each type on the smaller and larger dune are listed in Table 4.4.

Table 4. 4. Descriptive statistics for the metrics of the grainflow types on the smaller and larger dune. Dimensional unit is meter

	Elongated, narrow (Type 1)				Long, triangular (Type 2)				Short, rectangular (Type 3)			
	Avg*	Std. Dev*	Avg+	Std. Dev+	Avg*	Std. Dev*	Avg+	Std. Dev+	Avg *	Std. Dev*	Avg+	Std. Dev+
$\bar{l}_g$	9.4	3.6	20.2	6.1	11.7	1.9	21.5	5.6	6.7	3.1	10.2	3.1
$\bar{w}_g$	0.9	0.5	1.7	0.6	4.7	1.1	4.8	2.0	1.5	0.8	2.1	0.8
A	11.3	9.4	47.3	26.0	74.3	21.6	142.8	80.6	14.5	13.2	30.0	17.2
r_t	0.7	0.1	0.7	0.1	0.6	0.1	0.6	0.1	0.7	0.1	0.6	0.1
TRI	0.8	0.1	0.8	0.1	0.9	0.1	0.9	0.1	0.8	0.1	0.8	0.1
e_g	10.2	2.9	10.4	2.8	2.5	0.5	4.7	1.6	4.6	1.7	4.7	1.5

* samples from the smaller dune; + samples from the larger dune.

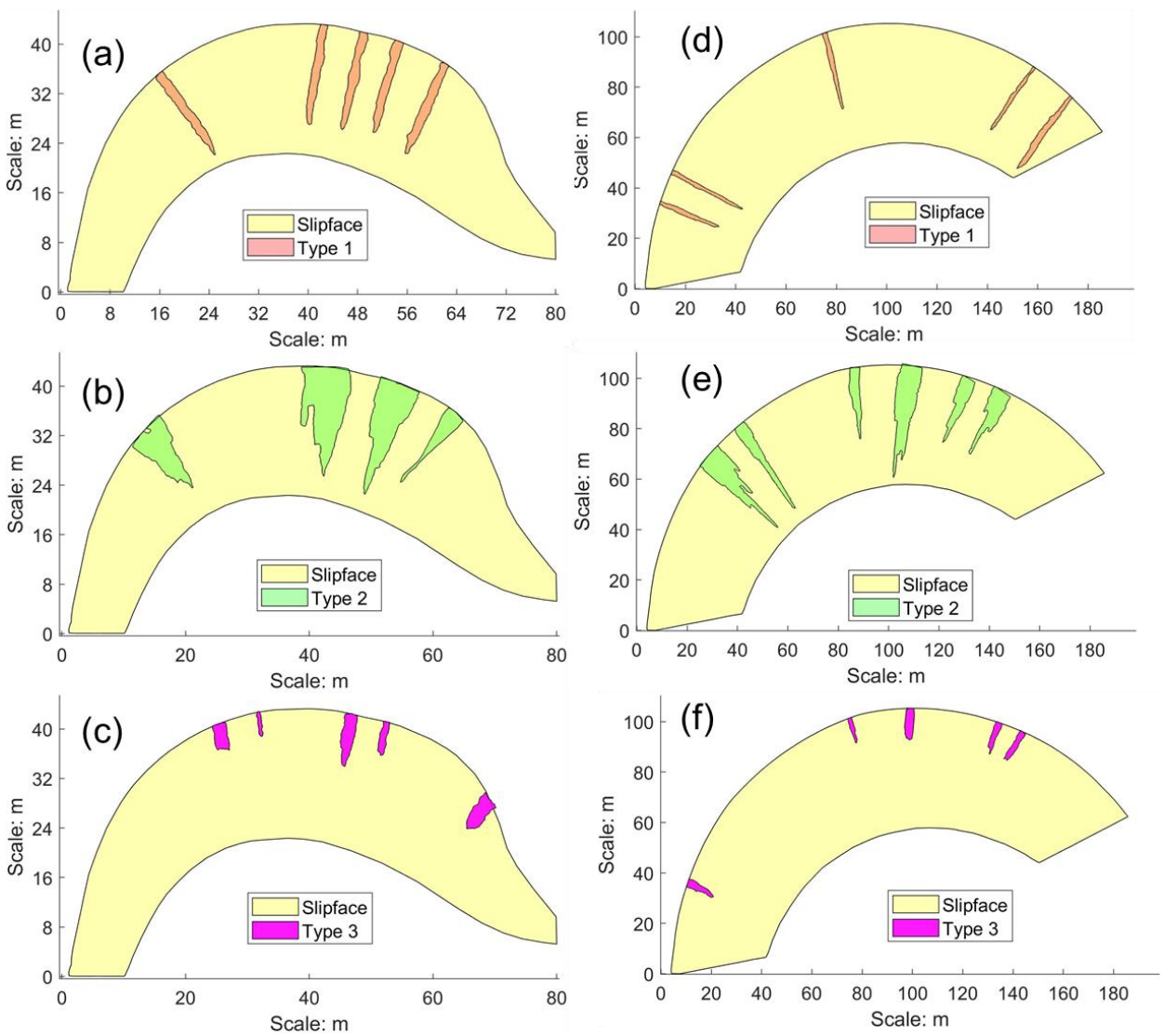

Figure 4. 5. The composite examples of each type of grainflows on the smaller and larger dune slipface. (a), (b), and (c) are from the smaller dune; (d), (e), and (f) are from the larger dune.

Figure 4. 6. Examples of the classified grainflow types (type 1: elongated, narrow grainflows; type 2: long, triangular grainflows; type 3: short, rectangular grainflows) from video images. Rough boundary lines are manually delineated to capture the main features.

Discussion

Grainflow morphometric characteristics

Our classification results are dependent on grainflow morphometry without consideration of grainflow processes; e.g., were they primary or secondary grainflows (Breton et al., 2008; Cornwall et al., 2018b), or formed through scarp recession or slump degradation (Hunter, 1977; Fryberger and Schenk, 1981). We can, however, compare our results with findings from other studies that do attempt to relate form and process. Only Cornwall et al. (2018a; 2018b) classified grainflow shape, but shape information can be derived from the field studies of Breton et al. (2008) and Nield et al. (2017b).

Elongated, narrow-shaped grainflows (Type 1) are similar to the funnel grainflows defined by Cornwall et al. (2018b) and the grainflow signatures observable in Nield et al. (2017b, Fig. 4b) that they associated with 'intermediate' wind speeds (6.5 ms^{-1}). Cornwall et al. (2018b) classified their funnel grainflows as secondary grainflows, as first described by Breton et al. (2008). Breton et al. (2008) indicated that the smaller secondary grainflows were triggered by the larger primary grainflows. Cornwall

et al. (2018b), however, found that secondary grainflows may also occur independently of primary grainflows. They suggested that nearly all secondary grainflows are triggered by processes such as the failure of a lock-up zone that stored sand mid-slope instead of it reaching the slipface base, or increased sediment transport rates caused by faster winds, or the influence of lee-side airflow patterns. Our video recordings confirm the occurrence of elongated, narrow-shaped grainflows independent of larger grainflows, although almost always (≥97%) originating near the brinkline. Our observation of these grainflows suggests that no novel, mid-slope triggering mechanism is necessary for their formation.

Long, triangular grainflows (Type 2) look similar to the grainflow signatures depicted in Nield et al. (2017, Fig. 4c) under their 'fast' wind speeds (8.5 ms^{-1}). Cornwall et al. (2018b) did not report a corresponding shape. Breton et al. (2008), however, did find triangular grainflows and used that shape as one basis for estimating grainflow area. Nickling et al. (2002) suggested that the formation of large grainflows might be related to the wedge-shaped bulges on their high dunes. The influence of grainfall patterns on grainflow morphometric characteristics is beyond the scope of this study and deserves further research.

Short, rectangular grainflows (Type 3) resemble the grainflow signatures depicted in Nield et al. (2017, Fig 4a) formed under slow wind speeds (5.2 ms^{-1}). We also find similar grainflow morphology in the observations of Cornwall et al. (2018a) and the grainflow signatures presented in Breton et al. (2008, Fig. 1 and Table 1). Cornwall et al. (2018b) described these grainflows as lobe-shaped and classified them as small, secondary grainflows. Unlike our observations, Cornwall et al. (2018b) mentioned that nearly all of their lobe grainflows were secondary, formed in the mid-slope region of the slipface. The few that occurred on the upper slope were ascribed to triggering by nearby primary grainflows.

We did not find evidence of hourglass-shaped grainflows that were described by Sutton et al. (2013a) in their wind tunnel experiments and Cornwall et al. (2018b) in the field. Cornwall et al. (2018b) reported that these were the most frequent type in their field study. They also described a slab-type grainflow, similar in morphology to Martian grainflows described by Ewing et al. (2017) as translational. We detected slab avalanches on our larger dune, but they are not grainflows. In a grainflow, as the term

suggests, an internal velocity profile develops as grains slide past one another through the depth flow (e.g., Haff, 1983). Slab-type avalanches, on the other hand, involve mass movement along a failure plane below a layer of cohesive particles that are not in motion relative to one another (e.g., Kokelaar et al., 2017; Gaume et al., 2019). We hypothesize that slab avalanches on dune slipfaces occur when moisture-induced cohesion is greater than in internal shear stresses. Our only observations of slab failure at the field site were on two days following rainfall. Cornwall et al. (2018b) did mention that "heavy rainfall occurred three days before with some light rainfall the night before observations in this study". We have observed similar and widespread slab failures in the Algodones Dunes in southern California after rains in August 2021 (Figure 4.7).

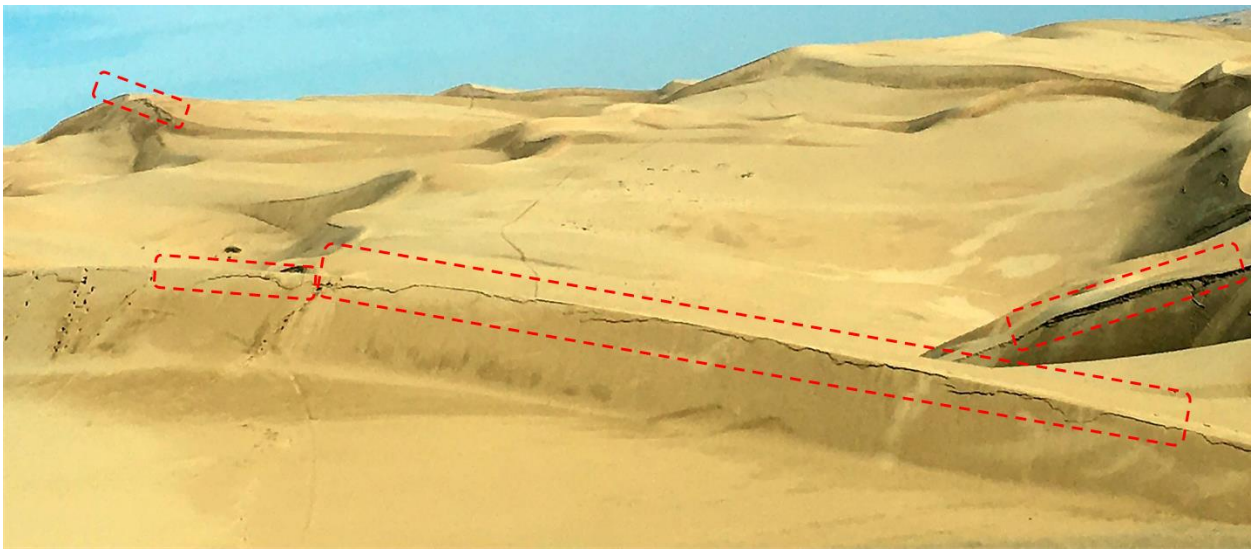

Figure 4. 7. Slab avalanches in the Algodones Dunes, July 31, 2021. The sand was tactile and visibly damp. Note remnant, near-vertical scarps (red dash box) maintained by moisture-induced cohesion. A weather station in Yuma AZ (Tatooine - KAZYUMA175) indicated 33.02 mm rainfall occurred the previous night.

The influence of dune size on grainflow morphology

The different grainflow types occur in different proportions on the smaller and larger dunes. On the smaller dune, 14% of the grainflows are Type 1 (elongated narrow), 2% are Type 2 (long triangular), and 84% grainflows are Type 3 (short rectangular). On the larger dune, the frequencies of the three types are 25%, 44%, and 31%, respectively. The average length of grainflows on the larger dune is approximately twice as long as that on the smaller dune for all three types. The different distributions of

grainflow shapes on the smaller and larger dunes may be related to critical and mean relaxation angles (the difference between critical angle and angle of repose). Pelletier et al. (2015) found that both critical angle and mean relaxation angle were significantly larger on the smaller dune than the larger. The distinctly different distributions of grainflow types on the smaller and larger dune point to dune (slipface) size controls. We also compared the classified grainflow shapes from Cornwall et al. (2018b) with our classifications and translated them to our equivalent types and plotted them based on dune height in Figure 4.7. The 'longer' shapes are favored, obviously, when the slipface is longer. This control may also explain why our findings on grainflow morphology are so different from the observations of Breton et al. (2008), Sutton et al. (2013a), Nield et al. (2017), Ewing et al. (2017), and Cornwall et al.(2018a; 2018b). Those studies are from dunes less than 10 m high. With the constraint of slipface length, the proportion of grainflows reaching the slipface base is similar (25% and 21%, respectively). These grainflows are not included in our classification scheme because their lengths were, perforce, truncated. They are important, however, for their contributions to dune migration. Most of these grainflows we measured did not reach the dune base, but their lockup on the slope, however, produced reservoirs of sand for future delivery to the base.

The hourglass shape reported by Sutton et al. (2013a) from their wind tunnel study and reported from field studies of relatively small dunes by Cornwall et al. (2018b) and from Martian dunes by Ewing et al. (2017) and Cornwall et al. (2018a) was not observed on the Jericoacoara dunes. The long, triangular shapes we observed are missing from descriptions of shape in Sutton et al. (2013a), Ewing et al. (2017), and Cornwall et al. (2018a; 2018b). We noted that the hourglass grainflows from Mars reported by Ewing et al. (2017, Fig. 12b) and Cornwall et al. (2018a, Fig. 5a) are the same. These grainflow shapes are also included in Figure 4.8. The proportion of long triangular grainflows is greatest on the highest of the dunes included in Figure 4.8. The proportion of elongated, narrow grainflows also appears to be a function of dune height, increasing slightly with slipface length. None of these studies reporting grainflow shape reported the 'droplet' shape described by Tischer et al. (2001) from that laboratory inclined surface study.

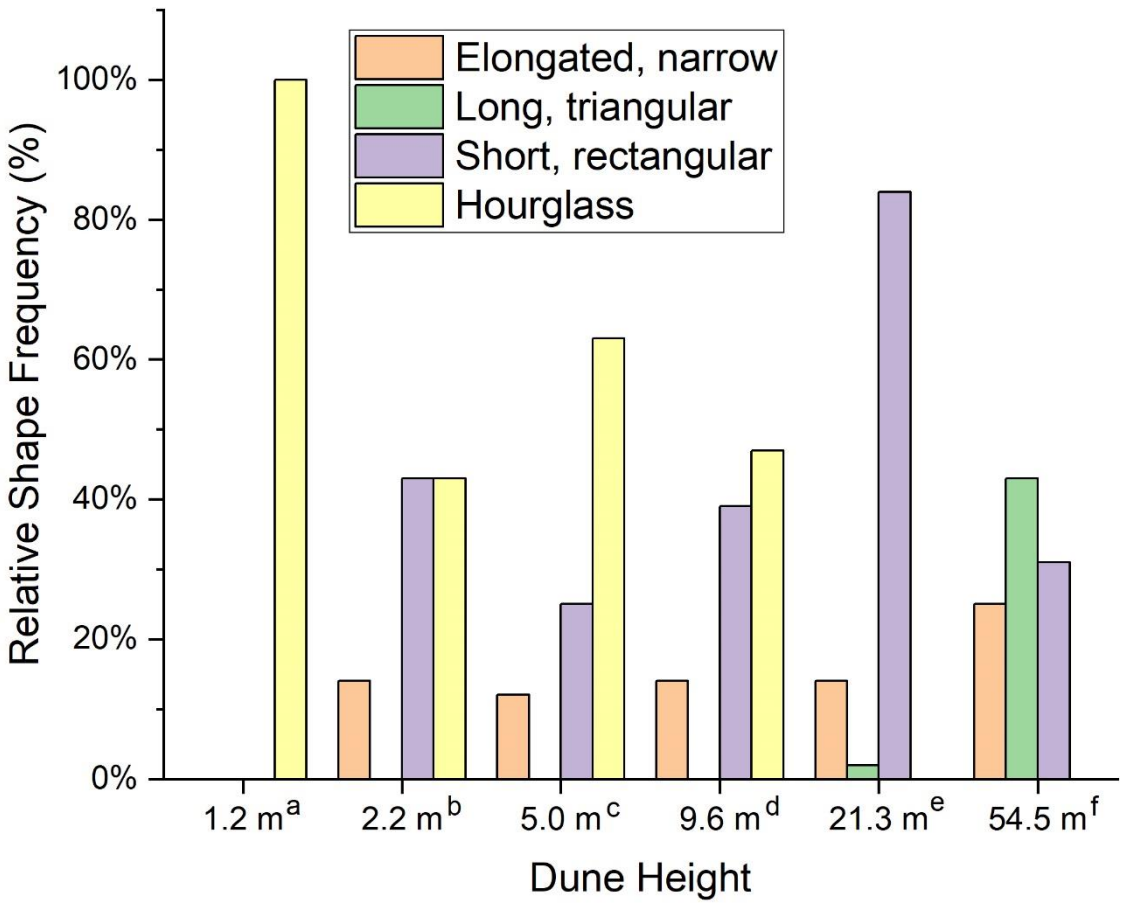

Figure 4. 8. The influence of dune height on grainflow morphology. The superscript 'a' indicates the results from a 1.2 m dune in the wind tunnel study of Sutton et al., (2013a); 'b' suggests the results from a 2.2 m dune in Cornwall et al. (2018a); 'c' indicates the results from a 5.0 m dune on Mars in Ewing et al. (2017) and Cornwall et al. (2018b); 'd' represents the results from a 9.6 m dune in Cornwall et al. (2018a); 'e' represents the results from the dune in 21.3 m high in this study; and 'f' suggests the results from the dune in 54.5 m high in this study.

Conclusions

This study provides the first objective quantification of grainflow morphology on dune slipfaces of substantially different heights (21.3 m and 54.5 m) and different from those of previous studies. We developed a method to analyze repeated Terrestrial Laser scanning data from those dunes to obtain both dimensional morphometrics (average length, average width, and area) and dimensionless shape descriptors (elongation, rectangularity, triangularity). The resulting metrics were used to describe and classify grainflow shapes, recognizing three types: elongated, narrow-shaped grainflows (Type 1), long, triangular grainflows (Type 2), and short, rectangular grainflows (Type 3). We compare the unequal

distributions of the three types on the two slipfaces and with findings from smaller dunes reported in the literature. We can draw the following conclusions from this work.

1. The field and analytical methods we used represent an efficient means of obtaining and assessing the characteristics of grainflows on dune slipfaces, and for the measurement and derivation of metrics for shape classification. Developments in TLS technology allow faster and higher resolution scanning. Future fieldwork using that technology should lead to the refinement of grainflow morphometry.

2. The location where grainflows are triggered, based on a comparison of our data with that of others, seems to be partially controlled by dune height. In our study, almost all grainflows began near the brinkline, whereas in the studies of Cornwall et al. (2018b) many of the grainflows began mid-slope. This difference may be a consequence of bulge geometry, developed within 2 m or so of the brinkline with failure initiated at the base of the bulge. In our study, 2 m is within 5-10% of the top of the slope. In other studies, focused on smaller dunes, the comparable distance puts the failure at approximately mid-slope.

3. The distribution of grainflow shape depends at least partially on slipface (dune) height. This is intuitive when regarding dimensional metrics, but it concerns the dimensionless metrics. On our 21.3 m (smaller) dune, grainflow occurrence is dominated by short rectangular (Type 3) shapes, whereas on the 54.5 m (larger) dune the distribution is much more uniform. On our two dunes, we did not find typical hourglass grainflows which were commonly reported from the relatively short dunes observed by Cornwall et al. (2018b). In contrast, no long, triangular grainflows were reported from these smaller dunes.

This morphometric study does not account for the processes that cause grainflows on dunes nor for how those processes might control resulting grainflow morphology. The potential grainflow shape influences of fluid shear stress, critical angle variations, relationships between grainfall pattern and bulge geometry, and sedimentological variability, remain to be explored. We believe that this classification

study is an important first step toward understanding the nature of those potential controls. Further laboratory, field, and numerical studies are needed to understand the morphodynamics of dunes.

Reference List for Chapter 4

Anderson, R.S., 1988. The Pattern of Grainfall Deposition in the Lee of Aeolian Dunes. Sedimentology 35, 175-188.

Atwood-Stone, C., McEwen, A.S., 2013. Avalanche slope angles in low-gravity environments from active Martian sand dunes. Geophys Res Lett 40, 2929-2934.

Banham, S.G., Gupta, S., Rubin, D.M., Watkins, J.A., Sumner, D.Y., Edgett, K.S., Grotzinger, J.P., Lewis, K.W., Edgar, L.A., Stack-Morgan, K.M., Barnes, R., Bell, J.F., Day, M.D., Ewing, R.C., Lapotre, M.G.A., Stein, N.T., Rivera-Hernandez, F., Vasavada, A.R., 2018. Ancient Martian aeolian processes and palaeomorphology reconstructed from the Stimson formation on the lower slope of Aeolis Mons, Gale crater, Mars. Sedimentology 65, 993-1042.

Barrineau, C.P., Ellis, J.T., 2013. Sediment transport and wind flow around hummocks. Aeolian Research 8, 19-27.

Borzsonyi, T., Halsey, T.C., Ecke, R.E., 2005. Two scenarios for avalanche dynamics in inclined granular layers. Phys Rev Lett 94.

Boyce, R.R., Clark, W.A.V., 1964. The Concept of Shape in Geography. Geogr Rev 54, 561-572.

Breton, C., Lancaster, N., Nickling, W.G., 2008. Magnitude and frequency of grain flows on a desert sand dune. Geomorphology 95, 518-523.

Cooke, R.U., Warren, A., Goudie, A.S., 1993. Desert geomorphology. CRC Press.

Cornwall, C., Bourke, M.C., Jackson, D.W.T., Cooper, J.A.G., 2018a. Aeolian slipface dynamics and grainflow morphologies on Earth and Mars. Icarus 314, 311-326.

Cornwall, C., Jackson, D.W.T., Bourke, M.C., Cooper, J.A.G., 2018b. Morphometric analysis of slipface processes of an aeolian dune: Implications for grain-flow dynamics. Sedimentology 65, 2034-2054.

Daerr, A., Douady, S., 1999. Two types of avalanche behaviour in granular media. Nature 399, 241-243.

Davis, J.C., 2002. Statistics and data analysis in geology. John Wiley & Sons, Inc., New York, 638p.

Diener, J., 2022. 2D Minimal Bounding Box, MATLAB File Exchange.

Douady, S., Andreotti, B., Daerr, A., Clade, P., 2002. From a grain to avalanches: on the physics of granular surface flows. Cr Phys 3, 177-186.

Du Pont, S.C., Fischer, R., Gondret, P., Perrin, B., Rabaud, M., 2005. Instantaneous velocity profiles during granular avalanches. Phys Rev Lett 94, 048003.

Eastwood, E.N., Kocurek, G., Mohrig, D., Swanson, T., 2012. Methodology for reconstructing wind direction, wind speed and duration of wind events from aeolian cross-strata. J Geophys Res-Earth 117.

Ellis, J.T., Sherman, D.J., Farrell, E.J., Li, B.L., 2012. Temporal and spatial variability of aeolian sand transport: Implications for field measurements. Aeolian Research 3, 379-387.

Ewing, R.C., Lapotre, M.G.A., Lewis, K.W., Day, M., Stein, N., Rubin, D.M., Sullivan, R., Banham, S., Lamb, M.P., Bridges, N.T., Gupta, S., Fischer, W.W., 2017. Sedimentary processes of the Bagnold Dunes: Implications for the eolian rock record of Mars. J Geophys Res-Planet 122, 2544-2573.

Farrell, E.J., Sherman, D.J., Ellis, J.T., Li, B., 2012. Vertical distribution of grain size for wind blown sand. Aeolian Research 7, 51-61.

Fenton, L.K., 2006. Dune migration and slip face advancement in the Rabe Crater dune field, Mars. Geophys Res Lett 33.

Flusser, J., Suk, T., 1993. Pattern-Recognition by Affine Moment Invariants. Pattern Recognition 26, 167-174.

Fryberger, S.G., Schenk, C., 1981. Wind Sedimentation Tunnel Experiments on the Origins of Aeolian Strata. Sedimentology 28, 805-821.

Gaume, J., van Herwijnen, A., Gast, T., Teran, J., Jiang, C., 2019. Investigating the release and flow of snow avalanches at the slope-scale using a unified model based on the material point method. Cold Regions Science and Technology 168, 102847.

Haff, P.K., 1983. Grain flow as a fluid-mechanical phenomenon. J Fluid Mech 134, 401-430.

Herrmann, H.J., Andrade, J.S., Schatz, V., Sauermann, G., Parteli, E.J.R., 2005. Calculation of the separation streamlines of barchans and transverse dunes. Physica A 357, 44-49.

Horgan, B.H.N., Bell, J.F., 2012. Seasonally active slipface avalanches in the north polar sand sea of Mars: Evidence for a wind-related origin. Geophys Res Lett 39.

Hunter, R.E., 1977. Basic types of stratification in small eolian dunes. Sedimentology 24, 361-387.

Jimenez, J.A., Maia, L.P., Serra, J., Morais, J., 1999. Aeolian dune migration along the Ceara coast, north-eastern Brazil. Sedimentology 46, 689-701.

Kocurek, G., 1991. Interpretation of Ancient Eolian Sand Dunes. Annu Rev Earth Pl Sc 19, 43-75.

Kocurek, G., Dott, R.H., 1981. Distinctions and Uses of Stratification Types in the Interpretation of Eolian Sand. J Sediment Petrol 51, 579-595.

Kokelaar, B.P., Bahia, R.S., Joy, K.H., Viroulet, S., Gray, J.M.N.T., 2017. Granular avalanches on the Moon: Mass-wasting conditions, processes, and features. J Geophys Res-Planet 122, 1893-1925.

Levin, N., Tsoar, H., Herrmann, H.J., Maia, L.P., Claudino-Sales, V., 2009. Modelling the formation of residual dune ridges behind barchan dunes in North-east Brazil. Sedimentology 56, 1623-1641.

Li, B.L., Ellis, J.T., Sherman, D.J., 2014a. Estimating the impact threshold for wind-blown sand. Journal of Coastal Research, 627-632.

Li, B.L., Sherman, D.J., Farrell, E.J., Ellis, J.T., 2010. Variability of the apparent von Karman parameter during aeolian saltation. Geophys Res Lett 37.

Liu, H.X., Wang, L., Sherman, D., Gao, Y.G., Wu, Q.S., 2010b. An object-based conceptual framework and computational method for representing and analyzing coastal morphological changes. International Journal of Geographical Information Science 24, 1015-1041.

Loope, D.B., Elder, J.F., Sweeney, M.R., 2012. Downslope coarsening in aeolian grainflows of the Navajo Sandstone. Sediment Geol 265, 156-162.

Loope, D.B., Rowe, C.M., Joeckel, R.M., 2001. Annual monsoon rains recorded by Jurassic dunes. Nature 412, 64-66.

Maia, L.P., Freire, G.S.S., Lacerda, L.D., 2005. Accelerated dune migration and aeolian transport during El Nino events along the NE Brazilian coast. Journal of Coastal Research 21, 1121-1126.

Maia, L.P., Jiménez, J.A., Raventos, J.S., de Morais, J.O., 2000. Dune Migration and Aeolian Transport Along Ceará State, Brazil: downscaling and Upscaling Aeolian Induced Processes. Arquivos de Ciências do Mar 33, 99-106.

Martin, R.L., Kok, J.F., Hugenholtz, C.H., Barchyn, T.E., Chamecki, M., Ellis, J.T., 2018. High-frequency measurements of aeolian saltation flux: Field-based methodology and applications. Aeolian Research 30, 97-114.

Mcdonald, R.R., Anderson, R.S., 1995. Experimental-Verification of Aeolian Saltation and Lee Side Deposition Models. Sedimentology 42, 39-56.

McDonald, R.R., Anderson, R.S., 1996. Constraints on eolian grain flow dynamics through laboratory experiments on sand slopes. Journal of Sedimentary Research 66, 642-653.

Nickling, W.G., Neuman, C.M., Lancaster, N., 2002. Grainfall processes in the lee of transverse dunes, Silver Peak, Nevada. Sedimentology 49, 191-209.

Nield, J.M., Wiggs, G.F.S., Baddock, M.C., Hipondoka, M.H.T., 2017b. Coupling leeside grainfall to avalanche characteristics in aeolian dune dynamics. Geology 45, 271-274.

Parteli, E.J., Duran, O., Herrmann, H.J., 2007. Minimal size of a barchan dune. Phys Rev E 75, 011301.

Pelletier, J.D., Sherman, D.J., Ellis, J.T., Farrell, E.J., Jackson, N.L., Li, B.L., Nordstrom, K.F., Maia, L.P., Omidyeganeh, M., 2015. Dynamics of sediment storage and release on aeolian dune slip faces: A field study in Jericoacoara, Brazil. J Geophys Res-Earth 120, 1911-1934.

Pratt, W.K., 1991. Digital Image Processing, chapter 17. Image Segmentation. New York: Wiley, 597-627.

Robinson, D.A., Friedman, S.P., 2002. Observations of the effects of particle shape and particle size distribution on avalanching of granular media. Physica A 311, 97-110.

Rosin, P.L., 2003. Measuring shape: ellipticity, rectangularity, and triangularity. Machine Vision and Applications 14, 172-184.

Sauermann, G., Andrade, J.S., Maia, L.P., Costa, U.M.S., Araujo, A.D., Herrmann, H.J., 2003. Wind velocity and sand transport on a barchan dune. Geomorphology 54, 245-255.

Sherman, D.J., Li, B.L., Ellis, J.T., Farrell, E.J., Maia, L.P., Granja, H., 2013. Recalibrating aeolian sand transport models. Earth Surface Processes and Landforms 38, 169-178.

Sherman, D.J., Swann, C., Barron, J.D., 2014. A high-efficiency, low-cost aeolian sand trap. Aeolian Research 13, 31-34.

Sherman Douglas, Z.P., Pelletier Jon, Ellis Jean, Farrell Eugene, Li Bailiang, 2022. Barchan Slipface Grainflows: Characteristics and Kinematics. Geophys Res Lett under review.

Silvestro, S., Fenton, L.K., Vaz, D.A., Bridges, N.T., Ori, G.G., 2010. Ripple migration and dune activity on Mars: Evidence for dynamic wind processes. Geophys Res Lett 37.

Sutton, S.L.F., Neuman, C.M., Nickling, W., 2013a. Avalanche grainflow on a simulated aeolian dune. J Geophys Res-Earth 118, 1767-1776.

Sutton, S.L.F., Neuman, C.M., Nickling, W., 2013b. Lee slope sediment processes leading to avalanche initiation on an aeolian dune. J Geophys Res-Earth 118, 1754-1766.

Tischer, M., Bursik, M.I., Pitman, E.B., 2001. Kinematics of sand avalanches using particle-image velocimetry. Journal of Sedimentary Research 71, 355-364.

Wu, X., Zou, X., Zheng, Z.C., Zhang, C., 2011b. Field measurement and scaled-down wind-tunnel model measurement of airflow field over a barchan dune. Journal of arid environments 75, 438-445.

Zhang, P., 2021. An algorithm for objective analysis of grainflow morphology. Aeolian Research 50.

Zhao, F.F., Cardenas, B.T., Kim, W., 2021. Controls of Aeolian Dune Height on Cross-Strata Architecture: White Sands Dune Field, New Mexico, USA. Journal of Sedimentary Research 91, 495-506.

CHAPTER 5 CONCLUSIONS AND FUTURE WORK

Conclusions and research directions

The ability of wind-blown sand to shape landforms and to threaten human environments, e.g., in coastal, arid, and semi-arid locations, has been long recognized (Wilson, 1975; Sherman and Nordstrom, 1994; Zhang et al., 2010; Wright et al., 2013; Li and Xu, 2019; Gao et al., 2020). Our understanding of aeolian processes and landforms has advanced greatly through development of theory (Bagnold, 1936; Kalinske, 1943; Kawamura, 1951; Belly, 1962; Owen, 1964; White and Schulz, 1977; Wiberg and Smith, 1985; Anderson and Hallet, 1986; Willetts et al., 1986; Shao and Raupach, 1993; Sherman and Nordstrom, 1994; Lancaster et al., 1996; McDonald and Anderson, 1996; Walker, 1999; Yizhaq et al., 2004; Andreotti et al., 2006; Li et al., 2010; Kok et al., 2012; Sherman and Li, 2012; Pahtz et al., 2014; Pahtz et al., 2020), instrumentation (Wu et al., 2011a; Cheng et al., 2013; Swann and Sherman, 2013; Sherman et al., 2014; Neuman and Bedard, 2017; Martin et al., 2018; Wang et al., 2020), and methods (Horikawa and Shen, 1960; Dong et al., 2003; Pi et al., 2016; Liu et al., 2017; Sherman et al., 2019) beginning with the quantitative experiments on the physical mechanisms of fluid-grain motion conducted by Bagnold (1936). The mechanisms of wind-blown sand, although conceptually simple, are still not fully understood because of the complex physics involved (Lancaster, 1994; Wiggs, 2001; Livingstone et al., 2007).

This dissertation had two objectives: 1) to address underappreciated aspects of wind-blown sand transport, i.e., creep motion mode, and 2) to expand our understanding of the morphodynamics of dunes slipfaces through the study of gravity-driven grainflows. Each chapter is a separate paper, published in peer-review journals. Chapters 2 concerns the measurement, analysis, and discussion of the physical mechanisms of creep transport rate. Chapters 3 and 4 are focused on grainflow morphology

characteristics. Chapter 3 presents an algorithm to extract grainflow boundaries. Chapter 4 focuses on the quantification and classification of grainflow morphology.

Chapter 2

Chapter 2 is published as "Aeolian creep transport: A review" in *Aeolian Research*, 2021, 51, https://doi.org/10.1016/j.aeolia.2021.100711. Creep motion has received the least attention among the three modes of sand transport (creep, saltation, and suspension). In most aeolian sand transport models, creep is either ignored or assumed negligible (Hugenholtz and Barchyn, 2011; Goossens et al., 2018), or to be a constant proportion, i.e., 25% of total transport (Bagnold, 1936; Bagnold, 1937; Bagnold, 1938; Bagnold, 1941; Dong and Qian, 2007; Kurosaki et al., 2022). There are many contradictions in the studies of creep transport (Dong et al., 2003; Rotnicka, 2013; Sherman et al., 2019; Wang et al., 2020; Zhang et al., 2021). These include definitions of creep, methods to measure creep transport, the relationship between creep and saltation, and the contributions of creep transport to total transport. We reviewed and analyzed the main literature concerning the measurement or estimation of creep transport. The review found different reports that creep accounts for as little as 1% and as much as 50% of total transport, numbers substantially different from the value of 25% suggested by Bagnold (1937). We found no constant relationship between q_c/q and u_*/u_{*t} in the literature. Indeed, some papers reported a positive relationship (Sherman et al., 2019; Wang et al., 2020) while others reported a negative relationship (Dong et al., 2003; Dong and Qian, 2007), indicating a fundamental deficit in our understanding of the sand transport system.

Critique for advancement: for future creep studies, critical issues remain concerning fundamental terminology for surface and near-surface transport. Theoretically, creep (reptation), saltation, and suspension modes represent a continuum of motion driven by increasing of fluid forcing, making it is difficult to clearly distinguish and define an objective a transition from one mode to another. Further, there are substantial methodology issues with the measurement of creep transport in the field (e.g., Horikawa and Shen, 1960; Stout and Zobeck, 1996). Different trap designs and lack of a standard protocol make comparison of results from different studies difficult (Horikawa and Shen, 1960; Stout and

Zobeck, 1996; Hijma and Lodder, 2001; Dong et al., 2003; Wu et al., 2011a; Cheng et al., 2013; Swann and Sherman, 2013; Liu et al., 2017; Wang et al., 2020). Based on this review, I would recommend a curve fitting method to estimate creep transport rates. This curve fitting method is not perfect, but it is more practical and reasonable than other field methods of which we are aware. In all approaches, we find a necessary compromise between theoretical understanding and practical empiricism.

Chapter 3

Chapter 3 is "An algorithm for objective analysis of grainflow morphology" published in *Aeolian Research*, 2021, 50, https://doi.org/10.1016/j.aeolia.2021.100686. Grainflows on dune slipfaces create temporary signatures by delivering sand from the upper slope to the lower slope, causing dune migration. Grainflow signatures are indicators of sediment transport processes on and around a slipface, representing fundamental morphodynamics (Fryberger and Schenk, 1981; Haff, 1983; Hunter, 1985; Anderson and Hallet, 1986; Anderson, 1988; Nickling et al., 2002; Borzsonyi et al., 2008; Breton et al., 2008; Eastwood et al., 2012; Sutton et al., 2013a; Ewing et al., 2017; Cornwall et al., 2018a; Cornwall et al., 2018b). Previous studies delineated grainflow boundaries based on manual methods and using sample sizes as small as four (Sutton et al., 2013a; Ewing et al., 2017; Cornwall et al., 2018a; Cornwall et al., 2018b). I present an algorithm to objectively and efficiently extract grainflow boundaries by processing Digital Elevation Models (DEMs) in Matlab and ArcGIS. A comparison of results with video records confirms the viability and efficiency of the method. This semi-automated method becomes increasingly efficient as sample sizes increase, becoming more efficient than manual approaches for sample sizes greater than about 15. This method is also applicable to other forms of slope failure and geophysical flows, e.g., avalanches, snowslides, landslides, and debris flows.

Critique for advancement: Further improvement can be made with high-level algorithm design, e.g., Graphical User Interfaces. The development of fully automated algorithms is currently constrained by the presence of data noise, the occurrence of discontinuous grainflow signatures, and the length of scan intervals used to produce DoDs (Difference of DEMs). A significant issue is how to automatically delineate grainflow boundaries when two or more grainflows are very close to each other. The design of a

Graphical User Interface with a portal for supervision will optimize the performance of the algorithm, using human intelligence to improve efficiency and accessibility. These improvements will make this method more accessible to people with little or no coding experience.

Chapter 4

Chapter 4 is "Quantification and classification of grainflow morphology" published in *Earth Surface Processes and Landforms*, https://doi.org/10.1002/esp.5348. As suggested by Boyce and Clark (1964), the morphometric characteristics of a landform or object in a natural environment may provide linkages to the processes associated with its formation. Grainflow morphology, therefore, may be important to interpreting grainflow processes on a dune slipface (McDonald and Anderson, 1996; Nickling et al., 2002; Breton et al., 2008; Nield et al., 2017a; Cornwall et al., 2018b). We extracted 2852 grainflow objects from measurements obtained from a field experiment in Jericoacoara, Brazil, by applying the algorithm presented in chapter 3. We filtered out samples with lengths that were limited by slipface length and analyzed the remaining grainflow morphometrics to establish a grainflow-shape classification system which is dune-size independent. After a correlation and principal component analysis of nine morphometric attributes, five attributes (average length, average width, elongation, rectangularity, and triangularity) were used to classify grainflow shapes. Three representative shape types were found: Type 1: elongated, narrow grainflows; Type 2: long, triangular grainflows; and Type 3: short, rectangular grainflows. Three conclusions were drawn from this analysis. First, the field and analytical methods we used are efficient means of extracting and assessing grainflow characteristics, and for the measurement and derivation of metrics for shape classification. Second, the location where grainflows are triggered (upper or middle slipface) is partially controlled by dune height. Third, the distribution of grainflow shapes is at least partially a function of dune height.

Critique for advancement: This study suggests two promising topics for future research. The first would be to seek morphometric linkages among slipface morphology (height, bulge geometry), aeolian processes (e.g., transport rates, grainfall patterns), and characteristic grainflow shapes. The second would be to establish a comprehensive model that incorporates factors related to grainflow morphodynamics and

develop rules to describe the redistribution of sand deposits from upper to lower slipface in order to explain slipface evolution and dune migration. The third would be to measure grainflow thicknesses to evaluate the sedimentological relationship between grainflow thickness and dune height (Hunter, 1977; Kocurek and Dott, 1981; Kocurek, 1991). This would be to test the hypothesis that suggests that grainflow thickness is related to dune height – i.e., higher dunes develop thicker grainflows.

In summary, my dissertation covers three understudied topics in aeolian processes and landforms, including aeolian creep, grainflow shape extraction, and grainflow morphology. Each topic is focused on a part of the aeolian system, but they share a common trait: a fast response to associated forcing processes. These topics were developed in the spirit of the process-response credo espoused by Brunsden and Thornes, (1979) p. 464), *For any given set of environmental conditions, through the operation of a constant set of processes, there will be a tendency over time to produce a set of characteristic landforms*. I believe that we can model the formation and evolution of aeolian landforms with associated processes through detailed research on these understudied topics.

Reference List for Conclusions and Future Work

Anderson, R.S., 1988. The Pattern of Grainfall Deposition in the Lee of Aeolian Dunes. Sedimentology 35, 175-188.

Anderson, R.S., Hallet, B., 1986. Sediment Transport by Wind - toward a General-Model. Geological Society of America Bulletin 97, 523-535.

Andreotti, B., Claudin, P., Pouliquen, O., 2006. Aeolian sand ripples: Experimental study of fully developed states. Phys Rev Lett 96.

Bagnold, R.A., 1936. The movement of desert sand. Proceedings of the Royal Society of London. Series A-Mathematical and Physical Sciences 157, 594-620.

Bagnold, R.A., 1937. The transport of sand by wind. The Geographical Journal 89, 409-438.

Bagnold, R.A., 1938. The measurement of sand storms. Proceedings of the Royal Society of London. Series A. Mathematical and Physical Sciences 167, 282-291.

Bagnold, R.A., 1941. The Physics of Blown Sands and Desert Dunes, London: Methuen.

Belly, P.-Y., 1962. Sand movement by wind. California University Berkeley Institution Of Engineering Research.

Borzsonyi, T., Halsey, T.C., Ecke, R.E., 2008. Avalanche dynamics on a rough inclined plane. Phys Rev E 78.

Boyce, R.R., Clark, W.A.V., 1964. The Concept of Shape in Geography. Geogr Rev 54, 561-572.

Breton, C., Lancaster, N., Nickling, W.G., 2008. Magnitude and frequency of grain flows on a desert sand dune. Geomorphology 95, 518-523.

Brunsden, D., Thornes, J., 1979. Landscape sensitivity and change. Transactions of the Institute of British Geographers, 463-484.

Cheng, H., Zou, X.Y., Liu, C.C., He, J.J., Wu, Y.Q., 2013. Transport mass of creeping sand grains and their movement velocities. J Geophys Res-Atmos 118, 6374-6382.

Cornwall, C., Bourke, M.C., Jackson, D.W.T., Cooper, J.A.G., 2018a. Aeolian slipface dynamics and grainflow morphologies on Earth and Mars. Icarus 314, 311-326.

Cornwall, C., Jackson, D.W.T., Bourke, M.C., Cooper, J.A.G., 2018b. Morphometric analysis of slipface processes of an aeolian dune: Implications for grain-flow dynamics. Sedimentology 65, 2034-2054.

Dong, Z.B., Liu, X.P., Wang, H.T., Zhao, A.G., Wang, X.M., 2003. The flux profile of a blowing sand cloud: a wind tunnel investigation. Geomorphology 49, 219-230.

Dong, Z.B., Qian, G.Q., 2007. Characterizing the height profile of the flux of wind-eroded sediment. Environ Geol 51, 835-845.

Eastwood, E.N., Kocurek, G., Mohrig, D., Swanson, T., 2012. Methodology for reconstructing wind direction, wind speed and duration of wind events from aeolian cross-strata. J Geophys Res-Earth 117.

Ewing, R.C., Lapotre, M.G.A., Lewis, K.W., Day, M., Stein, N., Rubin, D.M., Sullivan, R., Banham, S., Lamb, M.P., Bridges, N.T., Gupta, S., Fischer, W.W., 2017. Sedimentary processes of the Bagnold Dunes: Implications for the eolian rock record of Mars. J Geophys Res-Planet 122, 2544-2573.

Fryberger, S.G., Schenk, C., 1981. Wind Sedimentation Tunnel Experiments on the Origins of Aeolian Strata. Sedimentology 28, 805-821.

Gao, J.M., Chen, D.X., Saitiniyazi, M., 2020. Vulnerability of Oasis Agriculture to Sandstorm Disasters in Xinjiang, China. Bangl J Bot 49, 981-988.

Goossens, D., Nolet, C., Etyemezian, V., Duarte-Campos, L., Bakker, G., Riksen, M., 2018. Field testing, comparison, and discussion of five aeolian sand transport measuring devices operating on different measuring principles. Aeolian Research 32, 1-13.

Haff, P.K., 1983. Grain flow as a fluid-mechanical phenomenon. J Fluid Mech 134, 401-430.

Hijma, M., Lodder, Q.J., 2001. An evaluation of aeolian sand transport models using four different sand traps at the Hors, Texel.

Horikawa, K., Shen, H.W., 1960. Sand movement by wind action:(on the characteristics of sand traps).

Hugenholtz, C.H., Barchyn, T.E., 2011. Laboratory and field performance of a laser particle counter for measuring aeolian sand transport. J Geophys Res-Earth 116.

Hunter, R.E., 1977. Basic types of stratification in small eolian dunes. Sedimentology 24, 361-387.

Hunter, R.E., 1985. A Kinematic Model for the Structure of Lee-Side Deposits. Sedimentology 32, 409-422.

Kalinske, A.A., 1943. Turbulence and the transport of sand and silt by wind. Annals of the New York Academy of Sciences 44, 41-54.

Kawamura, R., 1951. Study on sand movement by wind. Rept. Inst. Sci. Technol. 5, 95-112.

Kocurek, G., 1991. Interpretation of Ancient Eolian Sand Dunes. Annu Rev Earth Pl Sc 19, 43-75.

Kocurek, G., Dott, R.H., 1981. Distinctions and Uses of Stratification Types in the Interpretation of Eolian Sand. J Sediment Petrol 51, 579-595.

Kok, J.F., Parteli, E.J.R., Michaels, T.I., Karam, D.B., 2012. The physics of wind-blown sand and dust. Rep Prog Phys 75.

Kurosaki, Y., Kinugasa, T., Nyamtseren, M., Liu, S., Otani, S., 2022. Impacts of Aeolian Desertification and Dust Storms on Ecosystems, Economic Development, and Human Health. Combating Aeolian Desertification in Northeast Asia, 129.

Lancaster, N., 1994. Dune morphology and dynamics, Geomorphology of desert environments. Springer, pp. 474-505.

Lancaster, N., Nickling, W., Neuman, C.M., Wyatt, V., 1996. Sediment flux and airflow on the stoss slope of a barchan dune. Geomorphology 17, 55-62.

Li, B.L., Sherman, D.J., Farrell, E.J., Ellis, J.T., 2010. Variability of the apparent von Karman parameter during aeolian saltation. Geophys Res Lett 37.

Li, D.J., Xu, D.Y., 2019. Sand fixation function response to climate change and land use in northern China from 1981 to 2015. Aeolian Research 40, 23-33.

Liu, B., Jin, H.L., Sun, L.Y., Sun, Z., Zhang, C.X., 2017. Grain size and geochemical study of the surface deposits of the sand dunes in the Mu Us desert, northern China. Geol J 52, 1009-1019.

Livingstone, I., Wiggs, G.F., Weaver, C.M., 2007. Geomorphology of desert sand dunes: A review of recent progress. Earth-science reviews 80, 239-257.

Martin, R.L., Kok, J.F., Hugenholtz, C.H., Barchyn, T.E., Chamecki, M., Ellis, J.T., 2018. High-frequency measurements of aeolian saltation flux: Field-based methodology and applications. Aeolian Research 30, 97-114.

McDonald, R.R., Anderson, R.S., 1996. Constraints on eolian grain flow dynamics through laboratory experiments on sand slopes. Journal of Sedimentary Research 66, 642-653.

Neuman, C.M., Bedard, O., 2017. A wind tunnel investigation of particle segregation, ripple formation and armouring within sand beds of systematically varied texture. Earth Surface Processes and Landforms 42, 749-762.

Nickling, W.G., Neuman, C.M., Lancaster, N., 2002. Grainfall processes in the lee of transverse dunes, Silver Peak, Nevada. Sedimentology 49, 191-209.

Nield, J.M., Wiggs, G.F., Baddock, M.C., Hipondoka, M.H., 2017a. Coupling leeside grainfall to avalanche characteristics in aeolian dune dynamics. Geology 45, 271-274.

Owen, P.R., 1964. Saltation of Uniform Grains in Air. J Fluid Mech 20, 225-242.

Pahtz, T., Clark, A.H., Valyrakis, M., Duran, O., 2020. The Physics of Sediment Transport Initiation, Cessation, and Entrainment Across Aeolian and Fluvial Environments. Rev Geophys 58.

Pahtz, T., Parteli, E.J.R., Kok, J.F., Herrmann, H.J., 2014. Analytical model for flux saturation in sediment transport. Phys Rev E 89.

Pi, H., Sharratt, B., Feng, G., Lei, J., Li, X., Zheng, Z., 2016. Validation of SWEEP for creep, saltation, and suspension in a desert-oasis ecotone. Aeolian Research 20, 157-168.

Rotnicka, J., 2013. Aeolian vertical mass flux profiles above dry and moist sandy beach surfaces. Geomorphology 187, 27-37.

Shao, Y., Raupach, M.R., 1993. Effect of Saltation Bombardment on the Entrainment of Dust by Wind. J Geophys Res-Atmos 98, 12719-12726.

Sherman, D.J., Li, B.L., 2012. Predicting aeolian sand transport rates: A reevaluation of models. Aeolian Research 3, 371-378.

Sherman, D.J., Nordstrom, K.F., 1994. Hazards of wind-blown sand and coastal sand drifts: a review. Journal of coastal research, 263-275.

Sherman, D.J., Swann, C., Barron, J.D., 2014. A high-efficiency, low-cost aeolian sand trap. Aeolian Research 13, 31-34.

Sherman, D.J., Zhang, P., Martin, R.L., Ellis, J.T., Kok, J.F., Farrell, E.J., Li, B.L., 2019. Aeolian Ripple Migration and Associated Creep Transport Rates. Geosciences 9.

Stout, J.E., Zobeck, T.M., 1996. The Wolfforth field experiment: A wind erosion study. Soil Science 161, 616-632.

Sutton, S.L.F., Neuman, C.M., Nickling, W., 2013a. Avalanche grainflow on a simulated aeolian dune. J Geophys Res-Earth 118, 1767-1776.

Swann, C., Sherman, D.J., 2013. A bedload trap for aeolian sand transport. Aeolian Research 11, 61-66.

Walker, I.J., 1999. Secondary airflow and sediment transport in the lee of a reversing dune. Earth Surface Processes and Landforms: The Journal of the British Geomorphological Research Group 24, 437-448.

Wang, P., Zhang, J., Dun, H.C., Herrmann, H.J., Huang, N., 2020. Aeolian Creep Transport: Theory and Experiment. Geophys Res Lett 47.

White, B.R., Schulz, J.C., 1977. Magnus Effect in Saltation. J Fluid Mech 81, 497-512.

Wiberg, P.L., Smith, J.D., 1985. A Theoretical-Model for Saltating Grains in Water. J Geophys Res-Oceans 90, 7341-7354.

Wiggs, G.F., 2001. Desert dune processes and dynamics. Progress in physical geography 25, 53-79.

Willetts, B.B., Rice, M.A., Nickling, W., 1986. Collision in aeolian transport: the saltation/creep link.

Wilson, R.L., 1975. Wind-blown sand injury on seeded onions and some control measures. Texas Tech University.

Wright, D.K., Darling, J.A., Lewis, B.V., Fertelmes, C.M., Loendorf, C., Williams, L., Woodson, M.K., 2013. The Anthropology of Dust: Community Responses to Wind-Blown Sediments within the Middle Gila River Valley, Arizona. Human ecology 41, 423-435.

Wu, J., Sun, H., Li, J., Luo, S., 2011a. Experimental research on threshold wind velocity for creeping sand. J. Desert Res 31, 571-574.

Yizhaq, H., Balmforth, N.J., Provenzale, A., 2004. Blown by wind: nonlinear dynamics of aeolian sand ripples. Physica D 195, 207-228.

Zhang, K.C., Qu, J.J., Liao, K.T., Niu, Q.H., Han, Q.J., 2010. Damage by wind-blown sand and its control along Qinghai-Tibet Railway in China. Aeolian Research 1, 143-146.

Zhang, P., Sherman, D.J., Li, B.L., 2021. Aeolian creep transport: A review. Aeolian Research 51.